Graduate School ETD Form 9
(Revised 12/07)

PURDUE UNIVERSITY
GRADUATE SCHOOL
Thesis/Dissertation Acceptance

This is to certify that the thesis/dissertation prepared

By Amanda P Siegel

Entitled
Regulating Lipid Organization and Investigating Membrane Protein Properties in Physisorbed Polymer-tethered Membranes

For the degree of Doctor of Philosophy

Is approved by the final examining committee:

Christoph A Naumann
Chair

Robert Minto

David Thompson

Kenneth Ritchie

To the best of my knowledge and as understood by the student in the *Research Integrity and Copyright Disclaimer (Graduate School Form 20)*, this thesis/dissertation adheres to the provisions of Purdue University's "Policy on Integrity in Research" and the use of copyrighted material.

Approved by Major Professor(s): Christoph A Naumann

Approved by: Martin J. O'Donnell 06/07/2011
Head of the Graduate Program Date

Graduate School Form 20
(Revised 9/10)

PURDUE UNIVERSITY
GRADUATE SCHOOL

Research Integrity and Copyright Disclaimer

Title of Thesis/Dissertation:

Regulating Lipid Organization and Investigating Membrane Protein Properties in Physisorbed Polymer-tethered Membranes

For the degree of Doctor of Philosophy

I certify that in the preparation of this thesis, I have observed the provisions of *Purdue University Executive Memorandum No. C-22,* September 6, 1991, *Policy on Integrity in Research.**

Further, I certify that this work is free of plagiarism and all materials appearing in this thesis/dissertation have been properly quoted and attributed.

I certify that all copyrighted material incorporated into this thesis/dissertation is in compliance with the United States' copyright law and that I have received written permission from the copyright owners for my use of their work, which is beyond the scope of the law. I agree to indemnify and save harmless Purdue University from any and all claims that may be asserted or that may arise from any copyright violation.

Amanda P Siegel

Printed Name and Signature of Candidate

06/02/2011

Date (month/day/year)

*Located at http://www.purdue.edu/policies/pages/teach_res_outreach/c_22.html

REGULATING LIPID ORGANIZATION AND INVESTIGATING MEMBRANE PROTEIN PROPERTIES IN PHYSISORBED POLYMER-TETHERED MEMBRANES

A Dissertation

Submitted to the Faculty

of

Purdue University

by

Amanda P. Siegel

In Partial Fulfillment of the

Requirements for the Degree

of

Doctor of Philosophy

August 2011

Purdue University

Indianapolis, Indiana

ACKNOWLEDGEMENTS

In the Talmud, we are admonished to find for ourselves a master teacher, and a colleague. My advisor, Christoph Naumann, has been a master teacher. Thank you, Christoph, for teaching me what I wanted to know, and what I needed to know, for leading when I needed a push, and for letting me lead from time to time. Dan Minner has been a most valued colleague. Thanks Dan for a great proofreading job (the errors are all my own), great suggestions, helping me in all kinds of ways, straightening me out at times, and just generally making life around the lab really fun for the last five years. Thanks to Merrell Johnson for the bulk of the atomic force microscopy data, and for teaching me how to acquire one of the data sets myself and Ricardo Decca for further assistance with the AFM and a really great sense of humor. Sumit Garg taught me many techniques and is responsible for the single particle tracking data in Section 4.2. To Mike Murcia, thank you for your long range mean square displacement tracking data and of course for pioneering the sonochemical synthesis of quantum dots, one of my favorite things to do in lab. Ann Kimble-Hill taught me how to incorporate membrane proteins into model bilayers and is responsible for Figure 4.2.1 and some of the results on protein sequestration described in Section 4.2.3. Thanks to Noor F. Hussain for assistance acquiring some data in Section 4.1.2 and to Kevin Song, Corey Lin and Dan Minner for the quantum dots used in Section 3.2.6.2. Thanks to Forrest Andrews for a meticulous proof-reading job. Mark Federwisch gave critical IT support to keep the microscopes

talking to the computers that run them, and helping set up back up systems. Guilherme Sprowl and David O'Brien both added youthful energy and enthusiasm during their high school internships. Thanks, guys.

To my husband, three children, and many dear friends in Indianapolis, your patience and generosity has been overwhelming. Jonah, Ruth and Isaac, you have been very understanding of the demands of graduate school, particularly the last six months. I value being your Mom more than anything. Catherine, Marcia, Yanit, Sue, Shira and Barbara, thank you for your support, especially as I navigated from homemaker to full-time graduate student. Tax, thanks for all the lunches. Chris, thanks for the long-range love and short-range support, especially with the creek. To my husband, Miles, your pride in my accomplishments and love have sustained me the last five years through graduate school, and the dozen plus before that. I wake up every morning knowing I am very lucky to be married to you and I love you very much.

Finally, this thesis is dedicated to David Shapiro and Linda Grossinger, both of blessed memory, whose life-long love of learning lifted me, inspired me and unfortunately ended too soon.

TABLE OF CONTENTS

Page

LIST OF TABLES

LIST OF FIGURES

Figure Page

Figure Page

Figure Page

Figure Page

DEFINITIONS FOR FREQUENTLY USED SYMBOLS

θ	Angle of buckling
ε	Brightness
v	Poisson ratio
ξ	Normalized height of buckles (w_{max}/h)
σ_c	Critical stress
σ_c/E^*	Normalized critical stress
σ_o	Actual stress
σ_o/σ_c	Loading parameter
τ_D	Characteristic diffusion time (for FCS)
A_l	Area per lipid molecule
$A_{l,o}$	Equilibrium area per lipid molecule ($X_p = 0$)
a_m	Length of monomer (nm)
b	buckle half-width
B_2, B_3	Virial coefficients for expression of A_l
BA	Bearing area (fraction of buckled area)
D_{corral}	Fractal dimension (of corral)
D_{diff}	Diffusion coefficient
d_l	Length of lipid tail in monolayer
$d_{l,o}$	Equilibrium length of lipid tail in monolayer

E	Young's modulus
E^*	Plane-strain modulus
E_{raft}	Raftophilic Excess
$G(t)$	Autocorrelation function
h	Monolayer film thickness (L_p + h)
$h(k)$	Experimentally acquired photon counting histograms
I	Intensity
k_B	Boltzmann's constant
K_c	Curvature elastic modulus or bending stiffness
K_p	Partition Coefficient
L_p	Length of polymer brush
N_{avg}	Average number of particles
N_{corr}	Number of corrals
n_p	Number of monomers
$PCH(k;N_{avg},\varepsilon)$	Solutions to the PCH algorithm for k
PSF	Point Spread Function
Q	Structure factor
R_c	Critical stiffness ratio
w_{max}	height of buckles
$X_{migrate}$	Mole Fraction Migrating
X_p	Mole fraction lipopolymer (or tether concentration)

LIST OF ABBREVIATIONS

AFM	Atomic Force Microscopy
BAM	Brewster angle microscopy
CCD	Charge coupled device
CDF	Cumulative distribution function
CHOL	Cholesterol
CS-XY	Confocal spectroscopy XY
CTxB	Cholera toxin B
$diC_{18}E_{50}$	1,2-dioctadecyl-*sn*-glycero-3-*N*-poly(2-ethyl-2-oxazoline)$_{50}$
$diC_{18}M_{50}$	1,2-dioctadecyl-*sn*-glycero-3-*N*-poly(2-methyl-2-oxazoline)$_{50}$
DODA-E_{85}	Dioctadecylamine poly(2-ethyl-2-oxazoline)$_{85}$
DPPC	1,2-dipalmitoyl-*sn*-glycero-3-phosphocholine
DPTE	1,2-dipalmitoyl-*sn*-glycero-3-phosphothioethanol
DSPE-PEG5000	Ammonium salt of 1,2-distearoyl-*sn*-glycero-3-phosphoethanolamine-*N*-[methoxy(polyethylene glycol)-5000]
ECM	Extracellular matrix
EPI	Epifluorescence
FCS	Fluorescence correlation spectroscopy
FFS	Fluorescence fluctuation spectroscopy
FN	Fibronectin

FRAP	Fluorescence recovery after photobleaching
FvK	Föppl/von Kárman
G	Gaseous
GM1	Ganglioside GM1
GPMV	Giant plasma membrane vesicle
GUV	Giant unilamellar vesicle
IF	Immobile fraction
LB	Langmuir/Blodgett
LC	Liquid condensed
l_d	Liquid disordered
LE	Liquid expanded
l_o	Liquid ordered
LS	Langmuir/Schaefer
MAbs	Monoclonal antibodies
NBD-PE	Triethylammonium salt of *N*-(7-nitrobenz-2-oxa-1,3-diazol- 4-yl)-1,2-dihexadecanoyl-*sn*- glycero-3-phosphoethanolamine
OG	Octyl-β-D-glucopyranoside
PBS	Phosphate buffered solution
PCH	Photon counting histogram
PSF	Point Spread Function
QD	Quantum dots
R6G	Rhodamine 6G
RGD	Arginine-glycine-aspartic acid

SOPC	1-stearoyl-2-oleoyl-*sn*-glycero-3-phosphocholine
TRITC-DHPE	Triethylammonium salt of *N*-(6-tetramethylrhodamine thiocarbamoyl)-1,2-dihexadecanoyl-*sn*-glycero-3-phosphoethanolamine
VN	Vitronectin

ABSTRACT

Siegel, Amanda P. Ph.D., Purdue University, August 2011. Regulating Lipid Organization and Investigating Membrane Protein Properties in Physisorbed Polymer-tethered Membranes. Major Professor: Christoph A. Naumann.

Cell membranes have remarkable properties both at the microscopic level and the molecular level. The current research describes the use of physisorbed polymer-grafted lipids in model membranes to investigate some of these properties on both of these length scales. On the microscopic scale, plasma membranes can be thought of as heterogenous thin films. Cell membranes adhered to elastic substrates are capable of sensing substrate/film mismatches and modulating their membrane stiffness to more closely match the substrate. Membrane/substrate mismatch can be modeled by constructing lipopolymer-enriched lipid monolayers with different bending stiffnesses and physisorbing them to rigid substrates which causes buckling. This report describes the use of atomic force microscopy and epimicroscopy to characterize these buckled structures and to illustrate the use of the buckled structures as diffusion barriers in lipid bilayers. In addition, a series of monolayers with varying bending stiffnesses and thicknesses are constructed on rigid substrates to analyze changes in buckling patterns and relate the experimental results to thin film buckling theory.

On the molecular scale, plasma membranes can also be thought of as heterogeneous mixtures of lipids where the specific lipid environment is a crucial factor affecting membrane protein function. Unfortunately, heterogeneities involving cholesterol, labeled lipid rafts, are small and transient in live cells. To address this difficulty, the present work describes a model platform based on polymer-supported lipid bilayers containing stable raft-mimicking domains into which transmembrane proteins are incorporated ($\alpha_v\beta_3$, and $\alpha_5\beta_1$integrins). This flexible platform enables the use of confocal fluorescence fluctuation spectroscopy to quantitatively probe the effect of cholesterol concentrations and the binding of native ligands (vitronectin and fibronectin for $\alpha_v\beta_3$, and $\alpha_5\beta_1$) on protein oligomerization state and on domain-specific protein sequestration. In particular, the report shows significant ligand-induced integrin sequestration with a low level of dimerization. Cholesterol concentration increases rate of dimerization, but only moderately. Ligand addition does not affect rate of dimerization in either system. The combined results strongly suggest that ligands induce changes to integrin conformation and/or dynamics without inducing changes in integrin oligomerization state, and in fact these ligand-induce conformational changes impact protein-lipid interactions.

CHAPTER 1 INTRODUCTION

1.1 Rationale and Objectives

Cell membranes have remarkable properties at both the microscopic and molecular scales. Although bilayers comprised of lipids alone are fairly inelastic, the human lung is a compressible lipid monolayer which is capable of expanding by as much as 80% during one breathing cycle (1). This is thought to occur due to monolayer collapse and restoration, but the specifics are still under investigation (2-4). Phagocytosis, the process of neutrophils expanding their plasma membranes by as much as 200% to engulf foreign particles and destroy them, probably involves membrane unwrinkling, although the mechanisms by which this occurs are also far from clear (5, 6).

Beyond this unexplained unwrinkling and extensibility, another interesting "microscale" mechanical property of cell membranes is bending stiffness and bending elasticity. Cell membranes can vary in elasticity by as much as four orders of magnitude (7), from the very soft red blood cells (8) and fibroblasts (in some circumstances) (9) to chondrocytes (10), osteoblasts (11), and the very stiff slime mold *Dictyostelium discoideum* (12). The mechanical properties of cells, including membrane bending stiffness and elasticity can be influenced by many different factors, including malignancy (7), osteoarthritis (10), and external stimuli (9). However, it is difficult to systematically study the effect of altering the mechanical properties of cell membranes. First, cells

display very different elasticities in suspension or attached to substrates. Second, cells will alter their bending elasticity depending on a number of factors including substrate stiffness and density and type of cell-substrate linker (11). Another difficulty is that cell stiffness is often measured for whole cells, while different membranes within the cell have different stiffnesses; the nucleus being quite stiff (13) and different areas of a single cell having different elastic moduli (7). Finally, there are difficulties getting comparable information on membrane stiffness from different methodologies (14). One way to overcome the difficulties of studying the mechanical effect of changes in membrane stiffness on a rapidly changing plasma membrane is to construct a model system and study the mechanical responses of lipid bilayers to different stresses in a controlled setting.

On the molecular level, a fascinating property of cell membranes is that small-scale lipid heterogeneities may be extremely important for determining membrane characteristics (15, 16), and are important for regulating location and functionality of membrane-associated proteins (17-21). One class of heterogeneous patches, lipid rafts, are defined as dynamic assemblies enriched in cholesterol (CHOL), sphingolipids and glycosylphosphatidylinositol (GPI)-anchored proteins (18, 22). Rafts of membrane proteins, in concert with other proteins or possibly lipids induce cellular activity as varied as creation of signaling platforms (23-26), pathogenesis through endocytosis (27), signal transduction leading to cell growth, differentiation and survival (28), and changes to cellular adhesion, cell morphology and angiogenesis (29). One possible explanation for

this incredible versatility is that energetically, it costs a cell very little to segregate or aggregate proteins through the use of lipid rafts (22).

The current best method to investigate transient effects of lipid rafts on protein functionality in the plasma membrane is to either deplete or load a plasma membrane of cholesterol content and watch for changes in protein functionality. If functionality is altered upon cholesterol depletion, and restored upon returning cholesterol to normal levels, rafts are thought to be implicated (30-34). Changes in protein functionality may be directly related to change in cholesterol levels in the plasma membrane, but may also be due to artifacts associated with cholesterol depletion such as cytoskeletal destabilization (35) or due to cholesterol's effect on a different protein or cofactor not included in the current model such as PIP_2 (36). Another critical question is whether raft association induces a protein conformational change or change in oligomerization state (37-39). Changes in cholesterol have been shown to critically affect the functionality of a class of protein known as the integrins, but the interplay between integrin-ligand association and the formation of microclusters of integrins in cell membranes are not well understood. For this reason, integrins are a good candidate for separating out different lipid raft-related effects on protein functionality.

Artificial lipid bilayers, while reasonable mimetics of cell membranes for some purposes (40-42), do a poor job of mimicking the elastic properties of cell membranes because pure lipid bilayers are much softer than cell membranes (43, 44). The proteins embedded in cell membranes and the protein linkages between the membrane and

extracellular and intracellular matrices significantly affect the biophysical properties of the cell's bilayers, including the bending modulus, the compressibility modulus, and the shear modulus (45). To overcome this, self-assembling actin filaments were added to lipid vesicles and the mechanical features of that system were determined using optical tweezers (46). One definite advantage that vesicles have over planar systems is that they have a built-in curvature due to their shape, and therefore can more closely mimic round cells. They still, unfortunately have similar difficulties for determining the elastic properties as cells themselves, again due to the shape constraint. Another way to increase the compressibility and bending stiffness of model lipid bilayers is through the addition of lipopolymers. Lipopolymers incorporated into model membranes, either into liposomes or planar solid-supported bilayers, can significantly alter biophysical properties including bending modulus and compressibility, depending on polymer type, weight, and concentration (47, 48).

Planar supported lipid bilayers enriched in low concentrations of lipopolymers in the bottom layer are extremely useful model membranes because the polymer uplifts the bilayer from the underlying substrate with a cushion that enables the incorporation of transmembrane proteins (49) and aids in constructing lipid bilayers that separate into liquid ordered (l_o) CHOL-rich regions and liquid disordered (l_d) CHOL-poor regions (42, 50). Membrane proteins, including lipid-anchored proteins and transmembrane proteins, have been successfully incorporated into phase-separating model lipid bilayers constructed of either planar supported lipid bilayers, giant unilamellar vesicles (GUVs) or giant plasma membrane vesicles (GPMVs) to study the intrinsic sequestration of

receptors and the role of crosslinking agents (22, 40, 51-55). Early supported lipid bilayer studies showed promise (53). Raft-associated proteins correctly sequestered to l_o phases in model systems comprised of supported lipid bilayers or monolayers (53, 54, 56), but raft-associated proteins sequestered preferentially to l_d phases in model systems consisting of GUVs (52, 57) and transmembrane raft-associated proteins also displayed preferences for l_d phases in GPMVs (55, 58). Several groups did observe higher partition coefficients upon crosslinking of raft-associated proteins with antibodies or addition of gangioside GM1 (GM1) cross-linked to cholera toxin B (CTxB) (52, 56, 59). The elegance of model systems, however, is that it is possible to study how the addition of ligands affects raft partitioning and oligomerization without the use of cross-linking agents.

The research described within this dissertation contains two distinct sets of objectives in which lipopolymers are incorporated into lipid monolayers and bilayers to study membrane properties at the microscopic level and at the molecular level. The first set of objectives relate to membrane stiffness and elasticity. It will be shown below that high concentrations of lipopolymers in lipid monolayers are capable of inducing buckle-driven delamination of a lipid monolayer deposited onto a glass substrate, and that such buckles can act as diffusion barriers when the monolayers are used to construct fluid bilayers. In addition, it is possible to systematically analyze the elastic properties of lipopolymer-enriched lipid monolayers through the study of buckling parameters of varying lipopolymer concentrations.

The second set of objectives involves protein studies on polymer-tethered CHOL enriched model membranes. These objectives will be to first confirm the fluid incorporation of correctly-oriented transmembrane proteins ($\alpha_v\beta_3$ and $\alpha_5\beta_1$) into polymer-tethered lipid bilayers. The second objective is to use phase-separating lipid mixtures to determine integrin partitioning between l_o and l_d phases for $\alpha_v\beta_3$ and $\alpha_5\beta_1$ integrins before and after ligand binding in the absence of crosslinking agents. The third objective is to determine the protein oligomerization state in l_o and l_d phases for $\alpha_v\beta_3$ and $\alpha_5\beta_1$ integrins before and after ligand binding and to systematically analyze the degree of oligomerization of $\alpha_v\beta_3$ and $\alpha_5\beta_1$ integrins before and after ligand binding in model membranes with increasing concentrations of CHOL.

1.2 Organization

This dissertation is organized into five chapters. The first chapter provides the rationale and key objectives of this study and describes the organizational structure of the dissertation. The second chapter introduces various methods and instrumentation used in this research. The second chapter also contains theoretical introductions to the theory of thin film wrinkling and delamination, biophysical properties of lipid-lipopolymer mixtures, and the role of CHOL in lipid bilayers. The third chapter details the materials and technical procedures used to contruct the model monolayers and bilayers, analyze the properties of the monolayers and bilayers through epifluorescence (EPI) microscopy, atomic force microscopy (AFM), and confocal spectroscopy including fluorescence fluctuation spectroscopy (FFS). It also outlines the key equations necessary for determining thickness and bending rigidity of lipid/lipopolymer mixtures, critical stress,

loading parameter and other buckling-related parameters, and the construction and testing of the photon counting histogram algorithm required for determination of oligomerization state.

CHAPTER 2 BACKGROUND

2.1 Methodology

2.1.1 Langmuir Films

Benjamin Franklin once poured a teaspoon of oil into the pond at Clapham Common in London and noted that the oil produced a calm area on the surface which spread, eventually, to cover perhaps half an acre. If the oil were olive oil, say a triglyceride of oleic acid, and it actually did cover half an acre, or 2025 m^2 of water, and it spread to make a layer of oil one molecule thick, that corresponds to an area per lipid molecule of 66 $Å^2$. Surprisingly, this is very similar to the area per molecule for a monolayer of unsaturated phospholipids compressed to physiologically relevant pressures. A Langmuir film is a monolayer of an organic substance that forms at the air-water interface. Langmuir monolayers can be thought of as two dimensional fluids. A typical pressure area isotherm for a phospholipid is shown in Fig. 2.1.1 for the substance 1,2-dipalmitoyl-*sn*-glycero-3-phosphocholine (DPPC). At very large area per molecule, there is no change in surface tension and the material at the air-water interface is in a two-dimensional gaseous phase (G). (By convention, surface pressure is defined as the change from pure water at 72 mN/m so that as surface *tension* decreases, surface *pressure*

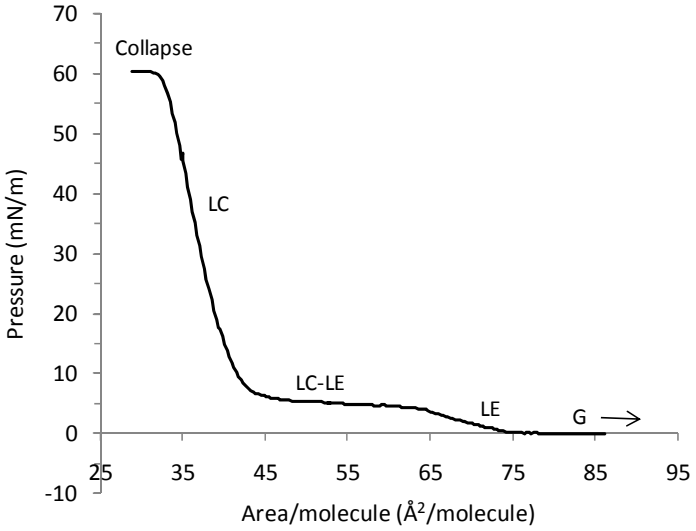

Figure 2.1.1 Pressure-area isotherm of DPPC at 295 K showing different phases: gaseous (G), liquid-expanded (LE), liquid condensed (LC) and a mixed LC-LE phase

increases). At decreased area per molecule, the surface pressure begins to increase slowly and the substance may enter a liquid expanded (LE) phase. Compressed further, the substance shifts to a liquid condensed (LC) phase, or possibly a gel phase, unless the monolayer ruptures and starts to form a second layer on top of the first layer. This is known as collapse. When the system is undergoing a phase change, the pressure-area isotherm will exhibit a straight horizontal line, that is, the pressure will not change substantially for large changes in area per molecule. For the DPPC pressure-area isotherm in Fig. 2.1.1, there is a phase change shown between the LE and LC phases.

2.1.2 Langmuir-Blodgett/Langmuir-Schaefer (LB/LS) Film Deposition

Langmuir films are particularly useful for constructing bilayers of varying or asymmetric lipid composition. Lipids align as monolayers with their hydrophilic head groups pointed toward the water and their hydrophobic tails away from the water. Lipid bilayers can be assembled on Langmuir troughs, which are simply troughs equipped with a variable barrier arm for changing the total surface area, a motorized dipping arm, a surface pressure detector, and a feedback loop enabling the barrier arm to change the total area in response to changes in the surface pressure. A schematic of a Langmuir trough showing the two stages of Langmuir-Blodgett (LB)/Langmuir-Schaefer(LS) film deposition is shown in Fig. 2.1.2, for a phospholipid bilayer with a physisorbed lipopolymer tether.

It is possible to transfer Langmuir films onto a solid substrate by combining two techniques referred to as LB deposition and LS deposition (60, 61). For the leaflet closer to the substrate, LB deposition involves immersing a substrate in the aqueous subphase, and slowly raising the substrate through the air-water interface while maintaining a constant surface pressure, as shown in Fig. 2.1.2(*A*). This transfers a monolayer so that the hydrophilic headgroups are closer to the substrate and the hydrophobic tails are pointed away from the substrate. To complete the bilayer, LS deposition involves pressing the substrate down onto the monolayer and capturing the substrate and bilayer within a depression slide. The process is shown in Fig. 2.1.2(*B*). This transfers a monolayer so that the lipid tails are adjacent to the lipid tails of LB layer, forming a fluid bilayer. The bilayer, trapped with a water layer between the depression slide and the

glass substrate, is shown in Fig. 2.1.2(*C*). It can be opened subsequently under water for addition of proteins or other lipids to the bilayer. The method is quite useful for making asymmetric bilayers because the composition of each leaflet can be adjusted independently. In particular, it is useful to add a variable fraction of a polymer-tethered phospholipid to the LB mixture, as depicted in Fig. 2.1.2.

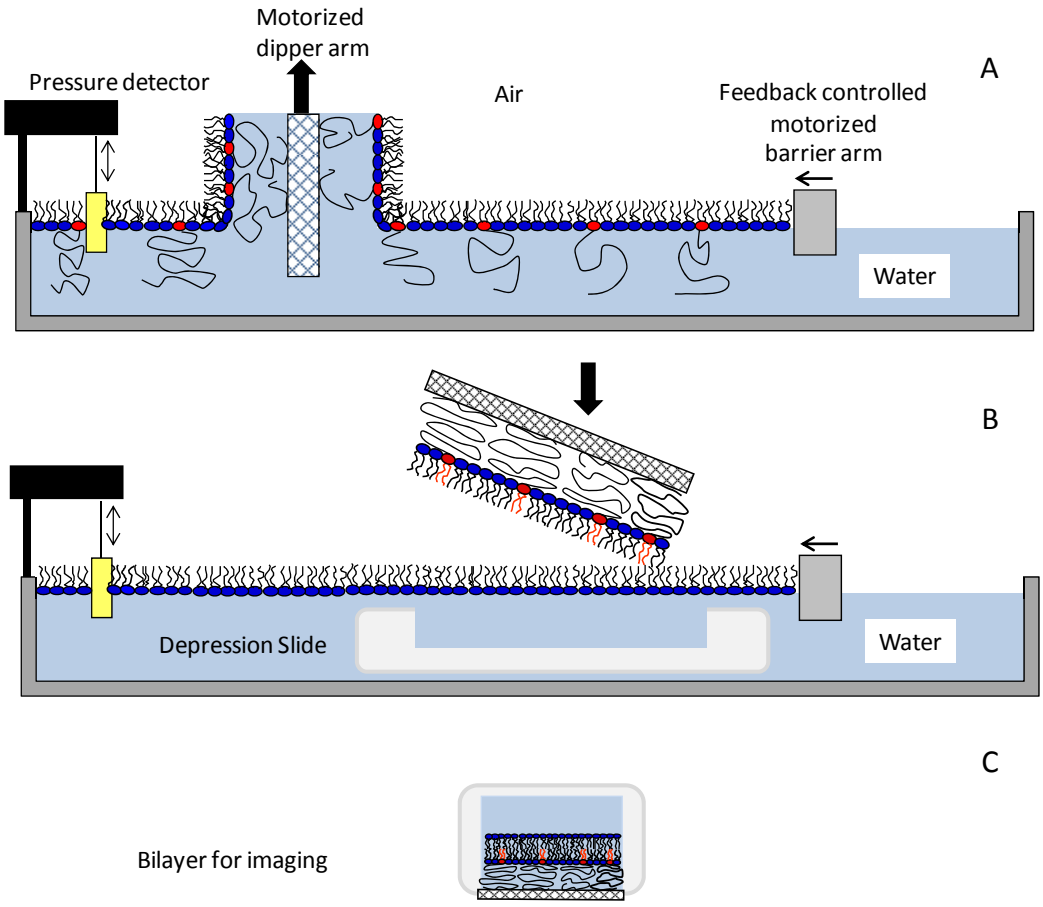

Figure 2.1.2 (A) Langmuir-Blodgett dipping of physisorbed polymer tethered lipid monolayer onto solid substrate. Lipopolymers (acting as polymer tethers) are shown as red lipids covalently attached to black hydrophilic polymers. (B) Langmuir-Schaefer transfer of upper leaflet of phospholipids onto substrate to complete the bilayer. (C) Physisorbed polymer-tethered fluid lipid bilayer sandwiched between solid substrate and depression slide

2.1.3 Epifluorescence Microscopy (EPI)

EPI microscopy is a widefield optical technique whereby a fluorescent sample is illuminated by a light source of one range of wavelengths, is excited, and emits photons at a different, longer wavelength. Through use of filters, only the emitted photons are collected. The excitation source most commonly used is a mercury discharge arc lamp whose output is passed through a dichroic filter. The output is again passed through an emission filter so that only the red-shifted emissions are collected by a charge coupled device (CCD) camera, the output of which is displayed on a workstation. Research was conducted on a microscope with both EPI microscopy and fluorescent fluctuation spectroscopy (FFS) capabilities, and a schematic is shown in Fig. 2.1.3.

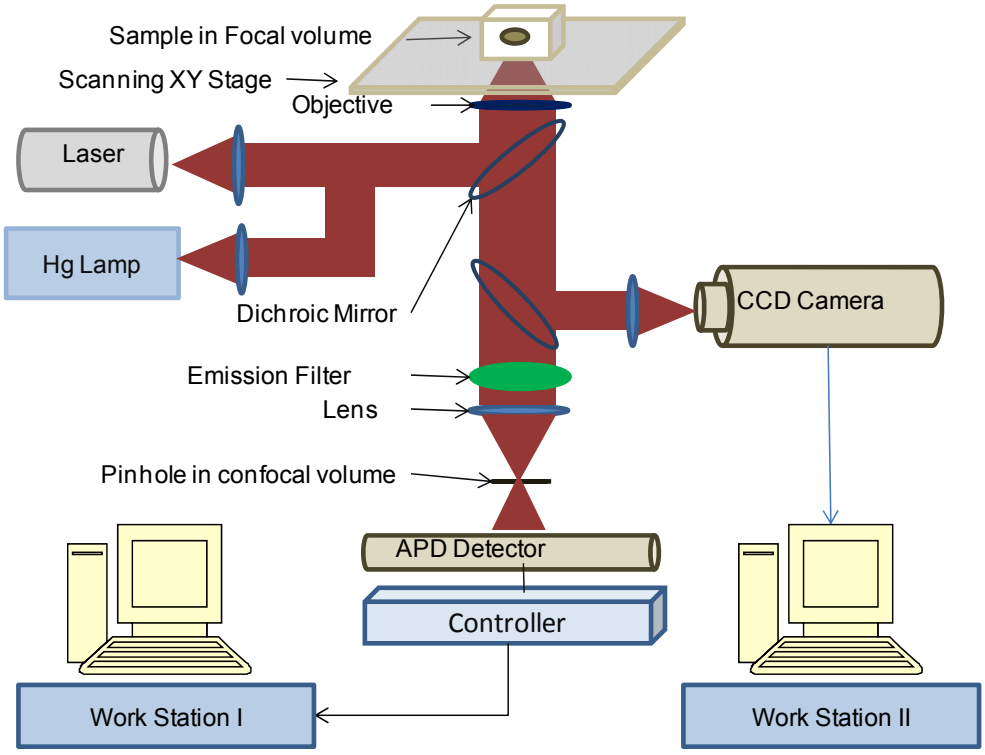

Figure 2.1.3 Microscope configuration for EPI microscopy and fluorescence fluctuation spectroscopy

2.1.3.1 Fluorescence Recovery After Photobleaching (FRAP)

Fluorescence recovery after photobleaching, a common technique in EPI microscopy, is used to determine diffusion coefficients for a bulk sample in two or three dimensions, but works especially well on two dimensional fluid surfaces such as planar bilayers and cell membranes. A small spot in a fluid sample is irrevocably photobleached, creating a dark spot. For a fluid sample, the unbleached fluorophores in the sample will randomly diffuse until it is no longer possible to distinguish the original bleaching spot. From the size of the bleach spot (w_{BS}) and the time it takes for the fluorescence within the bleaching spot to return to half brightness ($\tau_{1/2}$) , it is possible to determine the diffusion coefficient (D_{diff}) for the diffusing fluorophores from the following relation (62)

$$D_{diff} = \frac{w_{BS}^{2}}{4\tau_{1/2}\gamma_{D}} \qquad (2.1.1)$$

The variable γ_D is a correction factor that depends on the laser line and the bleach time. Should any part of the bleaching spot (or volume) not recover there are said to be immobilized particles and the immobile fraction (IF) can be calculated as the ratio of the intensity within the bleach spot to the ratio of intensity of a spot that was not bleached. This is different than the immobile fraction calculated from wide field single molecule fluorescence microscopy, where the immobile fraction is the fraction of jumps that are smaller than the jump tracked for an immobilized particle (61).

FRAP over a long time period is also excellent for determining diffusion barriers in an otherwise fluid sample. While individual immobilized particles do not significantly affect the capacity for mobile particles to diffuse around them, if the immobilized

particles form a diffusion barrier, the fluorescence recovery will be seen to occur only along channels or within compartments and not through such barriers.

2.1.3.2 Other Image Analysis Techniques

Beyond FRAP, EPI micrographs of lipid bilayers can provide a wide variety of qualitative and quantitative data. Qualitatively, EPI micrographs of fluorescently labeled proteins can show whether the labeled species are distributed homogeneously. Phase separations can be visualized, including polymer buckles and lipid phase separations. Finally, it is possible to acquire quantitative data about the concentration of species illuminated and recorded in the micrograph (63).

2.1.4 Atomic Force Microscopy (AFM)

AFM is a scanning probe technique than has sub-nanometer three dimensional resolution. Developed in the 1980's, AFM provides accurate information on small height changes by scanning with a very small probe (typical tip width 40 nm) attached to a cantilever of known stiffness (64). A schematic is shown in Fig. 2.1.4.

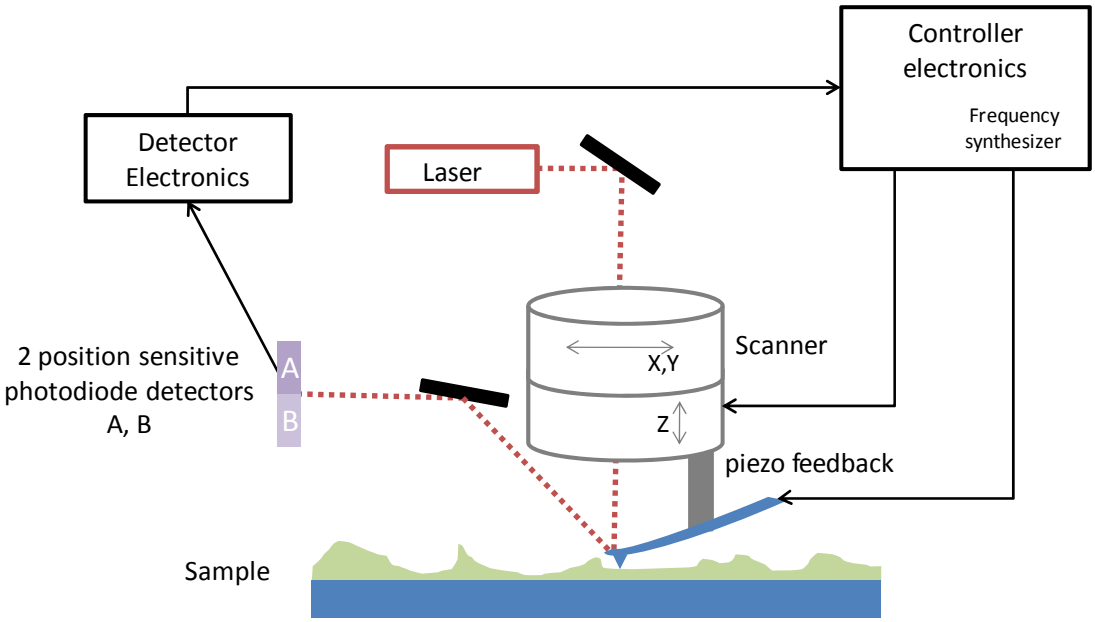

Figure 2.1.4 Schematic of atomic force microscope showing cantilever suspended over a soft substrate

In the tapping mode, most useful for soft samples such as lipid monolayers and bilayers, a probe (tip) oscillates at a known frequency and a laser beam is focused on the oscillating tip and through mirrors to photodiode detectors. As the tip senses a surface, either through direct contact or short range forces near the surface, changes in the height and stiffness of the sample induce changes in the amplitude and phase of the tip's oscillations which are detected by the photodiodes. This information is relayed back as the piezoelectric response for that position. The cantilever moves a short distance and a response is recorded at the new position. By scanning a sample, a three dimensional surface of the sample can be obtained. While analysis of the laser beam's location can only detect position changes on the order of 10 nm, due to the length of the laser beam path from tip to detector, this translates to sensitivities greater than 1 nm on the surface.

2.1.5 Fluorescence Fluctuation Spectroscopy (FFS)

A schematic of the equipment set-up for FFS, which encompasses both fluorescence correlation spectroscopy (FCS) and brightness analysis methods such as the photon counting histogram (PCH), was shown in Fig. 2.1.3. A laser beam passes through a beam splitter and then is focused with a high numerical aperture objective to a focal volume within a larger sample of freely diffusing fluorescent particles. Fluorescence emissions from within this volume pass back through the beam splitter and are focused onto a confocal volume. A pinhole in the axial plane of the confocal volume is introduced to further limit stray fluorescence and detectors are placed to acquire, at submicrosecond intervals, the total fluorescence detected within the confocal volume. The concept underlying FCS is that analysis of the fluctuations in intensity of fluorescent particles through a small volume in an unperturbed sample will give a complete kinetic description of the system containing the sample (65). This is done by analyzing the rate of change of fluorescence over different time length scales and generating an autocorrelation curve. By contrast, the motivational basis for PCH is the probability distribution of the discrete amplitudes which comprise the fluorescent trace, collected over time, can give a full description of the number and the brightness of species within a volume by aggregating the statistics of the intensities (photon counts) collected over time into a photon counting histogram. FCS, which analyzes intensity fluctuations, can sensitively determine the diffusion rate of fluorescent particles whereas PCH, which analyzes the frequency of different amplitudes of intensity more accurately determines average molecular number and brightness of fluorescent particles but does not determine rates of diffusion at all. In either case, data acquisition remains the same. Fig. 2.1.5 shows a photon counting

histogram (A), a fluctuation trace over time (B), and an autocorrelation fitting curve (C) of the fluctuation traces of rhodamine 6G (R6G) in solution for two different 10 s data acquisition sets.

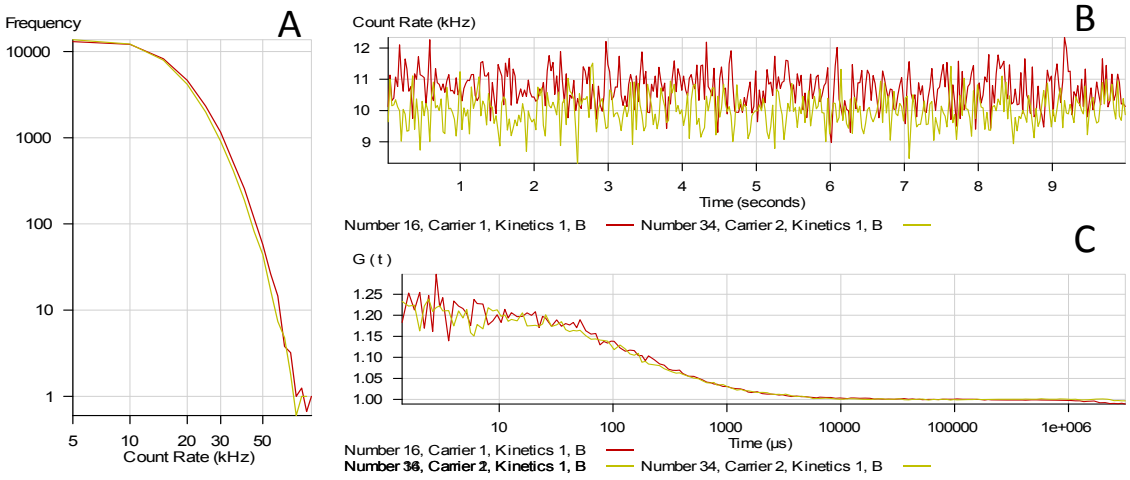

Figure 2.1.5 (A) Histogram of photon counts of R6G collected during a 10 s trace for two channels. (B) Fluctuation of intensity collected for a 10 s trace, time-binned. (C) Autocorrelation curves

2.1.5.1 Photon Counting Histogram (PCH)

It is expected that for random processes, the location of any one particle within the volume will be governed by a Poisson distribution. The shape of a Poisson distribution for discrete values of k is as follows, where λ is the expected number of occurrences.

$$Poisson(k,\lambda) = \frac{(\lambda)^k e^{-\lambda}}{k!} \qquad (2.1.2)$$

The brightness of a particle registered by a photon counter will depend on its position in the sample space and can be described by a point spread function (PSF) so that a particle of brightness ε which is at the exact center of the volume will show an intensity I_o but at a

distance *(r,z)* from the center, where r is radial distance and z the axial distance, the brightness will be less and intensity can be described as:

$$I(r,z) = PSF(r,z) \cdot I_o. \quad (2.1.3)$$

Finally, the number of particles within the confocal volume will also be governed by a Poisson probability distribution. These three statements were elegantly translated into an analytical tool to evaluate photon counting histograms such as those shown in Fig. 2.1.5(*A*) for use with modern microscopy by Enrico Gratton and colleagues in the late 1990's (66). While Gratton's set-up utilized a two-photon excitation microscope, others extended the system to one-photon excitation (67). The mathematical details of the photon counting histogram, as well as some limitations, are described in Section 3.2.5.

2.1.5.2 Fluorescence Correlation Spectroscopy (FCS)

As noted above, FCS, which was developed as an analytical tool before PCH, can determine diffusion times through an observation volume as well as number and brightness of particles in the volume (65). FCS was originally conceived as a method to monitor chemical reactions non-invasively by measuring spontaneous fluctuations instead of perturbing a system and watching it return to equilibrium (68). The mathematical treatment of the fluctuations that generate this information is as follows. First, a PSF is again required and is taken to be a Gaussian. Next, the average intensity $\langle I(t) \rangle$ for the fluctuation trace (Fig. 2.1.5(*B*)) is found and the deviation from average intensity is defined as $\delta I(t) = I(t) - \langle I(t) \rangle$. For purely random processes, the temporal autocorrelation function is the correlation of a time series with itself, shifted by time τ, and normalized by the average intensity squared:

$$G(\tau) = 1 + \frac{\langle \delta I(t) \delta I(t+\tau) \rangle}{\langle I(t)^2 \rangle}. \quad (2.1.4)$$

The data can then be fitted to determine the characteristic diffusion time of a particle moving through a volume, τ_D, the average number of particles, N_{avg}, and a structure factor relating the ratio of the ellipticality of the Gaussian observation volume, Q, as follows (69)

$$G(t) = 1 + \frac{1}{N_{avg}} \left(\frac{1}{1+\tau/\tau_D} \right) \left(\frac{1}{\sqrt{1+(1/Q^2)(\tau/\tau_D)}} \right). \quad (2.1.5)$$

This is solved explicitly for the characteristic diffusion time (τ_D) and N_{avg}. The average brightness is determined by dividing $\langle I(t) \rangle$ by N_{avg}. The data are analyzed in real time by Zeiss ConfoCor2 software with no further analysis necessary, other than to note that, from experience, the system provides the greatest reliability for 1-20 particles in the focal volume and total intensities that average less than 500 photon counts (kHz).

2.2 Thin Film Wrinkling and Delamination

Ultrathin elastic sheets subjected to lateral stress will wrinkle, and depending on the force of the lateral stress and the relative stiffness of the substrate next to the thin film, will delaminate and buckle. This phenomenon is observed on all length scales, from geological features such as the Canadian Rockies (Fig. 2.2.1(*left*)) (70) to children's kites and space satellites (71) to elastomer-metal hybrid bilayers 60 nm thick (72) to an LB monolayer of a lipid-lipopolymer (Fig. 2.2.1(*right*)). In the case of polymeric thin films, wrinkling or buckling patterns can be exploited to fabricate patterned surfaces (72-74). Mixed lipid monolayers at the air-water interface normally squeeze out lipids when

subjected to high lateral pressures, and these lipids do not recover on relaxing the pressure. However, if the lipid mixture is enriched with 3-10 mol% lung surfactant protein, the monolayer will exhibit reversible buckling in the water (75). For thin films subject to compressive stresses, wrinkling occurs when the compressive strain is less than a critical wrinkling strain (76). Delamination and buckling occur depending on the strength of the adhesive force between the substrate and the thin film as well as the ratio of the plane-strain moduli of the substrate and the film, so that the more similar the plane strain moduli, the more likely wrinkles will be produced rather than buckles, even at larger compressive forces (76).

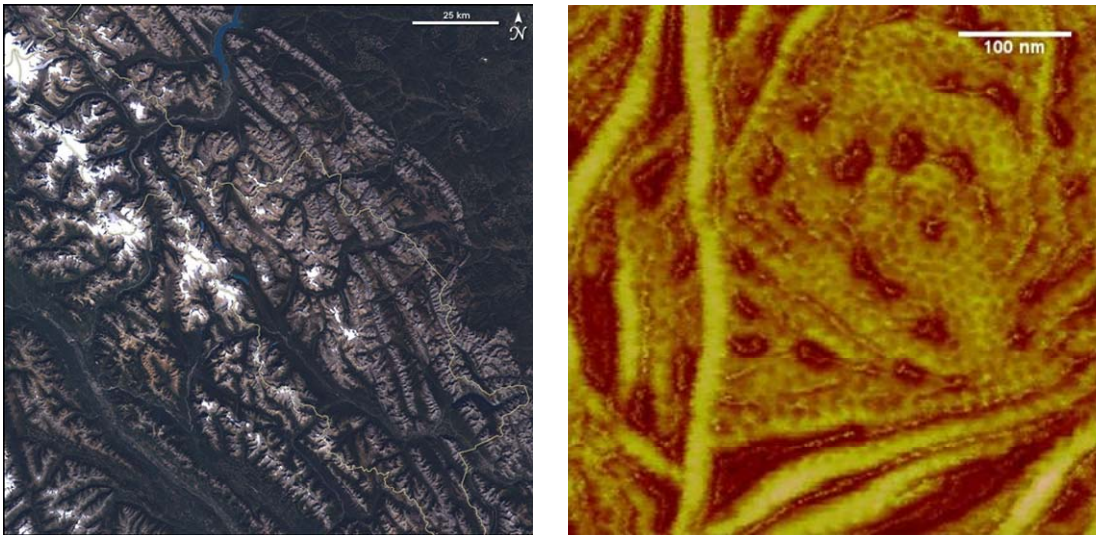

Figure 2.2.1 Left - Satellite photo of Banff National Park, Banff, Canada. Visible Earth project c. NASA and provided for use without restriction. Summit of Banff National Park is 2281 m ASL, 900 m above the town of Banff. Right - Detail of buckling structure of 40 mol% DSPE-PEG5000 /SOPC monolayer. Peaks of buckled structure on right are 8 nm above lowest point. Scale bars: left = 25 km, right, 100 nm

2.3 Biophysical Properties of Lipid-Lipopolymer Mixtures

The grafting of a polymer onto the head group of a lipid and then mixing the polymer-grafted lipids in with phospholipids into monolayers and bilayers provides a thin film with properties distinct from its components. Due to the usefulness of long-lasting liposomes comprised of mixtures of lipids and lipopolymers, a great deal of theoretical work has been undertaken on certain biophysical aspects of these mixed assemblies (47, 48, 77). For the current studies, the parameters of greatest interest are the height and bending stiffness of the monolayers. These can be deduced from experimentally determined values of a few physical parameters of the polymers, including the length of a unit monomer, the number of monomers in the polymer chain, the mole fraction of lipopolymers on a monolayer, and the height and bending stiffness of a monolayer of lipids in the absence of lipopolymers (47, 78). The formulae connecting these data will be described in detail in Section 3.2.5.

2.4 The Role of Cholesterol in Lipid Bilayers

The plasma membrane is a fluid lipid bilayer primarily composed of phospholipids, ceramides, CHOL and membrane proteins (79). The phospholipids and ceramides are amphipathic with charged or zwitterionic head groups and long carbon chains, generally around 16-20 carbons in length. The membrane proteins may contain transmembrane domains or lipid anchors attached to protein head groups that extend into either

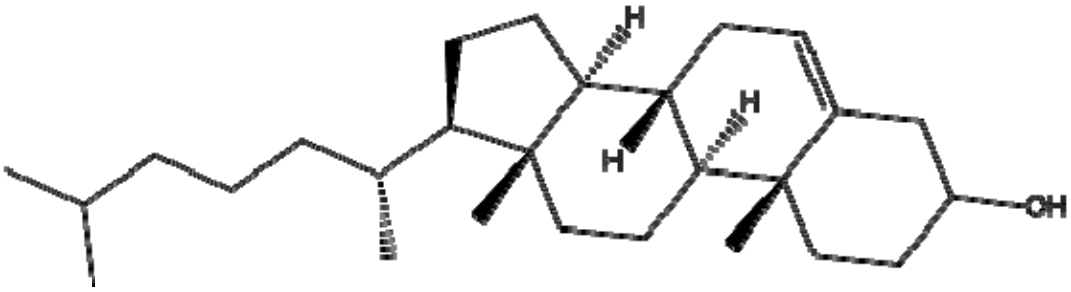

Figure 2.4.1 Cholesterol

the cytosol or the exterior face. CHOL, shown in Fig. 2.4.1, modulates the interactions between the lipids and proteins in many ways which are poorly understood and of intense interest (80). CHOL affects other lipids in a bilayer in a number of ways. With respect to size, CHOL is shorter than the phospholipids, and unlike the phospholipids, has no charged head group. Cholesterol sits within a membrane with its hydroxyl group interacting with the charged lipid head group and shielded from water. The sterol component next to the hydroxyl group is rigid and stiffens the bilayer, making the bilayer less permeable to small charged molecules. The effect of CHOL intercalating between lipids in this fashion increases the width of a bilayer, and decreases phospholipid fluidity both translationally and rotationally (81, 82). Interestingly, in model bilayers, CHOL is an "averager," disrupting packed, gel phase bilayers of saturated lipids to induce a less ordered state and organizing fluid liquid phase bilayers of unsaturated lipids into a state of greater lipid order (82). In fact, in model bilayers, as noted in Section 1.1, certain ternary mixtures of saturated lipids, unsaturated lipids and CHOL phase separate into two intermediate phases. The phases are known as the liquid ordered (l_o) phase composed primarily of CHOL and saturated lipids, and the liquid disordered phase (l_d) composed primarily of CHOL and unsaturated lipids (83). These two phases are thought to mimic

roughly the cholesterol content of lipid raft domains (l_d) and non-raft domains (l_d) in plasma membranes.

It is possible to study the effects of CHOL on proteins without studying transient lipid rafts on the plasma membrane directly by using polymer-tether supported lipid bilayers, as described below in Chapters 3 and 4. Here, a polymer tether enables the reconstitution of transmembrane proteins into these model systems, on which it is possible to vary levels of CHOL both in binary lipid mixtures as well as by using ternary mixtures with large, stable patches of l_o regions and l_d regions. With a ternary system, it is also possible to identify the biophysical preference of a membrane protein for either l_o or l_d phases in the absence or presence of other biochemical signals. Importantly, the planar nature of the system and its low background compared to live cells permits sophisticated FFS analysis of the lipids and proteins at the single molecule level.

2.5 Overview of Integrins $\alpha_v\beta_3$ and $\alpha_5\beta_1$

Integrins are a class of membrane proteins that are involved in many cellular functions including cell adhesion, morphology, motility, angiogenesis and they act as bidirectional signaling platforms (84, 85). These processes are thought to be regulated by lipid rafts as well as cytosolic proteins that bind to integrins, such as talin, and extracellular matrix (ECM) ligands including FN and VN. Integrins are comprised of two noncovalently bound subunits, an α subunit and a β subunit. Both subunits have large extracellular domains that in a resting state form a bend back toward the membrane. The ligand binding area is roughly in the middle at the top of the unit, which means that it

is not very far from the membrane. Both subunits have single membrane-spanning domains and short cytosolic domains. Currently, there is no crystal structure for an entire integrin, but Figure 2.5.1 shows a ribbon representation of a structure for both extracellular domains with the first 5 transmembrane peptides (86). The structure is oriented as if it were directly above the plane of the membrane. As described below in Section 3.2.2, inegrins are incorporated into previously constructed bilayers with no assurance their orientation will include the extracellular domain above the bilayer and accessible to ligands. However, by adding fluorescent tags to antibodies that bind to the EC domains after incorporation of the proteins into the bilayer, the current experimental set-up ensures that only correctly oriented integrins will be seen fluorescently.

Integrin functionality is regulated by ligand binding, cytosolic binding, and microclustering, as well as other protein-protein interactions. The cation Mn^{2+} has also been shown to increase integrin activity. Artificial crosslinking of integrins enhances their activity (87), as does Mn^{2+} (88). Moreover, cholesterol depletion in a plasma membrane decreases the clustering of wild type integrins, but not mutant integrins for which the mutation caused the integrin to be constitutively in a different conformation (33). Given the relative ease of incorporating integrins into model membranes and the relative difficulty in isolating the many potential factors regulating integrin functionality in the plasma membrane, they are a promising candidate for model studies. The specific integrins chosen, $\alpha_v\beta_3$ and $\alpha_5\beta_1$, are important because they are critically involved in angiogenesis, particularly cellular adhesion and cell motility ($\alpha_v\beta_3$ and $\alpha_5\beta_1$)(88), and tumorigenicity ($\alpha_v\beta_3$) (89).

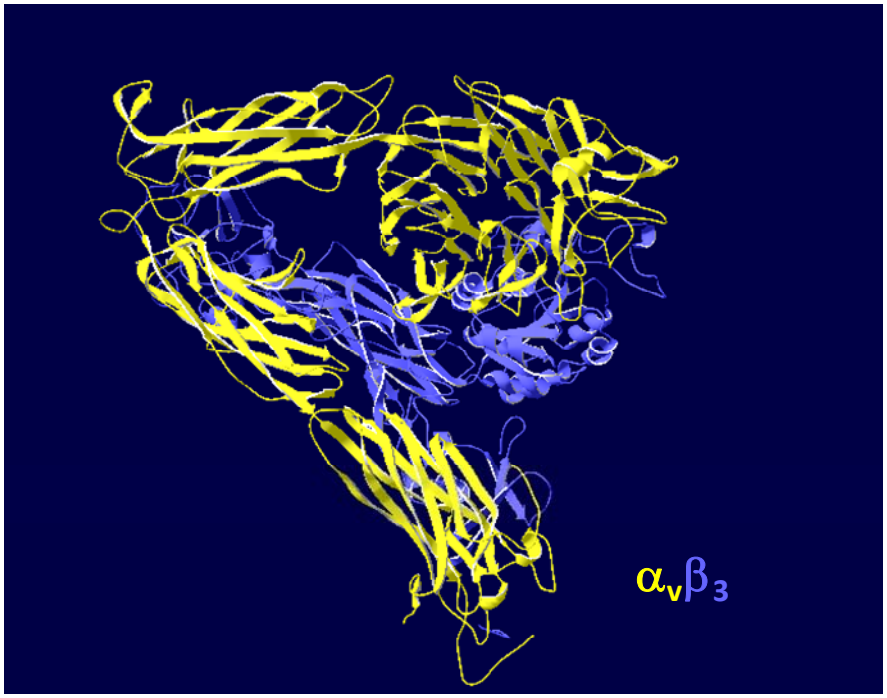

Figure 2.5.1 Ribbon representation of crystal structure of EC domains of $\alpha_v\beta_3$, with α subunit in yellow and β sub-unit in blue. Protein is in a folded conformation and oriented as if just above a plasma membrane

CHAPTER 3 MATERIALS AND EXPERIMENTAL PROCEDURES

3.1 Materials

The lipopolymer dioctadecylamine poly(2-ethyl-2-oxazoline)$_{85}$ (DODA-E$_{85}$) was synthesized in the laboratory of Jürgen Rühe following a procedure described previously (90). The lipopolymers 1,2-dioctadecyl-*sn*-glycero-3-*N*-poly(2-methyl-2-oxazoline)$_{50}$ (diC$_{18}$M$_{50}$), 1,2-dioctadecyl-*sn*-glycero-3-*N*-poly(2-ethyl-2-oxazoline)$_{50}$ (diC$_{18}$E$_{50}$), and 1,2-dioctadecyl-*sn*-glycero-3-*N*-poly(2-ethyl-2-oxazoline)$_{50}$ with a terminal fluorescence label of 6-tetramethylrhodamine[-isothiocyanate] (diC$_{18}$E$_{50}$-TRITC) were synthesized in the laboratory of Rainer Jordan following procedures described previously (91-93). Lipids and lipopolymers including 1-stearoyl-2-oleoyl-*sn*-glycero-3-phosphocholine (SOPC), ammonium salt of 1,2-distearoyl-*sn*-glycero-3-phosphoethanolamine-*N*-[methoxy(polyethylene glycol)-5000] (DSPE-PEG5000), 1,2-dioleoyl-*sn*-glycero-3-phosphocholine (DOPC), 1,2-dipalmitoyl-*sn*-glycero-3-choline (DPPC), 1,2-dipalmitoyl-*sn*-glycero-3-phosphothioethanol (DPTE), CHOL, and ganglioside GM1 (bain, ovine-ammonium salt) were purchased from Avanti Polar Lipids (Alabaster, AL) and used without further modification. The lipopolymers DODA-E$_{85}$, diC$_{18}$E$_{50}$, diC$_{18}$M$_{50}$ and DSPE-PEG5000 are shown in Fig. 3.1.1.

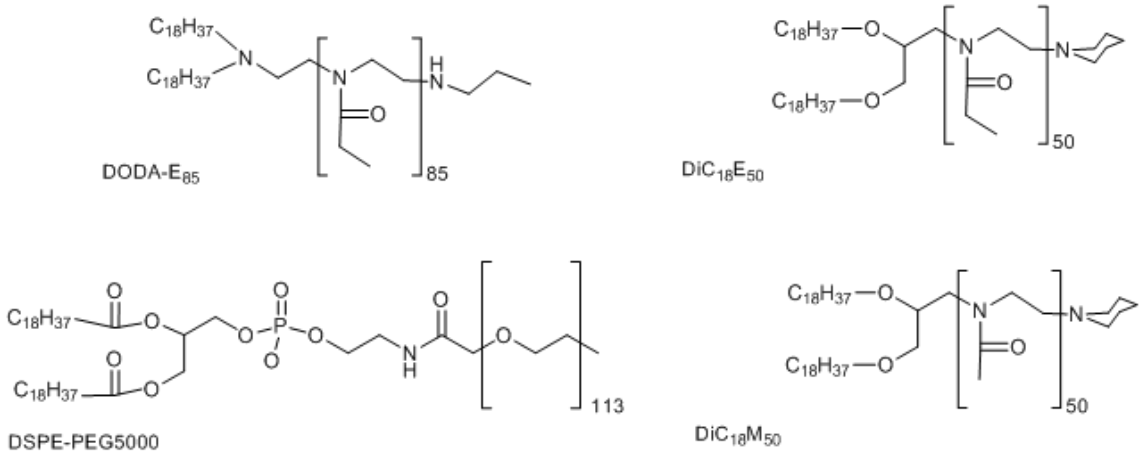

Figure 3.1.1 Lipopolymers DODA-E_{85}, DSPE-PEG5000, di$C_{18}E_{50}$, and di$C_{18}M_{50}$

Ultrapure water (Milli-Q) used in the preparation of lipid bilayers was provided via a Millipore Water Purification System (Milford, MA). Glass coverslips (24 x 40 mm, No. 1) were purchased from VWR Scientific Products (West Chester, PA) for EPI microscopy and from Thermo Fisher Scientific (Fisher Finest) (Waltham, MA) for FFS or combined EPI/FFS. Glass coverslips were prepared for use by baking in 515 °C oven for 1 h (VWR) or 3 h (Fisher Finest) and then sonicating in 1% SDS (30 min VWR, 45 min Fisher), followed by a thorough rinsing and sonicating in NaOH saturated MeOH (30 min VWR, 45 min Fisher), followed by thorough rinsing and sonicating in Milli-Q (5 min), followed by sonicating in 0.1% HCl (30 min VWR, 45 min Fisher) and a last rinsing and sonication in Milli-Q. All cleaning and buffer solutions were prepared using solvents and chemicals purchased through Thermo Fisher Scientific.

Proteins and antibodies were purchased from Millipore, Inc. (Billerica, MA). These included human integrin $\alpha_v\beta_3$, and human integrin $\alpha_5\beta_1$, both octyl-β-D-glucopyranoside

human purified protein, (VN), and human plasma fibronectin (purified protein) (FN). The kits for fluorescently labeling antibodies with TRITC or Alexa-555, and the fluorescent lipid probes triethylammonium salt of *N*-(6-tetramethylrhodaminethiocarbamoyl)-1,2-dihexadecanoyl-*sn*-glycero-3-phosphoethanolamine (*TRITC-DHPE*) and triethylammonium salt of (*N*-(7-nitrobenz-2-oxa-1,3-diazol- 4-yl)-1,2-dihexadecanoyl-*sn*-glycero-3-phosphoethanolamine) (NBD-PE) and Alexa-555 fluorescently labeled CTx B (CTxB-555) were purchased from Invitrogen. Rhodamine 6G (R6G) and octyl-β-D-glucopyranoside (OG) were purchased from Sigma-Aldrich (St. Louis, MO). Antibodies were labeled following procedures described in antibody labeling kits. Efficacy of labeling was checked by determining brightness through FCS. Lipopolymer-coated maleimide-functionalized quantum dots were graciously provided by members of the Naumann lab following a slightly modified version of the procedure described previously (94).

3.2 Experimental Procedures

3.2.1 LB/LS Deposition Techniques

Polymer-tethered phospholipid bilayers were built using successive LB and LS film transfers following standard procedures described before with slight modifications (60). To form the first (LB) monolayer, a chloroform solution of lipids and lipopolymers was spread at the air-water interface of a film balance equipped with dipper (Fig. 2.1.2) (Labcon, Darlington, UK). The composition was 5 mol% di$C_{18}M_{50}$ and 31.5 mol % DPPC and CHOL and 32% DOPC for TYPE I bilayers. For TYPE II bilayers, the

composition consisted of 5 mol% di$C_{18}M_{50}$ and 0, 5, or 30 mol% CHOL with the balance consisting of SOPC. Next the monolayer was compressed and, after stabilization (30 minutes for TYPE I bilayers or mixtures with > 10 mol% lipopolymer, 20 minutes for other mixtures), transferred to a prepared glass substrate at a film pressure of 32 $mN \bullet m^{-1}$ for TYPE II bilayers or 30 mN m^{-1} for other mixtures. Next, after surface-cleaning the trough, a fresh chloroform solution containing a lipid mixture was spread at the air-water interface and compressed to the same film pressure as the LB layer. The lipid mixture for the LS slide was the same as the lipid mixture for the LB slide but without the lipopolymer. For TYPE I bilayers, the three components were each increased proportionately in LS mixtures, for all other bilayers the lipopolymer was replaced with SOPC. LS transfer was accomplished by stabilizing the LS monolayer with a depression slide positioned underneath the air-water interface and then gently pushing the glass substrate containing the LB layer onto the underlying depression slide. For experiments incorporating proteins into bilayers, the depression slide was removed under water using a transfer dish and the bilayer placed into a Petri dish where Milli-Q was replaced by phosphate buffered solution (PBS) (Fisher Scientific, 10X concentration, diluted in Milli-Q).

3.2.2 Incorporation of Proteins into Bilayers

Proteins were reconstituted into model bilayers containing 5 mol% $DiC_{18}M_{50}$ in the LB layer using a modified Rigaud technique (95) as shown in Fig. 3.2.1. Micelle-stabilized membrane proteins (1.3×10^{-11} mol leading to bilayer concentrations of 10^{-3} mol%) were diluted 100x in PBS and added to the solution above the bilayer for 1.5-2 h

followed by removal of surfactant using a single layer (approximately 50 mg) of SM-2 biobeads (Bio-Rad, Hercules, CA) previously slurried in PBS and applied for 15 min. 1 g of biobeads suffice to soak up 117 mg of OG (96); thus a ten-fold excess was added (approximately). Fluorescently labeled monoclonal antibodies (MAbs) were then added for 2-4 h and excess antibodies were removed by rinsing. Antibodies routinely washed off and left no trace on TYPE II bilayers. For TYPE I mixtures, low levels of antibody adsorption occurred, for $\alpha_5\beta_1$ but not $\alpha_v\beta_3$ antibodies, if left on the bilayer over 12 h; therefore, antibodies were rinsed off within 4 h. FN or VN were added in 1:1 ratio to proteins and permitted to equilibrate 3-4 h or 12 h. Unbound FN or VN were removed by rinsing before imaging.

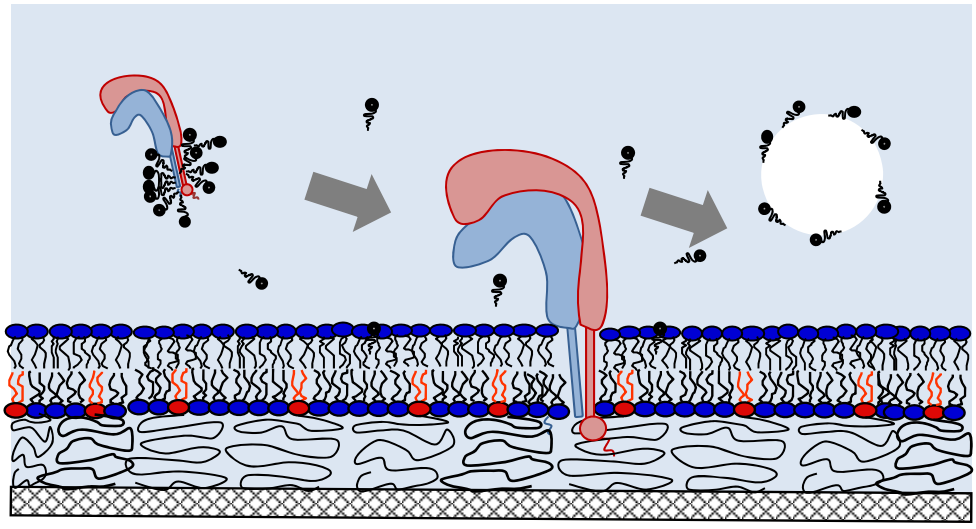

Figure 3.2.1 Membrane protein insertion into a polymer-tethered phospholipid bilayer, with removal of surfactants (black) with biobeads (white)

3.2.3 Combined EPI/FFS Data Acquisition

A commercial ConfoCor 2 (Zeiss, Jena, Germany) (schematic shown in Fig. 2.1.3) connected to an inverted optical microscope (Axiovert 200M, Zeiss, Oberkochen, Germany) was utilized for EPI microscopy and FFS. EPI was conducted using the optical microscope in epi-illumination (Axiovert 200M) where the beam was focused to the sample by a microscopy objective (Zeiss C-Apochromat, water immersion, 40x *NA* = 1.2 or Zeiss α plan-FLUAR TIRF, oil immersion, 100x *NA* = 1.45) with optovar magnification (1.6x). Appropriate filter sets for NBD-PE or Alexa-555/TRITC-DHPE were utilized; NBD-PE concentrations were chosen so no bleed through to the red channel was seen in the micrographs (less than 0.5 mol%). EPI was utilized for monolayer and bilayer analysis in the absence of proteins; in the presence of proteins a combined EPI/FFS data acquisition strategy was adopted.

FFS was conducted utilizing the C-Apochromat 40x objective. For FFS, the system was brought to thermal equilibrium to minimize drift, and data on protein distributions were acquired using a 1.8mW HeNe laser (wavelength 543nm, dichroic mirror and bandpass filter 550-605nm) excitation source and an appropriate dichroic mirror and bandpass filter (550-605nm). Data on NBD-PE distributions were acquired using a 30mW argon laser (wavelength 488nm) excitation source and an appropriate dichroic mirror and bandpass filter (505-530nm). TYPE I lipid mixtures induced phase separations into l_o and l_d domains, which were visualized by EPI either through low concentrations of NBD-PE or by protein distributions on the bilayer, and confirmed by subsequent addition of NBD-PE in fusogenic vesicles after completion of protein data

acquisition (94). Confocal spectroscopy XY (CS-XY) scans on TYPE I systems were accomplished for 10 x10 μm^2 areas using a 0.5μm step size and a low (7% for HeNe, 1% for Ar) laser power. These low powers minimized XY drift but did not eliminate entirely photobleaching of the sample. Control scans were performed in the absence of proteins to determine average background fluorescence, with and without low concentrations of NBD-PE, and then in the presence of proteins.

FFS data for the PCH analysis of proteins on bilayers were acquired using the 543nm HeNe laser (70% laser power) with runs of at least 50 s. Z directional focusing for proteins was done by a manual Z scan seeking to maximize fluorescence signal. Protein fluidity was confirmed by appropriate characteristic diffusion times, as determined by the ConfoCor2-generated autocorrelation curve. Data regarding protein brightness on the bilayer were also generated by the autocorrelation curve (using FCS), but were unreliable as overly influenced by background signal at the low protein concentrations utilized. The photon counting histograms ($h(k)$) were found by acquiring data from the ConfoCor2 graphs of frequency binned intensity data. These did not provide bins with zero count rates. To ensure the data were sufficiently robust above background for the low concentration of diffusing proteins on the bilayer, the intensity trace was also analyzed. It was found that when the average signal for the top 1% of the counts collected by the intensity trace were at least 20x above average background or more, sufficient data were available to fit the PCH data to a PCH algorithm-generated curve. FFS data were acquired for labeled antibodies and different dyes in solution as well as for TRITC-DHPE incorporated into fluid bilayers.

3.2.3.1 Fluorophore Concentration Determinations from Image Analysis

EPI studies analyzing relative concentrations of lipids and lipopolymers on monolayers and bilayers through intensity analysis were undertaken on the Axiovert200 utilizing a Zeiss AxioCam MRm monochrome digital camera and Axiovision 4.8 software. The exposure time for each micrograph was 50 ms. This generated consistent micrographs with a range of gray values (ranging from 32 for background to 3600 for monolayers with 0.8 mol% TRITC-DHPE), which correspond to the relative quantities of TRITC-DHPE or diC18E50-TRITC in different regions of the micrographs. The micrographs contained two distinct regions, "bright phase" and "dark phase" and associated gray values were found for a representative sample of regions and micrographs for three different dye concentrations. A monolayer with no dye was also imaged (using FFS to focus the sample) in order to obtain appropriate background values. To compare the relative gray values between the fluorescently labeled lipids and the fluorescently labeled lipopolymers, the mean gray value for the bright region of the 0.8 mol% TRITC-DHPE monolayer and the 0.8 mol% di$C_{18}E_{50}$-TRITC monolayer were each assigned the value of 1,000 a.u. (arbitrary units) and the rest of the gray values for each series were calculated relative to that number, in a.u.

3.2.3.2 Compartment Size, Buckle Width Determination, Fractal Dimension and FRAP Information from Image Analysis

Determination of compartment sizes in the 30 mol% DODA-E_{85} bilayers using EPI microscopy were performed on images acquired with a CoolSNAP$_{fx}$ CCD camera (Roper Scientific, Princeton, NJ) and Roper Scientific imaging software. FRAP was performed by closing the field stop on the microscope to its smallest diameter and permitting the Hg

light source (AttoArc HBO 100 Watt) to bleach the sample for 30 s. Two minutes or more passed before a subsequent EPI image was taken to show recovery. Size distribution of the compartments was determined using image analysis (Axiovision software). Here we determined a statistically significant number of compartment areas from different sections of the membrane. The average and standard deviation were then determined for the set of analyzed compartments. This procedure was repeated on different samples to ensure reproducibility in average compartment size. It was also possible to determine average compartment size in a completely independent fashion from single molecule fluorescence microscopy, utilizing $\langle r^2 \rangle$ *vs*. *t* plots from long-range single molecule diffusion studies (60).

For the monolayer studies involving DSPE-PEG5000, buckle width on monolayers and percent coverage of a monolayer by buckles was determined using Axiovision software (Zeiss) or Imagej, free software available at the NIH website. Determination of the fractal dimension, D_{corral}, of the corrals was performed using standard Box Count analysis available with the Imagej software (97). First, the images of interest were converted to binary images and then the fractal box count tool was applied to give a value. The procedure was repeated on different regions of the monolayer and on 2 different slides. The theory of fractal dimension through box counting is that boxes of progressively smaller sizes are used to tile a binary image. The number of boxes required to tile the image ($N(r)$) are collected as a function of the box size (r) and the box counting dimension, D, is defined as

$$D = \lim_{r \to 0} [\log N(r) / \log(1/r)].$$

3.2.3.3 Partition Coefficient and Migration Fraction from Confocal Spectroscopy-XY Scan Data

Partition coefficients (K_p (l_o/l_d)) (40) were determined from CS-XY scans. Raw scans were corrected for NBD-PE and background contributions to determine protein signal average intensities in l_o phases (I_{lo}) and l_d phases (I_{ld}). K_p was found as I_{lo}/I_{ld}. Another useful parameter for analyzing changes in K_p is raftophilic excess, E_{raft} defined as the difference in signal intensities between l_o and l_d phases normalized by the sum of the signal intensities

$$E_{raft} = (I_{lo} - I_{ld})/(I_{lo} + I_{ld}) . \quad (3.1)$$

For a system perturbed, for example by the addition of ligands, the change in raftophilic excess, divided by two, equals the fraction of proteins $X_{migrate}$, which have migrated from l_d to l_o

$$X_{migrate} = (E_{raft(new)} - E_{raft})/2 . \quad (3.2)$$

3.2.3.4 A Control Study: Combined EPI/FFS Data for Cholera Toxin B

In order to verify the efficacy of the combined EPI/FFS strategy of determining lipid phase orientation in particular locations on a bilayer and performing quantitative CS-XY scans to find the partition coefficient and E_{raft} on a working system, a bilayer was constructed with the TYPE I mixture of lipids, NBD-PE, and 1 x 10^{-3} mol% GM1. Subsequently, CTxB-555 was added. EPI micrographs were taken and CS-XY scans were performed. FCS runs were then performed in the l_o and l_d phases as identified by

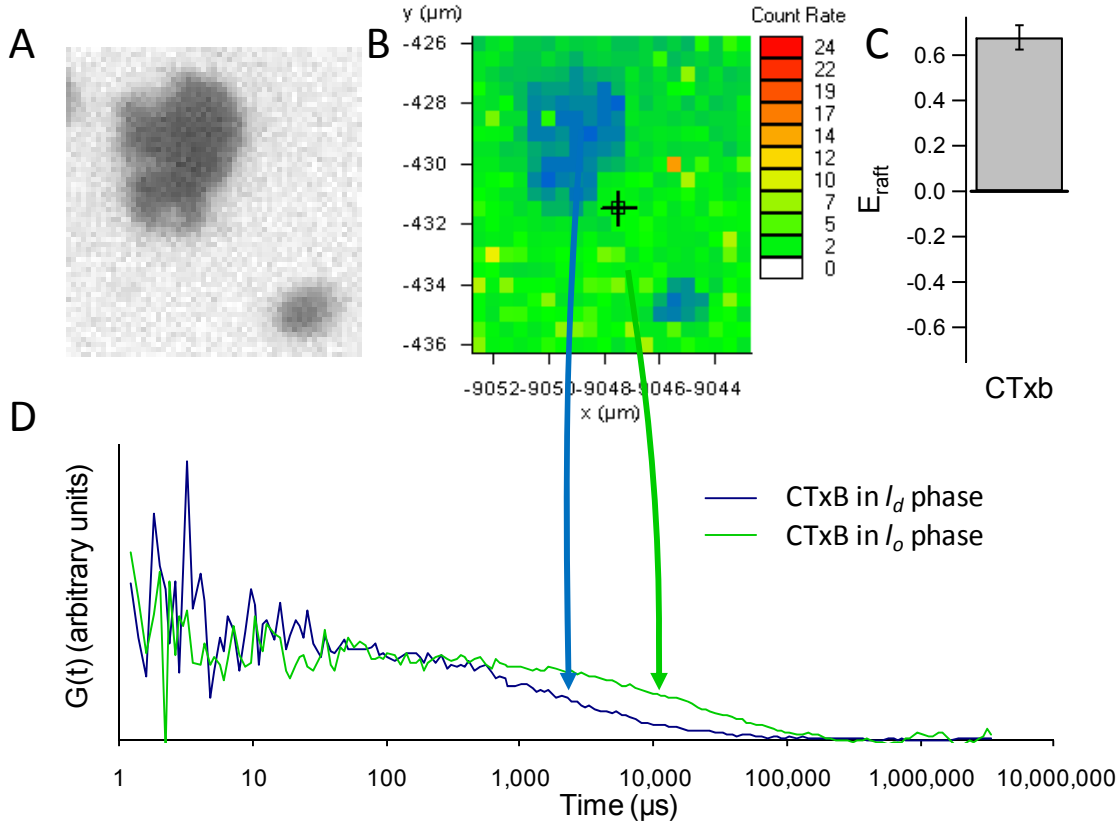

Figure 3.2.2 Combined EPI/FFS analysis of CTxB partitioning on phase-separated bilayer. (A) EPI micrograph of area of interest. (B) CS-XY scan of area of interest, 10 x 10 µm^2 at 0.5 µm intervals. (C) Determination of E_{raft} from data depicted in (B). (D) overlaid G(t) curves discovering different rates of diffusion of CTxB in l_o and l_d phases

the CS-XY scans. Representative results of these studies are shown in Fig. 3.2.2. (*A*) shows the EPI micrograph of the bilayer. (*B*) shows the CS-XY scan of the same area using the appropriate laser (543 HeNe, 7%) and filter settings for the Alexa-555 dye. From these data, it was first possible to determine E_{raft} from the intensities (*C*), with the minimal intensity from the NBD-PE first subtracted. Then, it was possible to move the stage to well-defined raft and non-raft areas and acquire FCS data determining characteristic diffusion times which indicate the relative diffusion coefficients (*D*). As expected, the CTxB diffusing in the non-raft l_d phase (*blue*) has a notably different characteristic diffusion time than the CTxB diffusing in the raft-like l_o phase (*green*).

While FCS is excellent at determining diffusion times, since it only analyzes fluctuations in intensity and not the full intensity profile, it is not as sensitive as PCH at determining brightness and number at low concentrations.

3.2.4 AFM on Air Stable and Water Stable Substrates

AFM images were obtained using a Digital Instruments BioScope, and analyzed using Nanoscope IV and Nanscope 6.12r1 software (Digital Instruments/Veeco Metrology Group, Plainview, NY). The samples were scanned using stiff (k = 0.32 or 0.58 N m^{-1}) non-conductive silicon nitride cantilevers (Veeco Instruments). Regions ranging from 0.5 x 0.5 μm^2 to 20 x 20 μm^2 were imaged at resolutions of 512 x 512 or 256 x 256 pixels using a scan rate of 0.1-1 Hz. Monolayers were analyzed in air within 48 hours of preparation using the tapping mode. Bilayers were analyzed in water (tapping mode) within 24 hours of preparation by mounting the cantilever onto a water-tight cantilever-mount. Manual tuning was necessary for the underwater images and for fine-tuning the air images. Both height and phase data were collected.

3.2.5 Calculating Thickness and Bending Elasticity of Lipid-Lipopolymer Mixtures

The thickness and bending modulus of monolayers containing lipopolymer/lipid mixtures have been investigated analytically. At concentrations of 3 mol% DSPE-PEG5000 or greater, the PEG polymers in the aqueous subphase, underneath the lipid monolayer, are in the brush regime. In other words, all the polymer headgroups interact and become stretched out as they overlap (78). Mean field theory calculations can be used to find the approximate length of the polymer brush, L_p, as follows:

$$L_p \approx n_p a_m^{5/3} (X_p / A_l)^{1/3} \tag{3.3}$$

where n_p is the number of monomers, a_m is the length of each monomer, X_p is the mole fraction of lipopolymers, and A_l is the area per lipid (47, 78). This assumes that water acts as a good solvent at the appropriate concentrations, and that monomers are equally dispersed throughout the volume at a constant density (a mean field approximation). These assumptions may not be exact but are a good approximation. For DSPE-PEG5000, n_p = 114, a reasonable value for a_m = 0.39 nm (78), and X_p can be set, but an explicit equation is needed for A_l. This is because when the concentration of lipopolymers exceeds a critical value, the area per lipid will start to expand to account for the polymer crowding. A_l as a function of X_p can be found by minimizing the interfacial free energy with respect to A_l. This corresponds to finding the minimum for the equation

$$\left(\frac{1}{A_{l,o}} - \frac{1}{A_l}\right) + B_2\left(\frac{1}{A_{l,o}^2} - \frac{1}{A_l^2}\right) + B_3\left(\frac{1}{A_{l,o}^3} - \frac{1}{A_l^3}\right) - (2/3)a_m^{4/3} n_p \left(\frac{X_p}{A_l}\right)^{5/3} = 0 \tag{3.4}$$

using the virial coefficients B_2 = 2.51 nm^2 and B_3= 0.779 nm^4 and $A_{o,l}$= 0.65 nm^2 (78) (using mean field theory). Once A_l is found numerically, then it is possible to determine the height of the lipid monolayer and the polymer layer. The height of the lipid monolayer is found by assuming constant lipid volume, so $d_l = d_{l,o}\,(A_{l,o}/A_l)$ and $d_{l,o}$ is 1.5 nm. The height of the full monolayer is then $h = L_p + d_l$.

The bending modulus is comprised of the mean curvature modulus, K_c and the Gaussian curvature modulus K_{cG}, but we will be assuming a straight sided blister as described below, and therefore $K_{cG} = 0$ and K_c can be written as follows

$$K_c = \frac{k_B T}{2}\left(\frac{1}{A_l} + \frac{2B_2}{A_l^2} + \frac{3B_3}{A_l^3}\right) d_l^2 + (5/9) k_B T a_m^{14/3} n_p \left(\frac{X_p}{A_l}\right)^{7/3} \quad (3.5)$$

(78) (again utilizing mean field theory) where T is taken to be 293 K and k_B is the Boltzmann constant. The first term in Eqn 3.5 is due to the lipid contribution and the second term is due to the polymer contribution. Casual inspection shows the polymer contribution includes the square of L_p multiplied by a term for the area expansion (47). These values of h and K_c will be needed to describe the buckling of a monolayer.

3.2.6. The Buckling of Thin Films on Rigid Substrates

Föppl and von Kárman investigated the elasticity of thin plates in the last century, and derived two coupled nonlinear partial differential equations (the FvK equations) to describe the vertical displacement of a film, w(x,y) and an Airy potential, v(x,y) such that the tangential components of the stress are the four second derivatives of the Airy potential in the (x,y) plane. The FvK equations have few analytical solutions (98). Based on the shape of the patterns formed by DSPE-PEG5000, the best analytically available solution is for a straight-sided blister, or "Euler column" (98, 99) and the boundary conditions are that the height of the blisters go to zero on the edges and Gaussian curvature is zero. For an Euler column, the bending stiffness is defined by the film thickness and the Young's modulus (E) or the plane strain modulus (E^*) as follows (99):

$$K_c = \frac{Eh^3}{12(1-\nu^2)} = \frac{E^* h^3}{12} \quad (3.6)$$

where ν is the Poisson ratio of the film and h is the film thickness. The Young's modulus is the ratio of the stress over strain for small values of stress and strain where Hooke's

law holds. The Poisson ratio is the ratio of the amount a sample contracts perpendicular to the load and the amount it stretches axially with a load. The solution of the FvK equations for the Euler column relates the critical stress (σ_c), defined as the stress at the onset of buckling, with bending stiffness, width and height of the buckles (99) as follows

$$\sigma_c = \frac{\pi^2 K_c}{b^2 h}. \tag{3.7}$$

Normalized critical stress, is $(\sigma_c/E^*) = (\pi^2/12)(h/b)^2$ from Eqns 3.6 and 3.7. The actual stress, σ_o, is determined from the same parameters plus the height of the buckle, w_{max}, through a parameter, ξ, defined as the ratio of the height of the buckle to the thickness of the film, $\xi = (w_{max} / h)$

$$\sigma_o = \frac{\pi^2 K_c}{b^2 h}\left(\frac{3}{4}\xi^2 + 1\right). \tag{3.8}$$

Another important parameter is the nondimensional loading parameter, which is the ratio of the actual film stress, σ_o, to the critical stress, σ_c. This can be determined using only ξ (99)

$$\frac{\sigma_o}{\sigma_c} = \frac{3}{4}\xi^2 + 1. \tag{3.9}$$

Clearly h and K_c can be calculated as described above using Eqns 3.3-3.5 and the published values for n_p, a_m, $A_{l,o}$, $d_{l,o}$, B_2 and B_3. Then, once the parameters w_{max}, b and θ are determined experimentally, it is possible to develop a metric-based understanding of the effect of the change in X_p on buckling in a mixed lipopolymer/lipid monolayer.

3.2.7 Generating the Algorithm for PCH

An algorithm for extracting brightness and number information from the PCH data was generated assuming a Gaussian point spread function (66, 67) and 50 particles or fewer in the observation volume. The central thesis of PCH is that a histogram of photon counts found for a single particle of average brightness ε in V_o ($p^{(1)}(k; V_o,\varepsilon)$) is described by integrating the Poisson distribution of ε multiplied by the PSF and integrated over the entire volume as follows.

$$p^{(1)}(k;V_o,\varepsilon) = \frac{1}{V_o}\int Poisson(k, \varepsilon \cdot PSF(\vec{r}))d\vec{r} \tag{3.10}$$

Assuming the particles are independent, the probability distribution for N particles in the volume is the probability of seeing 1 particle N times

$$p^{(N)}(k; V_o, \varepsilon) = (p^{(1)} \otimes p^{(1)} \otimes p^{(1)} \ldots \otimes p^{(1)})(k; V_o, \varepsilon) \text{ } N \text{ times.} \tag{3.11}$$

For an average concentration, the number of actual particles inside the volume will fluctuate. This fluctuation must also be captured as a Poisson distribution around N_{avg}.

$$PCH(k;N_{avg},\varepsilon) = \sum_0^\infty p^{(N)}(k;V_o,\varepsilon)\cdot Poisson(N, N_{avg}, \frac{V_o}{V}) \tag{3.12}$$

where the average photon counts, $\langle k \rangle$, will be the product of N_{avg} and ε. If a Gaussian PSF is chosen, and a factor, $Q = V_o/V$ is determined, which sets a ratio of total volume to Gaussian volume, it has been shown

$$p_G^{(1)}(k,Q,\varepsilon) = \frac{1}{Q\pi^{1/2}k!}\int \gamma(k, \varepsilon e^{-2x^2})dx \tag{3.13}$$

where γ is the incomplete gamma function (67). This can be numerically integrated for each value of k so that $p^{(1)}(k;Q,\varepsilon)$ can be used to determine $PCH(k; N_{avg},\varepsilon)$. For two

species, the photon counting histogram is the convolution of the probabilities for each species determined separately.

$$PCH(k;N_1,\varepsilon_1,N_2,\varepsilon_2) = PCH(k;N_1,\varepsilon_1) \otimes PCH(k;N_2,\varepsilon_2) \quad (3.14)$$

The Gaussian model has been shown to have difficulties at low count rate regimes with species of high brightness (67). In our model, this is corrected for by convoluting with a background species of low brightness and high count rate. In addition, we fit the PCH curves for values of $k > 1$. Some experimentalists have noted difference brightness values determined by their PCH algorithm for proteins in solution and proteins located on a slab of finite thickness (100). We find that setting $Q = 1$ enables good fits comparing brightnesses in solution and on a bilayer. For fitting the data to the PCH curve, the normalized probability of getting k counts is $h(k)$ and the probability of not getting k counts is $1-h(k)$. Standard deviation σ, and χ^2 are defined as described below

$$\sigma = \sqrt{(h(k)(1-h(k))} \qquad \chi^2 = \frac{\sum_{k=k\min}^{k\max} \frac{(h(k)-PCH(k))^2}{h(k)(1-h(k))}}{k_{\max}-k_{\min}-d} \quad (3.15, 3.16)$$

where d is the number of fitting parameters and $h(k)$ is the experimentally determined probability of observing k photon counts. We fit this using a least squares method. The residuals are as follows:

$$r(k) = (h(k) - PCH(k))/\sigma . \quad (3.17)$$

The quality of the fit can be estimated from the χ^2 value and the residuals.

As a practical matter, another way to calculate error for PCH algorithms is to run multiple sets of data and find the best fit answers to the fitting curves for N_{avg} and ε for the different data sets. The standard deviation in $h(k)$ for each k will suffice for error bars

for *h(k)* and when graphing brightness and number, the standard deviation of the solutions to N_{avg} and ε can provide error bars.

3.2.7.1 Particle Number and Brightness Determinations by PCH and FCS

After the PCH algorithm has been constructed, it must be tested by determining its ability to detect differences in fluorophore number and brightness. FFS data for low concentrations of a standard fluorophore, R6G, were tested by PCH and by FCS analysis to show the capability of PCH to determine number under relevant conditions. The results are shown in Fig. 3.2.3. Low dye concentrations were chosen for two reasons. First, with fewer photons hitting the detector, there is no need to correct for detector dead time (101). More importantly, these low fluorophore concentrations will better mimic the conditions that will be studied with membrane proteins. The results showed that PCH did as well as FCS in determining number, both finding a slight excess at the lowest concentration and working reasonably well for slightly higher concentrations.

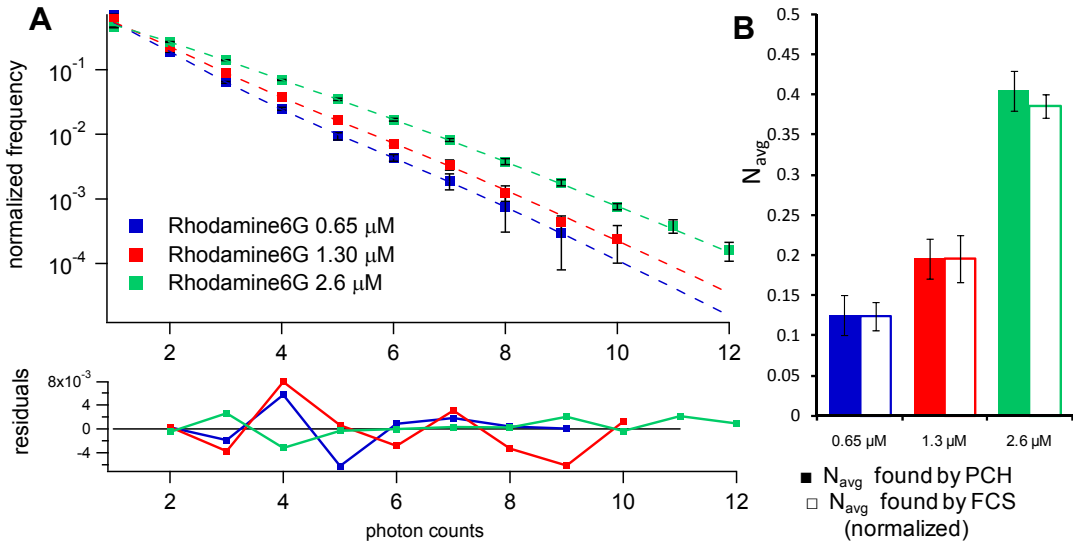

Figure 3.2.3 (A) PCH of R6G at three different concentrations, showing residual errors for the fit beneath (A). (B) Number extracted from PCH (filled bars) and from the autocorrelation curve description of the same data by FCS (open bars)

3.2.7.2 PCH Algorithm Calibration: Particles in Solution and on a Bilayer

In order to determine the oligomerization state of proteins on a bilayer, it is necessary to compare the brightness of fluorescent probes in solution, where they are monomers, and on a bilayer. However, different PCH algorithms can generate different brightness values in these two circumstances due to the different shape of a PSF for particles in solution, which is essentially a three-dimensional ellipsoid, and particles confined essentially to a plane (100). Therefore, it is necessary to test a PCH algorithm with a system that is known to be monomeric both on a bilayer and in solution to determine whether a correction factor is necessary. Maleimide-functionalized quantum dots (QDs) were deemed an appropriate choice for this control since they are monomeric in solution and when linked to thiol-functionalized lipids (DPTE) on a bilayer (94). A bilayer was constructed with SOPC with $2x10^{-3}$mol% DPTE. QDs were added in excess (60 min)

and unbound QDs were rinsed off before imaging. Fig. 3.2.4 shows the PCH algorithms and the best fits, with residuals for QDs in solution and on the bilayer.

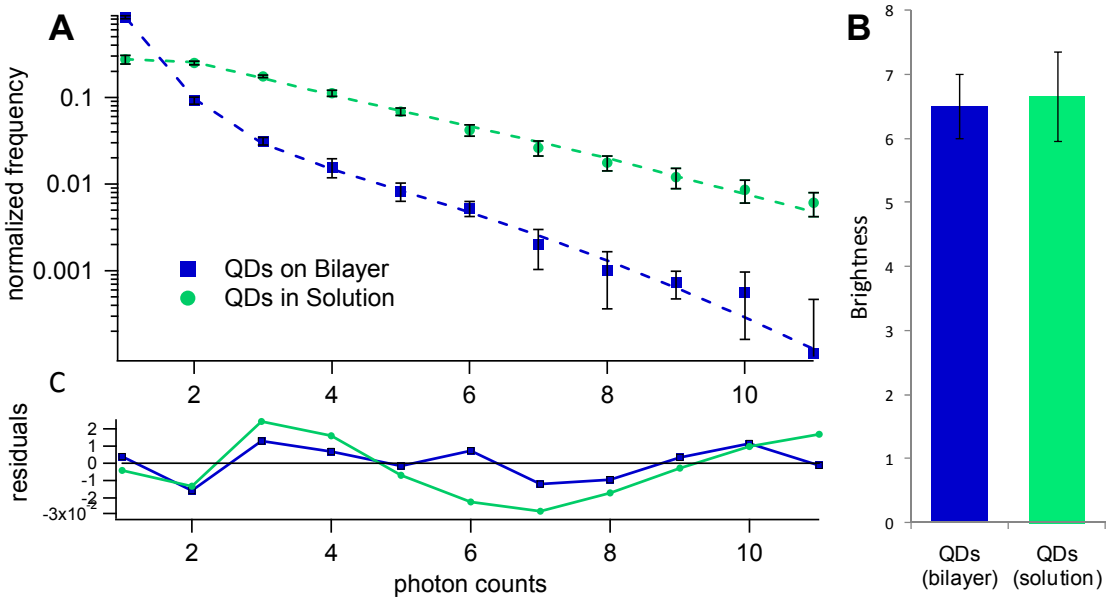

Figure 3.2.4 (A) PCH of QDs on a bilayer and QDs in solution with residuals. (B) Brightness extracted from PCH (with error bars) shows essentially equal brightness found by algorithm for fluorescent markers on a bilayer or in solution

CHAPTER 4 RESULTS AND DISCUSSION

4.1 Impact of Tether Concentration on Membrane Organization and Dynamics

A major difference between model lipid bilayers and a cell membrane is that model bilayers do not ordinarily contain membrane proteins. This is a critical difference due to the high density of membrane proteins in a plasma membrane (102). Membrane proteins not only have specific interactions with membrane lipids, such as those described in detail in Section 4.2, but also increase the lateral stress on a plasma membrane through connections to the cytoplasm, ECM, and steric crowding. One way to mimic an increase in lateral stress is to incorporate actin filaments to a lipid bilayer (46). Another method to systematically control changes in lateral stress is to incorporate lipopolymers into the lipid bilayer at increasing concentrations while maintaining the same surface tension on a Langmuir trough. As has been previously reported, increasing the mole fraction of lipopolymers in one leaflet of a bilayer leads to decreasing rates of diffusion in a process generally described as obstructed diffusion (61). Moreover, this effect is coupled across the bilayer so that a decreased rate of diffusion in one leaflet is mirrored by a decreased rate of diffusion on the other leaflet (103). Beyond changing the rate of diffusion, increasing the lipopolymer content in a lipid bilayer should induce other long-range effects involving membrane tension, membrane stress, and even membrane buckling. Section 4.1.1 describes the investigation of observed diffusion barriers identified in membranes constructed with high mole fraction (X_p) DODA-E_{85}. Ultimately, it is shown

that the diffusion barriers occur due to buckling of the LB monolayer caused by the lateral stress imparted by the lipopolymers where the lipophilicity of the polymer moiety is instrumental in the creation of the diffusion barriers. The diffusion barriers segregated the 30 mol% DODA-E_{85} into μm^2-sized compartments. Section 4.1.2 describes a systematic investigation of the buckling patterns of DSPE-PEG5000 (X_p = 0.03 – 0.40) by AFM and EPI to determine the effect of increasing lipopolymer concentration on film stress and response in model monolayers.

4.1.1 Buckling-induced Diffusion Barriers in Lipopolymer-Enriched Bilayers

We first conducted a set of EPI and FRAP experiments to explore the impact of applied lateral stress on the large-scale membrane organization and dynamics of a physisorbed polymer-tethered phospholipid bilayer. Fig. 4.1.1 illustrates representative EPI and FRAP micrographs of physisorbed polymer-tethered SOPC bilayers containing 5 (*A,D*), 15 (*B,E*), and 30 mol% (*C,F*) of DODA-E_{85}. While the LS monolayer exclusively contains the phospholipid SOPC and 1 mol% dye-labeled lipid NBD-PE, the LB monolayer is comprised of mixtures of NBD-PE, SOPC and DODA-E_{85}. At the low lipopolymer molar concentration of 5 mol%, the fluorescence micrograph shows a homogeneous bilayer (Fig. 4.1.1(*A*)). In this case, an isotropic fluorescence recovery can be observed (Fig.4.1.1 (*D*)), which resembles that of a one-component lipid bilayer in the fluid phase. In contrast, at 15 mol% DODA-E_{85}, the fluorescence micrograph suggests the existence of two distinct phases (Fig.4.1.1 (*B*)). Remarkably, the corresponding FRAP experiment shows that the darker phase acts as a lipid diffusion barrier, thus effectively compartmentalizing the bilayer system (Fig. 4.1.1(*E*)). At 30 mol% DODA-

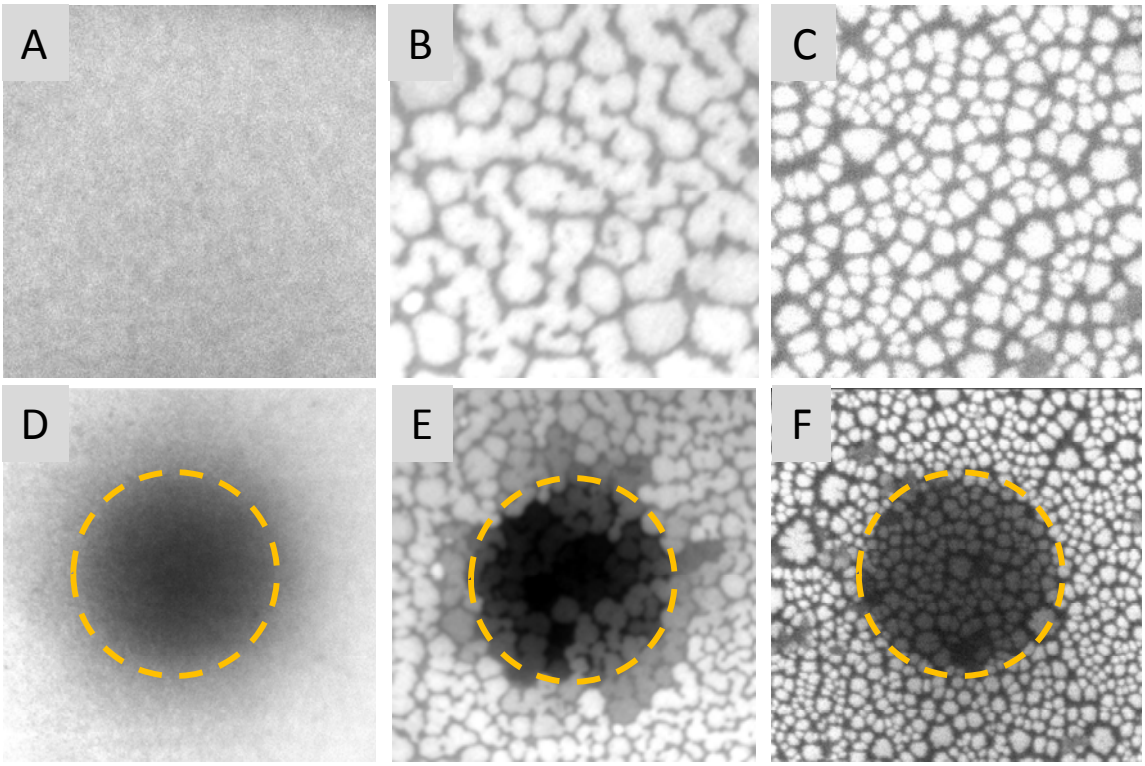

Figure 4.1.1 EPI micrographs (taken using 40x objective) of bilayers with 5 (*A,D*), 15 (B,E), and 30 (C,F) mol% DODA-E_{85} in the LB layer, and SOPC in the LS layer, illustrating qualitatively the impact of lipopolymer concentration on membrane organization. The size for the top row is 50 µm x 50 µm; the size for the bottom row which also show FRAP (2 min recovery after bleaching) is 100 µm x 100 µm. The dotted circle indicates the position and size of the bleaching spot

E_{85}, the dark phase becomes more pronounced and the bilayer compartmentalization becomes more complete (Figs. 4.1.1(*C,F*)). Comparable results were obtained when NBD-PE was replaced by TRITC-DHPE, thus excluding dye-specific artifacts as a possible explanation of the data in Fig 4.1.1. Representative micrographs showing the effect of continued bleaching of a small spot using TRITC-DHPE instead of NBD-PE are provided in Fig. 4.1.2. It is possible to watch fluid dyed-lipids moving from outside the bleaching area in toward the center, but they are clearly restricted by the same diffusion barriers seen using NBD-PE.

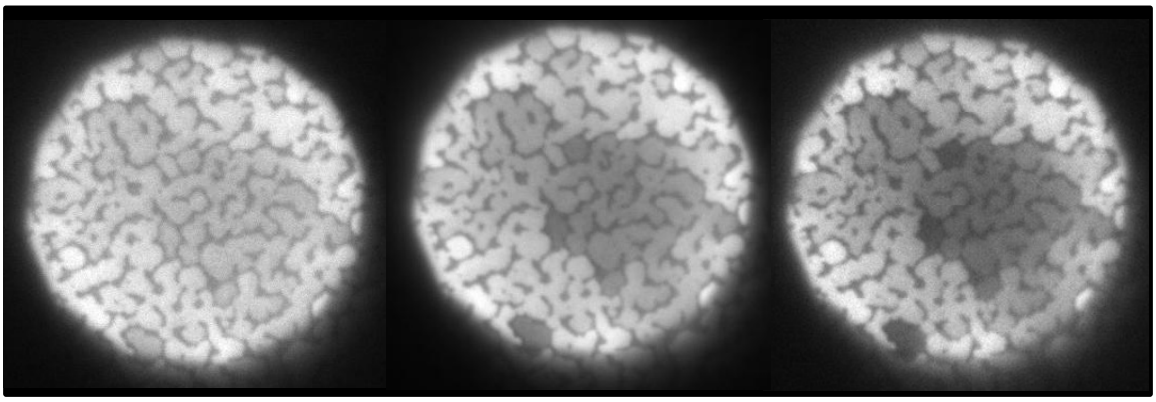

Figure 4.1.2 EPI micrographs of 15 mol% DODA-E_{85} in SOPC using TRITC-DHPE dye. Micrographs taken during continuous bleaching over time (t_{lag} = 30 s between each frame) show bleach-out is most complete for areas cut off from rest of bilayer by diffusion barriers. Box = 60 μm

4.1.1.1 Studies on Fluorescently Labeled DiC_{18}-P_{50} Monolayers

One possible explanation for the different phases in Figs. 4.1.1 and 4.1.2 is the formation of a large-scale phase separation into lipopolymer-poor and lipopolymer-rich phases in the bottom leaflet (LB monolayer). In fact, recently it was reported that polymeric systems are able to corral lipids in a monolayer, thereby causing its compartmentalization (104). In addition, lipopolymer-phospholipid phase separations have been reported on polymer-tethered lipid bilayer systems built using very slow LB transfer speeds (105). To explore whether such phase separations would explain the micrographs shown in Figs. 4.1.1 and 4.1.2, LB monolayers of SOPC with 15 mol% were constructed with 0.4, 0.6, and 0.8 mol% dyed lipids (TRITC-DHPE) or 0.4, 0.6, and 0.8 mol% dyed lipopolymers ($diC_{18}E_{50}$-TRITC). Fig. 4.1.3 (*A*) illustrates representative EPI micrographs of LB monolayers showing the TRITC-DHPE (top) and $diC_{18}E_{50}$-TRITC distributions (bottom) (dye-molecule concentration: 0.6 mol%). As expected due to the

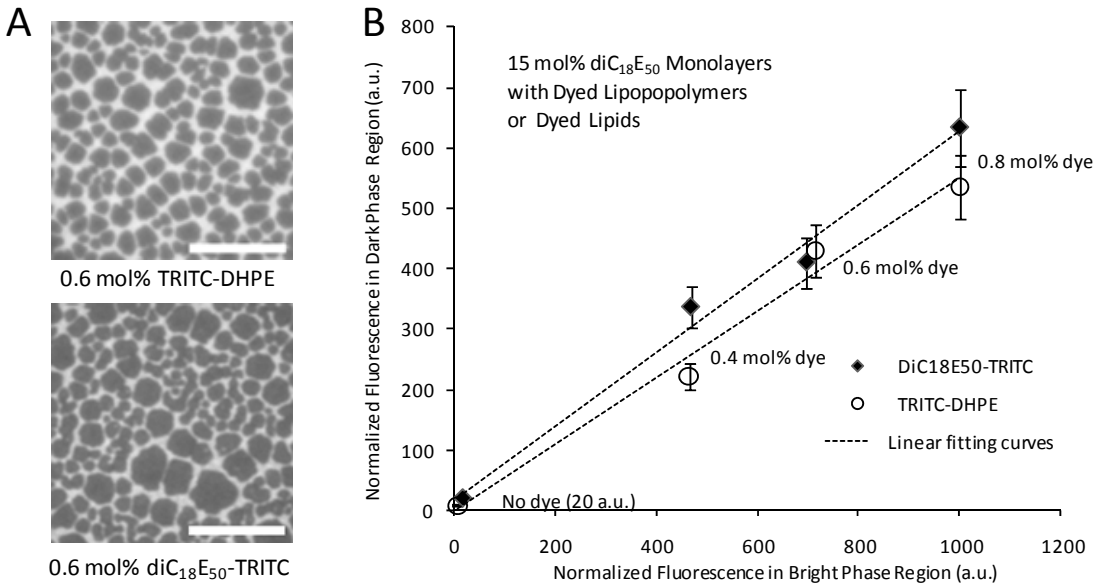

Figure 4.1.3 (A) EPI micrographs of LB monolayers with 15 mol% $diC_{18}E_{50}$, 84.6 mol% SOPC and 0.6 mol% either TRITC-DHPE (top) or $diC_{18}E_{50}$-TRITC (bottom). Scale bar is 10 μm. (B) Graph of relative fluorescence intensity in bright and dark regions for $diC_{18}E_{50}$-TRITC and TRITC-DHPE in LB monolayers with 15 mol% $diC_{18}E_{50}$. Data are taken from series of micrographs including those shown in (A), where fluorescence intensity is determined from relative gray values and normalized to arbitrary units (a.u.) where the bright region value for 0.8 mol% dye = 1000 a.u. Background values for the monolayer with no dye were also converted to a.u.

use of the same polymer moiety in both types of lipopolymers, the phase patterns in Fig. 4.1.3 are quite similar to those of the DODA-E_{85}-containing bilayer systems in Figs. 4.1.1 and 4.1.2, thus confirming the similarity of DODA-E_{85} and $diC_{18}E_{50}$. Interestingly, there is a phase inversion between the TRITC-DHPE-containing monolayer in Fig. 4.1.3(*A*) and the bilayers in Figs. 4.1.1. In contrast, no phase inversion is observed if one compares the phase patterns of dye-labeled lipids and dye-labeled lipopolymers in Fig. 4.1.3(*A*). Since there is no phase inversion, the lipids and lipopolymers must be roughly equally distributed across the monolayers. This important result indicates that the existence of both phases cannot simply be attributed to lipid-lipopolymer phase separations in the LB monolayer. To confirm this qualitative finding, a quantitative

analysis of the normalized fluorescence intensities of the dark and bright phases of comparable LB monolayers was conducted in the presence of 0.4, 0.6, and 0.8 mol% TRITC-DHPE and di$C_{18}E_{50}$-TRITC, respectively (Fig. 4.1.3(*B*)). This quantitative analysis showed that the fluorescence intensity in the dark phase is more than 16-fold higher than the background intensity (without dyes), thus excluding partial dewetting of the monolayer as a possible interpretation for the dark phase. Another notable result of Fig. 4.1.3(*B*) represents the linear relationship between changes in normalized fluorescence intensities of dye lipids and dye lipopolymers in the bright and dark phases. The resulting slopes of the linear fitting curves in Fig. 4.1.3(*B*) suggest 1.6 and 1.8 fold enrichments of both TRITC-DHPE and di$C_{18}E_{50}$-TRITC in the bright phase. These almost identical enrichment values of both types of probe molecules confirm that dark and bright phases in Fig. 4.1.3(*A*) are not caused by phospholipid-lipopolymer demixing. Obviously, an alternative explanation must be sought to explain the existence of these two distinct phases.

4.1.1.2. AFM of DODA-E_{85} Enriched Monolayers and Bilayers

To further understand the surface morphologies of these interesting systems, AFM data were obtained on an LB monolayer containing 30 mol% DODA-E_{85} and an LB/LS bilayer with the same composition in the LB layer and SOPC in the LS layer. Fig. 4.1.4 illustrates representative height (*A*) and phase data (*B*) of the monolayer system, which are quite instructive. Fig. 4.1.4(*A*) demonstrates that the LB monolayer contains a series of connected ridges, such that the highest point on the monolayer extends about 2.5 nm from the base. The pattern similarity of ridge regions in Fig. 4.1.4(*A*) and bright phases

in Fig. 4.1.3(*A*) provides a plausible explanation for the existence of two phases in the mixed lipopolymer-lipid LB monolayer at elevated lipopolymer molar concentration observed by EPI. In other words, non-planar regions (ridges) contain more lipid and lipopolymer material than planar (base) regions. The corresponding AFM phase mode image (Fig. 4.1.4 (*B*)) does not show a significant contrast between base and ridge regions and provides further evidence that the monolayer does not undergo a partial dewetting from the glass substrate, thus confirming the corresponding findings from EPI on LB monolayers presented in Fig. 4.1.3.

These phase data also exclude partial lipopolymer crystallization as a possible reason for the formation of ridges in Fig. 4.1.4(*A*). Such crystallization phenomena have been reported on crystallizable polymeric films (106, 107). The lack of lipopolymer crystallization in Fig. 4.1.4(*A*) is supported by the observation that Langmuir monolayers of comparable poly(2-ethyl-2-oxazoline) lipopolymers maintain their fluidity at the LB transfer pressure of 30 mN m^{-1} (108). Instead, the ridge and base regions in Fig. 4.1.4(*A*) can be interpreted in terms of a mechanism of buckle-driven delamination. Here the buckling/delamination can be explained in terms of the competing nature of attractive physisorption of lipopolymers on the solid substrate and repulsive forces between stretched polymer chains of neighboring lipopolymers. This competitive interaction behavior implies that lipopolymers in delaminated regions adopt entropically more favorable (less stretched) polymer conformations. Such a buckle-driven delamination

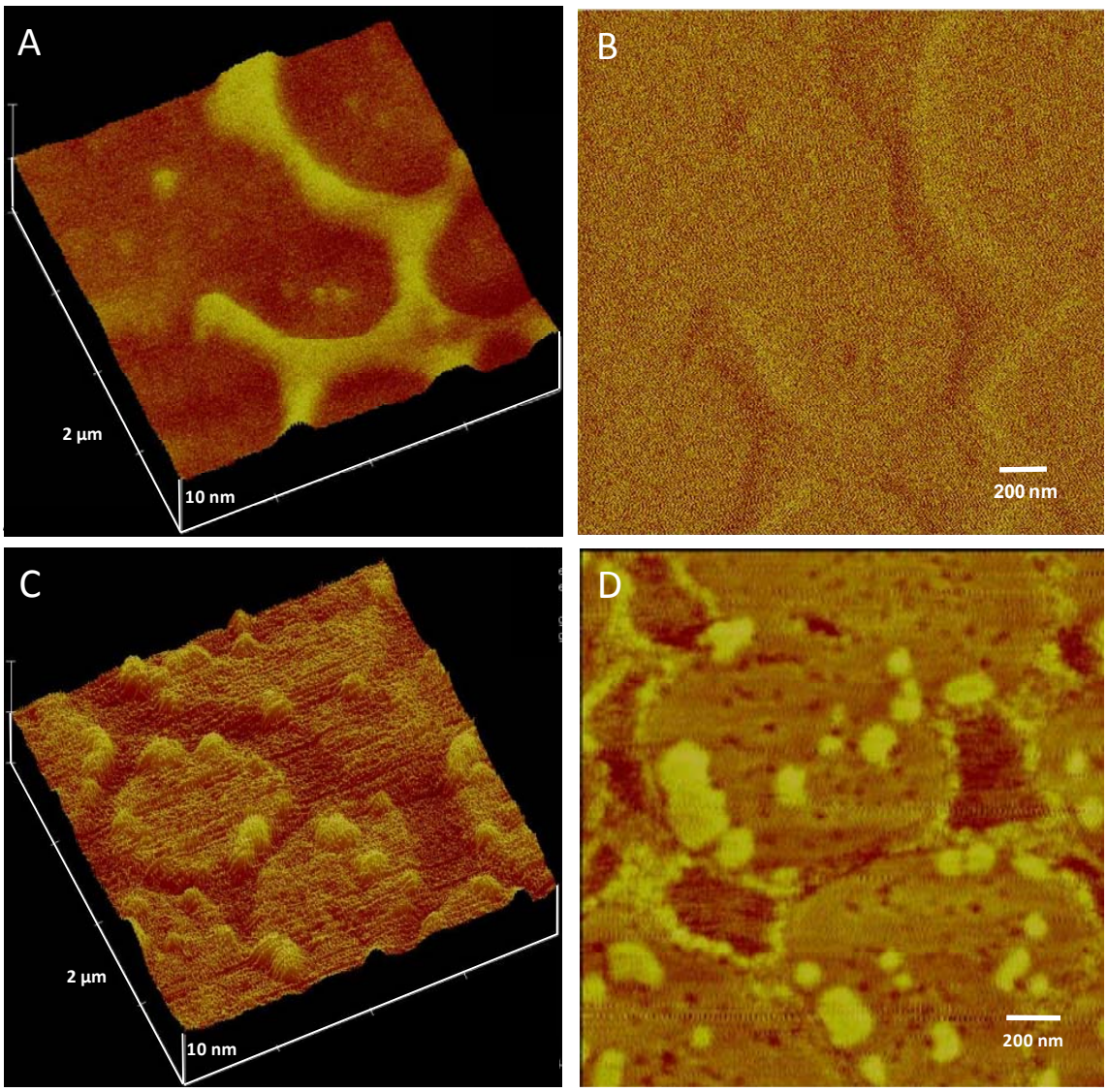

Figure 4.1.4 Height (A,C) and phase (B,D) images of LB monolayer (captured in air) (A,B) and LB/LS bilayer (captured under water) (C,D) with 30 mol% DODA-E_{85} in LB monolayer. Scales as shown.

process was also recently observed on polymer brushes, which were grown from an initiator and subsequently cross-linked to fabricate a film containing internal lateral compression stresses (109). There, the partial delamination of the polymeric film was achieved by weakening thiol-gold polymer-substrate linkages using an electrical pulse. If the adsorption strength of polymer chains to the underlying solid is strong enough,

polymers may also partially escape the lateral stress without desorption by stretching their chains.

Of even greater interest than the LB monolayer morphology is that of the bilayer constructed by subsequent LB and LS monolayer transfers. Figs. 4.1.4(*C,D*) illustrate corresponding height (*C*) and phase (*D*) data of such a bilayer system. Remarkably, a comparison of the LB data in Figs. 4.1.4(*A*) and the LB/LS data in Figs. 4.1.4(*C,D*) indicates that the ridge regions in the LB monolayer become valleys in the bilayer system with the average depth of the valleys being 2.0 ± 0.3 nm as found by inspection of a number of AFM micrographs of bilayers. Because such valley regions appear to act as lipid lateral diffusion barriers, we hypothesize that, unlike in base regions, no lipid bilayer can form over ridges of the LB monolayer. It might be expected that if the monolayer has ridges about 2 nm high that do not form bilayers, then after the upper leaflet, nominally 2.5 nm in height completes over the non-ridge areas of the bottom leaflet there would be only a small height difference between the fluid and non-fluid regions. Instead, the bilayer is 2.5 nm taller than the incomplete monolayer system. The reason for this height differential is not straightforward, however, since the monolayer and bilayer experience different hydration conditions and the height of the polymer-tethered monolayer in water will be swelled relative to the height of a dry monolayer (41).

Interestingly, the existence of butte-like morphologies near the rim of bilayer regions in Fig. 4.1.4(*C*) also suggests a dewetting-like process, which is often characterized by an

accumulation of material into an advancing/retracting rim (110). The corresponding phase image (Fig. 4.1.4(*D*)) shows that that these butte-like regions are characterized by distinct viscoelastic properties. Previously, it has been reported that buckled, delaminated areas of a thin polymeric film may become nucleation sites for dewetting (111).

4.1.1.3 Effect of Polymer Hydrophilicity on Lipid Bilayer Fluidity

To further explore the underlying molecular process of bilayer compartmentalization in Figs. 4.1.1-4.1.4, we next modified the degree of hydrophilicity in the polymer moiety of lipopolymers. A possible explanation for the formation of the diffusion barriers is that the moderately lipophilic polyethyloxazoline polymer chain may escape the lateral stress imposed by polymeric crowding by penetrating through the hydrophobic lipid region of the LB monolayer. Should that occur, the surfaces of delaminated ridge regions in such systems would become less hydrophobic, which could possibly affect the ability of an LS monolayer to spread over such regions. To test this, we conducted a set of EPI and AFM experiments on polymer-tethered monolayers and bilayers using a more hydrophilic di$C_{18}M_{50}$. The enhanced hydrophilicity of poly(2-methyl-2-oxazoline) lipopolymers is exemplified by their lacking the low-pressure transition in pressure-area isotherms conducted on Langmuir monolayers that has been associated with adsorption/desorption of amphiphilic polymers at the air-water interface (108, 112). Significantly, DODA-E_{85} and DSPE-PEG5000 display this low pressure transition in pressure-area isotherms for $X_p > 0.05$ (data not shown). Fig. 4.1.6 shows FRAP/EPI data of model SOPC- di$C_{18}M_{50}$ bilayers after LB and LS transfers with 5 (*A*), 15 (*B*), and 30 mol% (*C*) di$C_{18}M_{50}$ in the

bottom leaflet. Unlike corresponding DODA-E_{85}-containing polymer-tethered membranes (Figs. 4.1.1-4.1.2), no dark phases acting as lipid diffusion barriers are evident in any of the micrographs in Fig. 4.1.6, regardless of lipopolymer molar concentration.

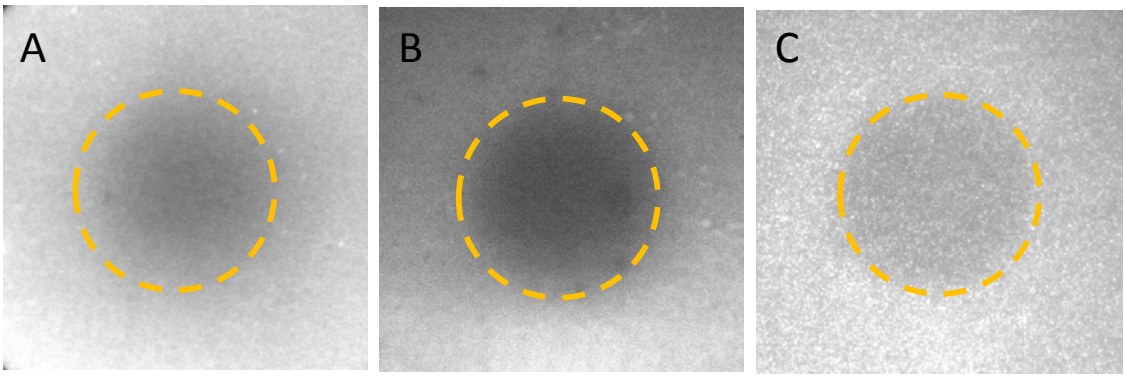

Figure 4.1.5 EPI micrographs (taken using 40x objective) showing FRAP of bilayers with 5 (A), 15 (B), and 30 (C) mol% di$C_{18}M_{50}$ in the LB layer, and SOPC in the LS layer. The size is 100 µm x 100 µm. The dotted circle indicates the position and size of the bleaching spot

To explore further the obvious differences between poly(2-ethyl-2-oxazoline) and poly(2-methyl-2-oxazoline) lipopolymer-containing polymer-tethered membranes in Figs. 4.1.1 and 4.1.5, the surface morphology of the latter systems was also investigated using AFM. Fig. 4.1.6 illustrates AFM height data of a polymer-tethered monolayer (*A*) and bilayer (*B*) containing 30 mol% di$C_{18}M_{50}$ in their LB monolayer. Instead of long ridges observed on the presence of DODA-E_{85}, the LB monolayer containing di$C_{18}M_{50}$ shows buckling into a series of small blisters (Fig. 4.1.6(*A*)). As indicated, the XY scale in Fig. 4.1.6 is magnified relative to the scale in Fig. 4.1.4 to better observe the more closely spaced blisters. The height of the blisters is 4-5 nm above the lowest point. The existence of different buckling patterns in DODA-E_{85}- and di$C_{18}M_{50}$ -containing membrane systems is not surprising, as theoretical models of compressed thin films

elastically attached to rigid substrates predict a variety of buckling patterns found in much thicker systems such as sputter deposited metal coatings (113-115). These patterns include circular blisters, straight-sided blisters, and single and mesh-like undulating stripes. In all of these cases, their occurrence depends on multiple parameters, such as the applied lateral stress, the film elasticity, the film thickness, and the strength of adhesion between film and substrate. Of particular interest here is that unlike the case of the DODA-E_{85} system in Fig. 4.1.4, the surface morphology of the di$C_{18}M_{50}$-based bilayer system Fig. 4.1.6(*B*) complements that of the corresponding monolayer Fig.

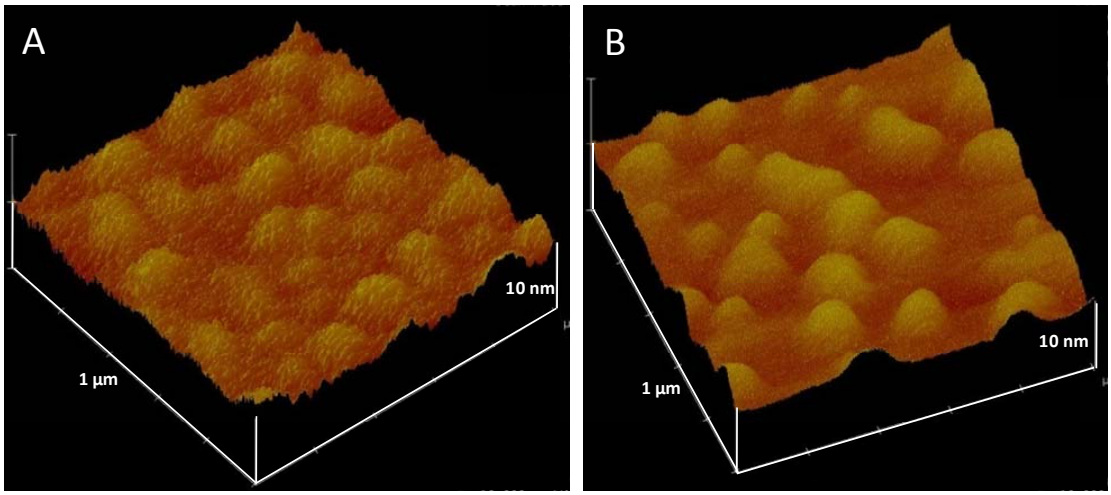

Figure 4.1.6 Height AFM images of (A) LB monolayer (captured in air) and (B) LB/LS bilayer (captured under water) with 30 mol% di$C_{18}M_{50}$ in LB monolayer

4.1.6(*A*). This important finding indicates that the entire bilayer can be completed on top of a di$C_{18}M_{50}$-containing LB monolayer, regardless of the existence of blisters, thus explaining the good fluorescence recovery on di$C_{18}M_{50}$ containing membranes shown in Fig. 4.1.5. The different EPI, FRAP, and AFM results obtained from DODA-E_{85}- and di$C_{18}M_{50}$-based LB monolayers and LB/LS bilayers in Figs. 4.1.1-4.1.6 suggest different stress relaxation processes of lipopolymers associated with their distinct polymer hydrophilicity or lipophobicity.

Fig. 4.1.7 provides a proposed schematic of these distinct stress relaxation processes. In the case of the polyethyloxazoline-containing lipopolymers DODA-E_{85} and di$C_{18}E_{50}$, the amphiphilic nature of the ethyloxazoline moiety of the lipopolymers enables a stress relaxation process in which polymers detach from the solid substrate and partially penetrate into the hydrophobic lipid regions of the delaminated monolayer, thus making the surface of these regions more hydrophilic (Fig. 4.1.7(*A*)). As a result of such a polymer relaxation process, a lipid bilayer can only be formed outside of delaminated membrane regions (Fig. 4.1.4(*C*)). In the case of di$C_{18}M_{50}$, the higher hydrophilicity of the methyloxazoline polymer moiety prevents the penetration of polymer chains into the hydrophobic part of the monolayer in response to applied lateral stress (Fig. 4.1.6(*B*)). Because the surfaces of buckled regions retain their hydrophobicity, a bilayer can be formed on top of buckled and unbuckled regions (Fig. 4.1.6(*D*)). The above model highlights the importance of a subtle amphiphilic balance between lipid and polymer moieties of lipopolymers in the structure and dynamics of polymer-tethered lipid bilayer systems, as considered in this study. Interestingly, Szleifer and coworkers previously reported that the bilayer stability in lipopolymer-containing vesicles also depends on a subtle balance between the polymer chains and lipid tails and that stable lamellar bilayer structures can only be formed at relatively low lipopolymer concentrations of less than 10 mol% (48). These findings support the notion that planar polymer-tethered phospholipid bilayers at elevated lipopolymer concentrations, as studied in the current work, trigger the frustration of the entire membrane system, which is only counterbalanced by

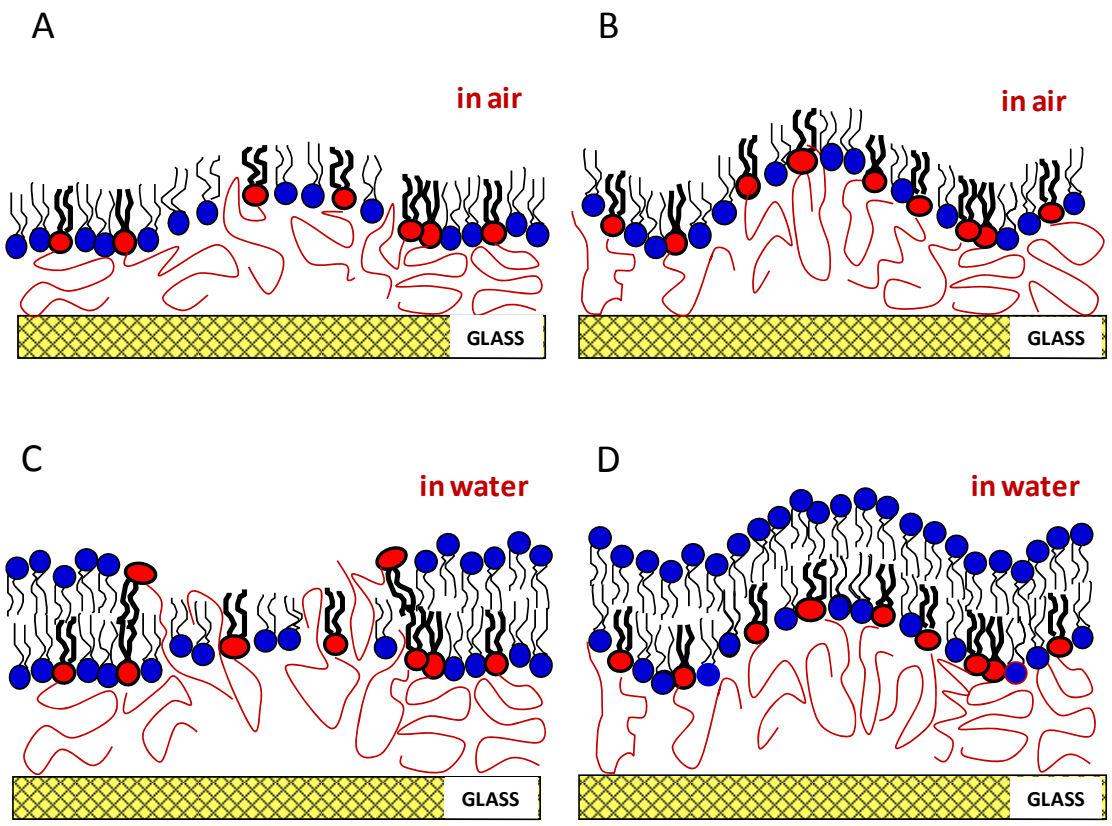

Figure 4.1.7 Proposed schematic of stress relaxation processes in LB monolayers, as derived from EPI, FRAP and AFM data, suggest the poly(2-ethyl-2-oxazoline) (E_{85}) moieties are more able to incorporate into the lipid monolayer than the poly(2-methyl-2-oxazoline) (M_{50}), disrupting the formation of a bilayer over the ridges for the DODA-E_{85} bilayer, but not the di$C_{18}M_{50}$ bilayer. As described in the text, the extent of void formation under buckled regions partially depends on the strength of polymer adsorption to the glass substrate. (A) DODA-E_{85} LB monolayer; (B) di$C_{18}M_{50}$ LB monolayer; (C) LB/LS bilayer of DODA-E_{85} and (D) LB/LS bilayer of di$C_{18}M_{50}$

physisorption of polymer chains to the solid substrate. The prevention of the bilayer formation on top of delaminated membrane regions observed in the case of the DODA-E_{85} system is intriguing because it can be seen as a process of buckling-induced dewetting of the LS monolayer. This dewetting effect is potentially interesting as it may be possible to correlate the relative amount of stress that a monolayer is experiencing by inspection of the pattern of buckles transferred on an LB monolayer.

4.1.2. Results from DSPE-PEG5000 Monolayers

Materials that buckle do so predictably in response to several controllable factors including film thickness, film stiffness, substrate stiffness, substrate adhesion forces, and compressive forces. By varying a few of these parameters in a controlled manner it should be possible to construct a metric relating buckling parameters to monolayer stiffness and thickness. The lipopolymer DSPE-PEG5000 was chosen for these studies because it exhibits diffusion barrier-buckles for $0.03< X_p <0.40$. Moreover, it is a well-characterized lipopolymer (47, 78, 116-118). In addition, the commercial availability of DSPE-PEG with different length of polymers (from molecular weight 500 to molecular weight 5000) makes this a promising lipopolymer on which to base a film buckling metric with which to study monolayers containing a variety of lipid mixtures.

4.1.2.1 Buckling Characteristics of DSPE-PEG5000 Monolayers

Thin films constructed from DSPE-PEG5000/SOPC mixtures using the LB technique and completed to a bilayer with the LS technique contain intricate buckled structures. Fig. 4.1.8 shows an EPI micrograph immediately after a circular section (indicated by a yellow dashed circle) was bleached for 30 s (*left*), and the FRAP pattern found 3 minutes later (*right*) for a bilayer constructed using 10 mol% DSPE-PEG5000 on the LB layer, and SOPC with the fluorescent lipid probe TRITC-DHPE in the LS layer. Noting the patterns in Fig. 4.1.8(*right*), it is clear that the structures act as diffusion barriers. The concentration of DSPE-PEG5000 (X_p), influences the buckling structures dramatically. Fig. 4.1.9 shows bilayers containing 3 mol%-40 mol% DSPE-PEG5000 that have been bleached and permitted to recover. At 3 mol%, the structures look like round blisters; by

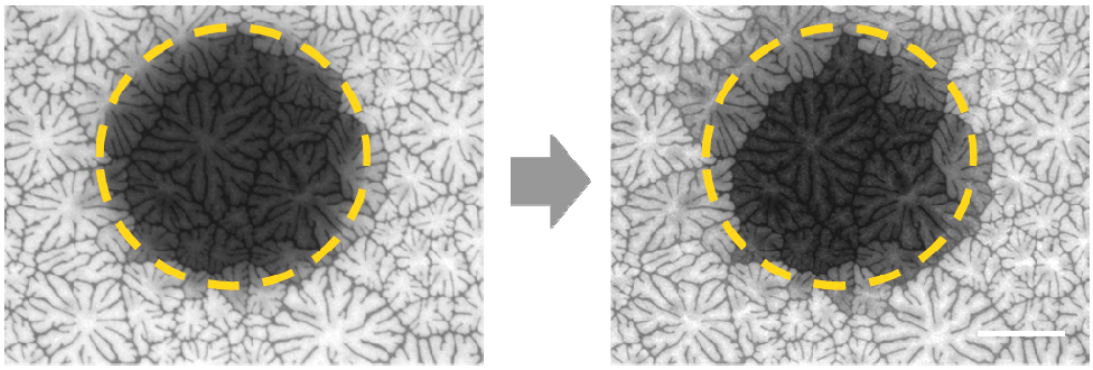

Figure 4.1.8 Bleach and recovery of a fluid lipid bilayer (10 mol% DSPE-PEG5000 in LB monolayer) is constricted by visible diffusion barriers. Immediately post bleach (left) and after 3 min recovery (right), yellow dotted circles show the bleaching area. Scale bar = 25 μm.

5 mol% they have elongated to snakes. At 10 and 20 mol% DSPE-PEG5000 buckling structures are more elaborate and branched, but by 30 mol% the structures are already becoming more compact and circular. The last micrograph at 40 mol% shows smaller, more circular structures and a fuller network of diffusion barriers.

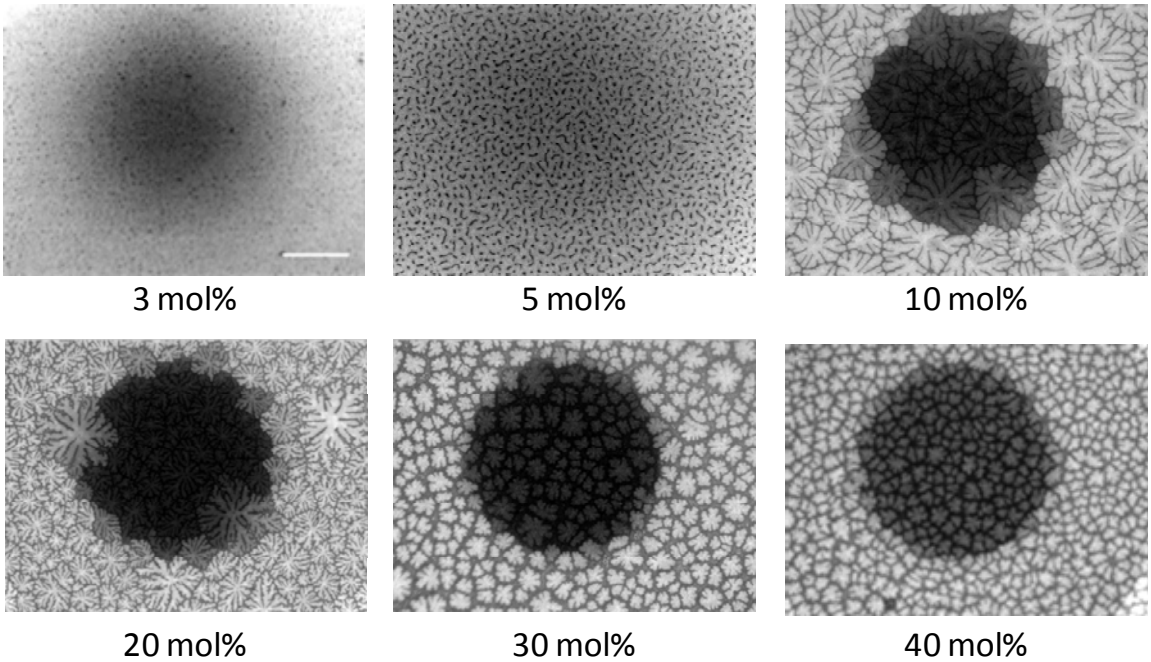

Figure 4.1.9 EPI micrographs of fluid bilayers with varying concentrations of DSPE-PEG5000 in LB layer, shown after bleach and ~3 min recovery. Scale bar = 25 μm

Interesting as these diffusion patterns are, however, the actual data on the buckled delaminations are best acquired from the monolayers before completion to bilayers. Bilayer completion adds a layer of lipids on top of the critical structures and hydration causes swelling of the polymers (119). Fig. 4.1.10 shows AFM data for 3, 5, 10, 20, 30 and 40 mol% DSPE-PEG5000 monolayers. The length scale is 20 x 20 μm^2 for Fig. 4.1.10(*B-F*) but is enlarged to show greater detail for the 3 mol% system to 5 x 5 μm^2 (Fig. 4.1.10(*A*)). From these and other AFM data, average values were found for *b*, the half-width of the buckle, w_{max} the average maximum height of the buckle, and θ, the angle at which the buckle delaminates. These values are tabulated in Table 4.1. For the *b* values, EPI micrographs of monolayers were also analyzed for the 10-40 mol%

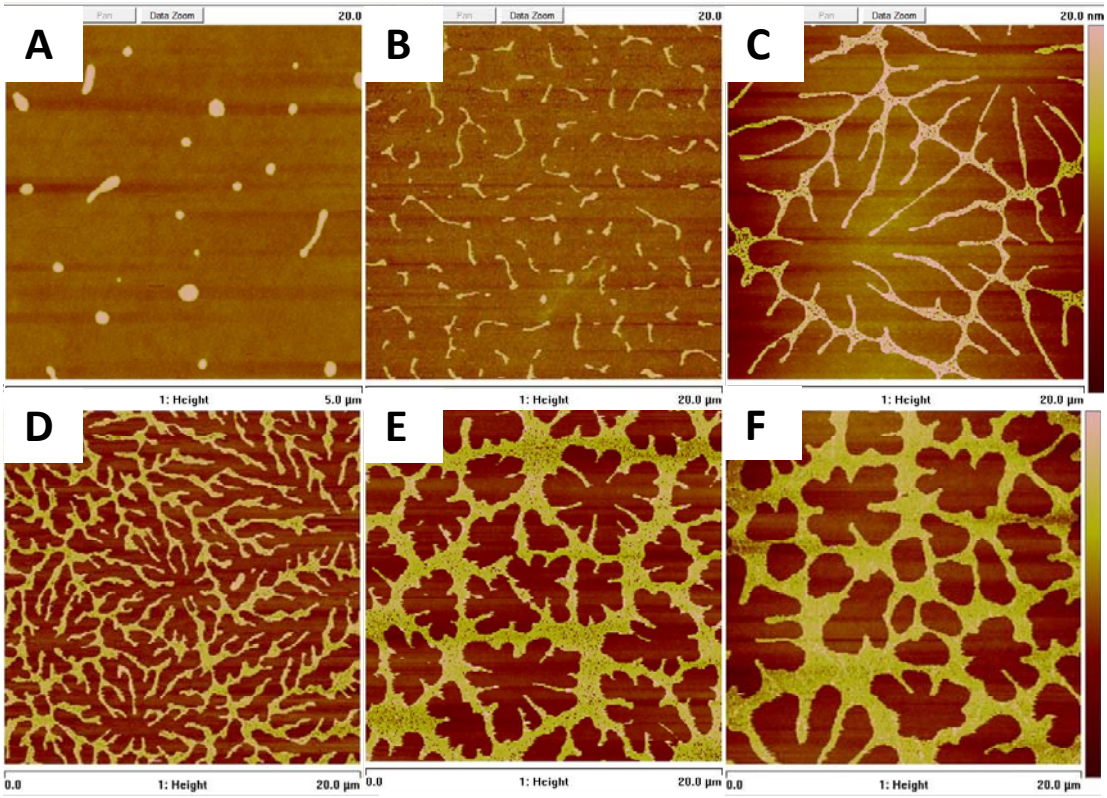

Figure 4.1.10 AFM data for 3 (A), 5 (B), 10 (C), 20 (D), 30 (E) and 40 (F) mol% DSPE-PEG in SOPC monolayer. Scales as indicated, (A) is 5 x 5 µm, (B-F) 20 x 20 µm. Height scale is the same for all monolayers (20 nm)

systems because they contain more information and show sufficient precision. Also included in Table 1 are bearing area (*BA*), that is, the fraction of monolayer which is buckled; and for the 10-40 mol% systems, average number of corrals in a 20 x 20 μm^2 box (N_{cor}), and the fractal dimension of the corrals, D_{corral}.

Table 4.1 Physical data obtained from AFM and EPI micrographs of DSPE-PEG5000 monolayers (error for w_{max} ± 0.5 nm). Fractal coefficient is for enclosed compartments only (10 mol% DSPE-PEG5000 and up)

X_p	b	w_{max}	θ (°)	BA	N_{Corr}	D_{corral}
0.03	203 ± 59	8.95	16 ± 4	3.3 ± 0.2	---	---
0.05	230 ± 75	8.2	12 ± 3	5.9 ± 0.3	---	---
0.1	350 ± 104	9.4	21 ± 8	14.0 ± 0.7	1.75 ± 0.35	1.94 ± .01
0.2	423 ± 167	8.8	19 ± 5	29.8 ± 0.5	4.6 ± 2.6	1.90 ± .01
0.3	907 ± 384	7.9	17 ± 8	38 ± 2	10.3 ± 1.5	1.86 ± .01
0.4	1149 ± 390	7.0	12 ± 6	39 ± 2	57.1 ± 4.0	1.81 ± .03

From inspection of the micrographs, there are clear correlations between X_p and *BA*, and X_p and N_{Corr} which are graphed in Fig. 4.1.11(*A,B*). From 3-20 mol% DSPE-PEG5000, there is a direct correlation between X_p and *BA*, the best fit is a straight line with an R^2 value > 0.99 and the error bars are smaller than the size of the markers. Also, at these concentrations the principal shapes of the buckles are circular blisters (for 3 mol%) or straight lines with increasing numbers of junctions. By 30 and 40 mol% DSPE-PEG5000, *BA* has significantly leveled off and the shape of the lines has switched

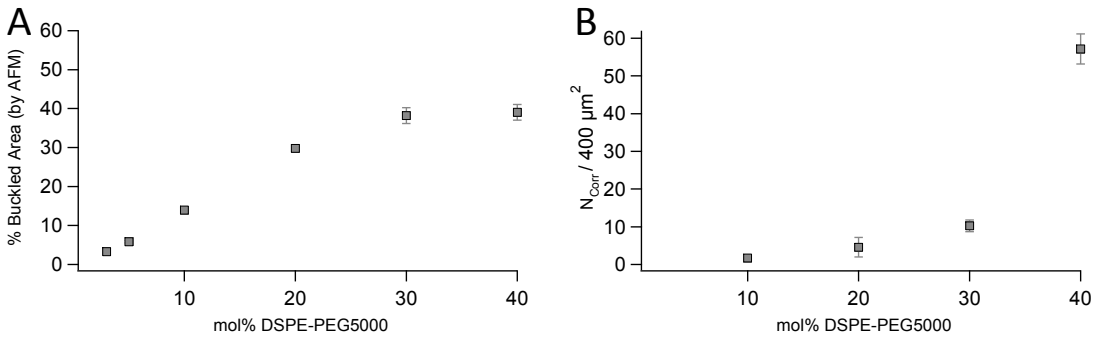

Figure 4.1.11 (A) Graph of % buckling (BA) vs. mol% DSPE-PEG5000 showing that increases in the mol% DSPE-PEG5000 increase BA linearly until 40 mol%. (B) Graph of number of corrals in 400 μm^2 box vs mol% DSPE-PEG5000 showing number of corrals increases linearly between 10-30 mol%, with large additional increase (decrease in size of corrals) at 40 mol%

to more rounded areas. Fig. 4.1.11(*B*) graphs X_p vs N_{cor}. For 10-30 mol% DSPE-PEG5000, $N_{cor} \sim X_p^{1/2}$. with an $R^2 > 0.99$. This relationship falters for X_p = 40 mol%, as N_{cor} gets very large. Interestingly, while b increases monotonically for increasing X_p, w_{max}, reaches a plateau at 10 mol% and then gradually decreases. θ follows a similar progression, reaching its maximum value at 10 mol%. While these data are interesting and enable the prediction of buckling patterns at different molar concentrations of DSPE-PEG5000, without more information it is not possible to relate the data to changes in membrane stiffness and membrane stress. To identify such relationships, it is necessary to look at theoretical models of lipopolymer mixtures which give calculations for the values of film thickness, bending stiffness and plain-strain modulus. These values, together with the experimental information, can then be applied to buckling theory of thin films on rigid substrates to makes predictions about whether films will buckle, how the actual film stress relates to the critical buckling stress, and to compare these data with plasma membranes found in nature.

4.1.2.2 Bending Modulus, Film Stress and Loading Parameter in DSPE-PEG5000 Monolayers

The two key parameters to apply to the study of the buckling patterns are film thickness (*h)* and bending stiffness (K_c). Using these values along with the information from EPI/AFM, it is possible to calculate a number of other parameters as described in Section 3.2.6, including ξ, the normalized height of the buckles (w_{max}/h); the loading parameter which relates the actual stress to the minimum stress that would induce buckling (σ_o/σ_c); the plane-strain modulus, E^*; and the normalized critical stress (σ_c/E^*). These values are reported in Table 4.2. The errors are propagated from the errors reported in Table 4.1.

Table 4.2 Useful mechanical properties of DSPE-PEG5000/SOPC monolayers

X_p	h (nm)	K_c/k_BT	E^* (Pa)	ξ	σ_o/σ_c	σ_c/E^*
0.03	9.88	32	1.59E+06	0.91 ± 0.5	1.61 ± 0.09	0.00195
0.05	12.07	48	1.33E+06	0.68 ± 0.04	1.35 ± 0.08	0.00226
0.10	14.65	137	2.12E+06	0.604 ± 0.03	1.30 ± 0.07	0.00144
0.20	17.49	495	4.48E+06	0.50 ± 0.03	1.19 ± 0.07	0.00141
0.30	19.04	970	6.82E+06	0.41 ± 0.03	1.13 ± 0.07	0.00036
0.40	19.95	1436	8.77E+06	0.35 ± 0.02	1.09 ± 0.08	0.00025

These data show some interesting trends. First, as expected, the calculated values for h and K_c increase monotonically with increasing lipopolymer concentration. For h, the larger factor is L_p which scales as a bit less than $X_p^{1/3}$ (Eqn 3.3), since A_l also increases with increasing X_p. For K_c, the term describing the polymer contribution scales as h^2 and

$X_p^{7/3}$ so this term, which increases rapidly with increasing X_p , dominates the value of K_c (Eqn 3.5). K_c for *Dictyostelium discoideum* (wild type) is about 400 k_BT, or around the same as 20 mol% DSPE-PEG5000 (12) and K_c for red blood cells is around 50 k_BT, about the value of 5 mol% DSPE-PEG5000 (8), although all determinations of bending moduli on live cells must be treated very cautiously.

The question of whether a compressed film on a substrate will wrinkle or deformably buckle has been analytically addressed (76). The important factors in this determination are the plane-strain modulii of the substrate and film and the relative size of the delamination, which is simply *b/h*. The plane-strain modulus of the glass substrate can be approximated as 71 GPa from average published values of Young's modulus and Poisson ratio for glass and the E^* values for the films are included in Table 4.2. The ratio of E_s^*/E_f^* is the critical stiffness ratio, R_c (76). In the current system R_c varies from 4×10^4 to 8×10^3 and at the same time, *b/h* varies from 20 - 50 (approximately). The model presented by Mei et al. is based on empirical data that relates R_c and *b/h* so that as R_c gets larger, the tendency to buckle increases and as *b/h* increases, the tendency to buckle decreases. Applying the model to our data, the 3 mol% DSPE-PEG5000 system has the largest R_c and the smallest *b/h* which would both predict buckling at even very small compressive stresses.

Another identifiable trend relates to w_{max}. These data do not appear to show much of a trend, but once the buckle height is normalized by correcting for the changing thickness of the monolayer, ξ monotonically decreases significantly from 3 - 40 mol% DSPE-

PEG5000. The stiffer monolayers with higher K_c deform a smaller height than the softer monolayers with lower K_c. From Table 4.1, increasing X_p also increases BA so the buckles, although smaller, become more prevalent (which is to be expected as *b/h* is also increasing in this regime). The loading parameter is the ratio of normal stress to the critical stress at the onset of buckling, σ_o/σ_c, and it is related to ξ by Eqn 3.9. Fig. 4.1.12(*A*) shows a graph of loading parameter vs concentration of DSPE-PEG5000. This shows a decrease in loading parameter with increasing concentration. This is the expected result since the relative stiffness of the film and the substrate also decrease with increasing X_p. Inspection of the values for θ, the buckling angle found by AFM, show that it also describes the same trend as σ_o/σ_c for 10-40 mol% DSPE-PEG5000 (although due to the high error associated in getting these buckling angles as the wrinkles did not all look alike, it would be easy to overinterpret this result). Not only the loading parameter, but also the normalized critical buckling stress (σ_c/E^*) which does not depend on w_{max} or K_c (Eqns. 3.5 and 3.7) decreases with increasing tether concentration.

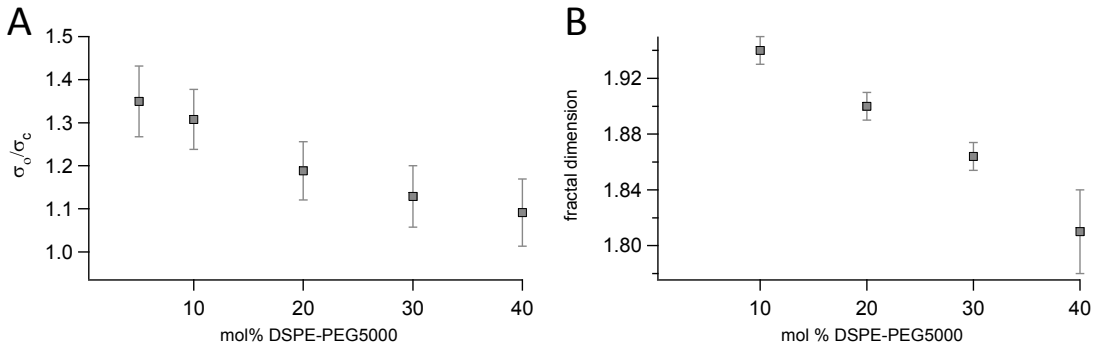

Figure 4.1.12 Graphs of loading parameter (σ_o/σ_c) (A) and fractal dimension (B) with increasing DSPE-PEG5000 concentration in LB monolayers

All of these trends describe a situation where the more stress on the bilayer, the closer it is to the critical stress so that smaller energetic fluctuations can induce buckles.

Another way to understand the impact of the trend in the loading parameter is by looking at the energy change for a given ratio of σ_o/σ_c (99): the ratio of extra energy beyond the energy required to buckle the system, or $\Delta G/G_o = (1- \sigma_c/\sigma_o)^2$ (99), varies from 14% at 3 mol% DSPE-PEG5000 to as low as 0.7 % for 40 mol% DSPE-PEG5000. This may have implications for cells: plasma membranes that have smaller loading parameters, that is, membranes that approximate the stiffness of nearby substrates, require less extra energy to induce a buckling response. Strictly by mechanical feedback, cells, if they contain sufficient surface stresses and adhesions to substrates, similarly sense substrate stiffness at a lower energy cost.

Another relationship to explore is one observed dramatically due to the intricate patterns seen on the films, particularly at 10 and 20 mol% DSPE-PEG5000. This is the relationship between X_p and the circularity of the buckling corrals. One way to quantify how circular the corrals are is by determining the fractal dimension for the corrals (97, 120), as described in Section 3.2.3.2. Briefly, the more labyrinthine the structure, the further its deviation from round, the higher the fractal dimension. Fig. 4.1.12(*B*) shows fractal dimension, *D*, as a function of X_p for 10-40 mol% DSPE-PEG5000, showing that as X_p increases, *D* decreases. Fractal analysis has been used to describe diffusion limited aggregation (97, 121), crystalline growth (120) and even the coalescence of gel-phase phospholipids on a Langmuir trough (122). However, to our knowledge, it has not been applied to the patterning of buckled thin films. One group studying wrinkling patterns on curved substrates, however, noted that the patterns changed from labyrinthine (more fractal) to triangular (less fractal) with decreasing loading parameter, σ_o/σ_c (123). That

trend is clearly matched in the current study, as shown by comparison of Fig. 4.1.12(*A*) and (*B*).

Finally, it is also possible to return to the AFM data and reconsider the trend whereby *BA* increased linearly with X_p until 30 mol%, then it tailed off some, and then at 40 mol% did not increase significantly. Fig. 4.1.13 shows 3D projections of 3 x 3 μm scans of 20 mol% and 40 mol% monolayers. The 40 mol% data show a set of secondary ridges within the primary ridges (similar ridges were also shown in Fig. 2.2.1, right). These ridges, approximately 30 nm in width and 0.95 nm in height, appear within the larger buckles that are approximately 1.1 μm in width and 7 nm in height. Thin films containing buckles on top of buckles have been reported and analyzed energetically to determine under which conditions these results might occur (124). There, the superimposed blisters formed when *b/h* was large and the elastic energy that went into increasing *b* was greater than the elastic energy of creating a secondary buckle within the first buckle. An example with $b/h \approx 100$ was identified. In the 40 mol% system, $b/h \approx 57$ and buckles are seen on buckles. In *Colin*, the first set of buckles were interpreted to be plastic, such that they could not re-form into smooth buckles upon addition of greater stress but instead formed buckles on buckles (124). The plasticity of the current system is unknown.but the existence of these secondary buckles suggests that to utilize DSPE-PEG5000 in monolayers as a metric for determining film stiffness, it is best to stay below 40 mol% DSPE-PEG5000 and *b/h* values less than 50.

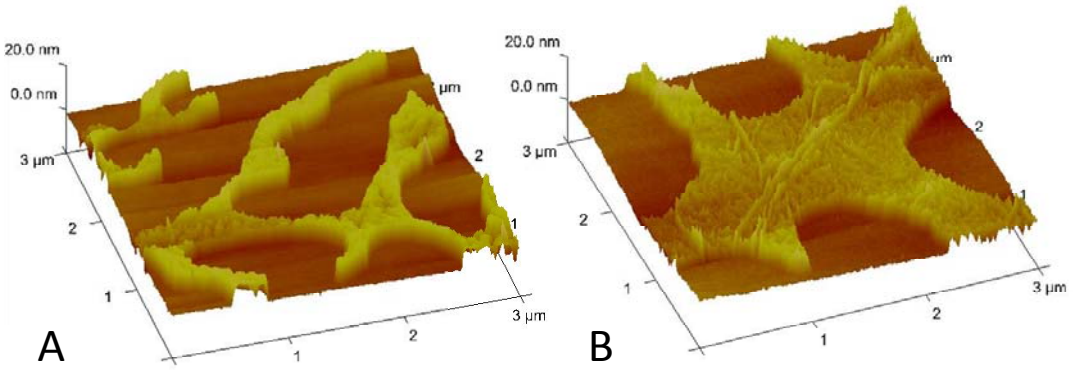

Figure 4.1.13 3-D projection of 3 x 3 µm^2 AFM scans of 20 mol % DSPE-PEG5000 (A) and 40 mol% DSPE-PEG5000 (B) showing a formation of secondary ridges along the top of the buckles at 40 mol% but not at 20 mol%

It has been argued that a monolayer of DSPE-PEG5000 compressed to a sufficiently high density can collapse through vesicular structures formed on top of the monolayer for monolayers with area/lipopolymer < 5 nm^2/molecule (118). There, 100% DSPE-PEG5000 lipids were transferred at π = 11, 13.6 and 18.9 mN m^{-1} and Brewster Angle Microscopy (BAM) showed some patches that looked like vesicles on top of the monolayer for PEG-DSPE5000 compressed to area/lipopolymer of 4 and 2.3 nm^2/molecule, but not for 5 nm^2/molecule. It is not inappropriate to compare data from pure DSPE-PEG5000 monolayers and mixtures of DSPE-PEG5000 and other lipids if the area per lipopolymer values are similar (125). The BAM data suggest that vesicular collapse may occur in the current system at high (> 20) mol% DSPE-PEG5000, where area per lipopolymer are less than 5 nm (as determined by pressure-area isotherms, data not shown). The AFM data do not show evidence of separate vesicles but it may be that some squeeze out or collapse contributes to the trends such as those seen in Fig. 4.1.11(*A*) at the higher mol% DSPE-PEG5000, where there is a falling off of *BA* at high X_p. The AFM of the transferred monolayers do not appear to present a second layer of vesicles on

top of the monolayer. The potential for this to occur suggests it might be preferable to utilize lower mol% DSPE-PEG5000 for analyzing buckling patterns to asses lipid monolayer stiffness in future studies.

A few other factors may complicate the analysis of the buckling patterns. First, the AFM of the monolayers are collected dry, whereas the transfer to the substrates took place at the air/water interface. Undoubtedly the monolayers dried out subsequently and that might significantly impact the total height and buckle width. It would be interesting to redo the experiments in 100% humidity conditions. Second, it was suggested in Section 4.1.1 (see Fig. 4.1.7) that the polymer moieties are capable of escaping into the lipid monolayers. However, there is no attempt to factor this effect into the current data set.

Even so, the buckling patterns show very regular trends. By combining mean field theory to determine film thickness and stiffness for different mixtures of lipids and lipopolymers with thin-film buckling theory, we have created a metric capable of analyzing mechanical properties of lipid monolayers based on the patterns generated by the manner in which they delaminate when transferred onto a glass substrate. The data fit well with existing theories on how buckling patterns should evolve for changing stiffness and film thickness, and the films are capable of producing bending stiffnesses in the same range as biological cells. Moreover, the data set showed there is a complex interplay between critical stiffness ratio, relative delamination size, and the energy cost of buckling. Since the response of different lipid compositions in the plasma membrane to

mechanical force is not well understood, analyzing the response of lipids in a model system could provide translational insights.

4.2 Integrin Sequestration and Oligomerization State Probed in Polymer-Tethered Model Membranes

4.2.1 Functional Reconstitution of Integrin Proteins into Tethered Bilayers

Lipid bilayers were constructed with 5 mol% di$C_{18}M_{50}$ incorporated into the LB layer. As described in Section 4.1.1.3, di$C_{18}M_{50}$ does not generate diffusion barriers even at high (30 mol%) tether concentrations and therefore was chosen as the best lipopolymer to use to introduce a polymeric cushion between the glass substrate and the lipid bilayer. The integrins $\alpha_v\beta_3$ and $\alpha_5\beta_1$ were successfully reconstituted into the bilayers using a modified Rigaud technique (95, 126) as described in Section 3.2.2. Membrane proteins' strong preference for the lipophilic bilayer cause insertion to occur. Integrins are transmembrane proteins with small cytosolic domains and large extracellular domains (127). In order to assure that only correctly oriented proteins were tracked, the integrins were labeled with fluorescently tagged antibodies subsequent to incorporation into the bilayer. The antibodies utilized are specific for the extracellular binding pocket of the integrins: any integrins incorporated upside down, that is with the cystolic domains above the top leaflet, would not bind to the antibodies and therefore would not be seen in the studies. This did permit the possibility of non-specific adsorption of fluorescent antibodies directly to the membrane, which was checked by adding antibodies to bilayers empty of proteins. Antibodies routinely washed off and left no trace on bilayers constructed of SOPC or SOPC with CHOL (TYPE II bilayers). For TYPE I bilayers, low

levels of antibody adsorption occurred, for $\alpha_5\beta_1$ but not $\alpha_v\beta_3$ antibodies, if left on the bilayer over 12 h; therefore, antibodies were rinsed off within 4 h (data not shown).

One complication with the Rigaud method is the detergent can incorporate into a bilayer. Therefore, following protein incorporation, biobeads which soak up detergent were added to the solution above the bilayers as described in Section 3.2.2. EPI micrographs of TYPE I bilayers verified detergent removal as shown in Figure 4.2.1. FCS of proteins also analyzed qualitatively for appropriate characteristic diffusion times to ensure detergent removal (FCS data not shown).

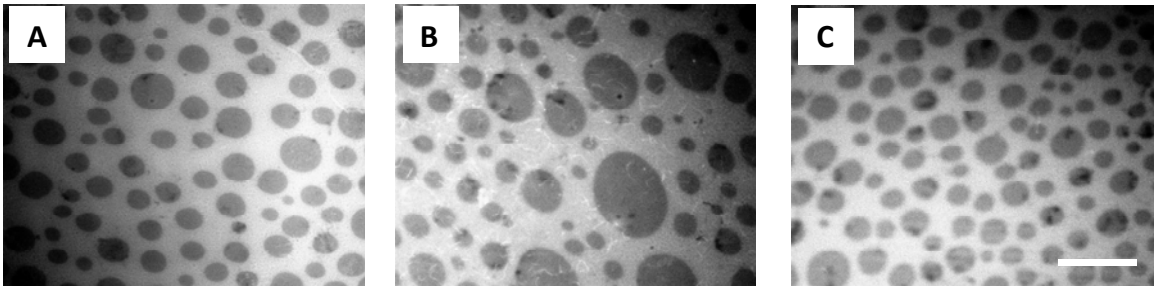

Figure 4.2.1 EPI micrographs of distribution of NBD-PE dyed lipids on TYPE I bilayer before addition of proteins with detergents (A), after addition of proteins and detergents (B) and after rinsing off detergents with biobeads (C). Scale bar is 50 μm

4.2.2 Determining Fluidity of $\alpha_v\beta_3$ and $\alpha_5\beta_1$ Incorporated into Tethered Bilayers

Proper incorporation of proteins was routinely verified by inspection using EPI micrographs and through data acquisition by FFS which gave characteristic diffusion times through the autocorrelation curve and through inspection of the intensity trace. A typical intensity trace for $\alpha_v\beta_3$ and $\alpha_5\beta_1$ (10 s) incorporated into polymer-tethered SOPC bilayers is shown as Fig. 4.2.2. These data, collected for 50 s run aggregates, formed the basis for histograms (*k(h)*) used in the PCH analysis. In addition, the diffusion profile was also quantified by analyzing the lateral diffusion of the proteins at single molecule

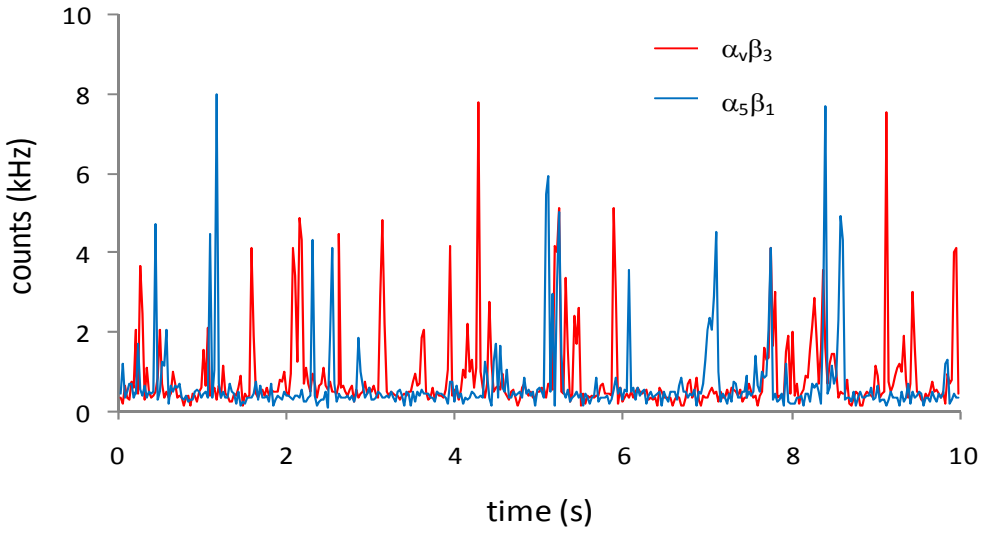

Figure 4.2.2 10 s intensity *vs* time trace for $\alpha_v\beta_3$ (blue) and $\alpha_5\beta_1$ (red) in TYPE II SOPC bilayers

(1 x 10^{-8} mol%) concentrations in TYPE II SOPC bilayers before and after ECM ligand binding using wide field single molecule fluorescence microscopy (128). The mean square displacement for t_{lag} = 38 ms were as follows: for $\alpha_v\beta_3$, $\langle r^2 \rangle$ = 0.060 ± 0.006 (-VN), 0.07 ± 0.007 (+VN), for $\alpha_5\beta_1$ $\langle r^2 \rangle$ = 0.11 ± 0.01(-FN), 0.14 ± 0.01 (+FN), (all values μm^2), immobile fractions < 10% by inspection of cumulative distribution functions). These data are in good agreement with data for $\alpha_{IIb}\beta_3$ integrins reconstituted onto other planar model membranes (129, 130). *Purrucker et al.* determined the thickness of a $DiC_{18}M_{60}$ polymer cushion physisorbed to a substrate to be 6.9 nm using neutron reflectometry for bilayers constructed with 6% $diC_{18}M_{60}$ (131). Scaling theory would suggest that the polymer cushion of $diC_{18}M_{50}$, used in the current experiments, would be a bit less than 5/6 as thick (from Eqn. 3.3), or about 5.4 nm. For integrins, the beta chain is slightly longer than the alpha chain in the cytosolic domain, approximately 50 aa that corresponds to about 8 nm (127). This protein length is adequately distanced

from the glass substrate by the polymer tether, and therefore the fluidity of the integrins in these systems is not surprising.

4.2.3 Determining Raft Sequestration Before and After Ligand Binding

As described above in Section 3.2.3.4, bilayers composed of DOPC:DPPC:CHOL in a 1:1:1 mixture with 5 mol% $DiC_{18}M_{50}$ in the LB layer and with registered l_o and l_d domains (TYPE I bilayers) were constructed with an addition to the LS mixture of 2 x 10^{-3} mol% GM1 and 0.5 mol% of the lipid raft marker NBD-PE. CTxB-555 was subsequently added and CS-XY scans were performed. As expected, the raftophilic CTxB colocalized with the NBD-PE: E_{raft} for CTxB = 0.68 ± 0.07. This corresponds to a K_p of 5.2 ±1.2, verifying the sensitivity of the bilayers to induce sequestration in the GM1/CTxB system. Next, TYPE I bilayers were constructed with 0.5 mol% NBD-PE added to the LS mixture and $\alpha_v\beta_3$ was incorporated as described above. After EPI micrographs were taken in both the protein (red) and NBD-PE (green) channels, CS-XY scans were performed, representatives of which are shown in Fig. 4.2.3(*left*), where the same area is scanned by the red (protein) channel and the green (NBD) channel. Comparing the CS-XY scans show that before addition of VN, $\alpha_v\beta_3$ displays a marked preference for the non-raft l_d phase. As illustrated in Fig. 4.2.3(*bottom row, left*), adding VN to the same substrate induced a dramatic change in raft preference. The $\alpha_v\beta_3$ proteins switched from l_d preference to l_o preference. The NBD-PE distribution is not perturbed

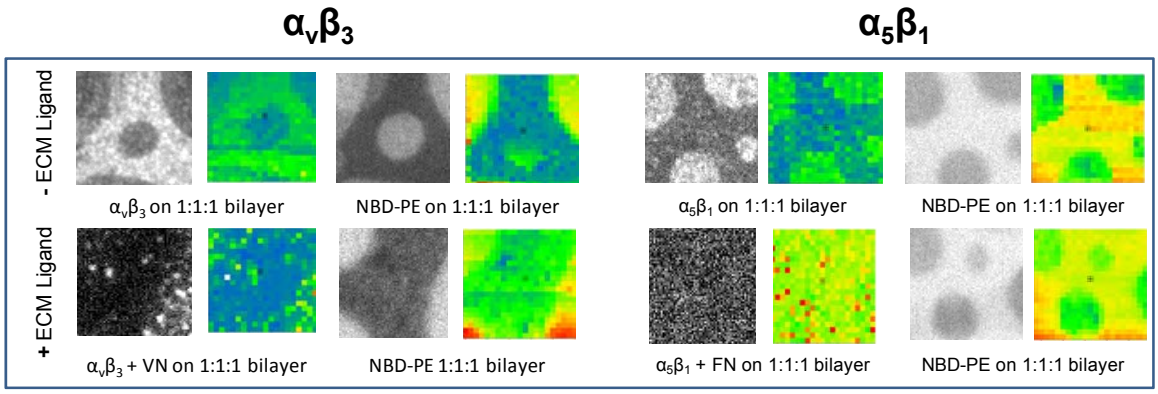

Figure 4.2.3 EPI micrographs (gray scale) and CS-XY scans (color) for $\alpha_v\beta_3$/NBD-PE - (left) and $\alpha_5\beta_1$/NBD-PE (right) incorporated into phase-separating TYPE I bilayers. NBD-PE is a raft marker; $\alpha_v\beta_3$ and $\alpha_5\beta_1$ are predominantly in the l_d phase before ligand binding (VN or FN) (top row); after ligand binding $\alpha_v\beta_3$ is predominantly in the l_o phase and $\alpha_v\beta_3$ and $\alpha_5\beta_1$ shows no preference for lo or ld (bottom row). Scale box = 10 μm

by the addition of VN. Motivated by the question of whether this large change in raftophilicity was specific to the $\alpha_v\beta_3$ integrins or was more generally applicable to other integrins, the experiment was carried out again using $\alpha_5\beta_1$ integrins and FN as the ECM ligand, and the results are shown in Fig. 4.2.3(*right*). Similar to the $\alpha_v\beta_3$ integrins, before addition of ligand the $\alpha_5\beta_1$ partitioned preferentially to the l_d phase. Subsequent to FN addition, however, the $\alpha_5\beta_1$ switched to displaying no strong preference for either the l_d or the l_o phase (Fig. 4.2.3(*bottom row, right*)). The results from the CS-XY scans are quantified and tabulated, along with the partitioning behavior of the GM1-CTxB system, in Fig. 4.2.4 which shows E_{raft} for $\alpha_v\beta_3$ and $\alpha_5\beta_1$ before and after ligand binding (VN and FN respectively), and E_{raft} for CTxB-555 linked to GM1. The fraction of receptors that translocated from the l_d domains to l_o domains can be quantified as $X_{migrate}$, as discussed above (Eqn 3.2). CS-XY scans showed $X_{migrate} = 53 \pm 6$ % for $\alpha_v\beta_3$ integrins, and $X_{migrate} = 27 \pm 3$% for $\alpha_5\beta_1$ integrins.

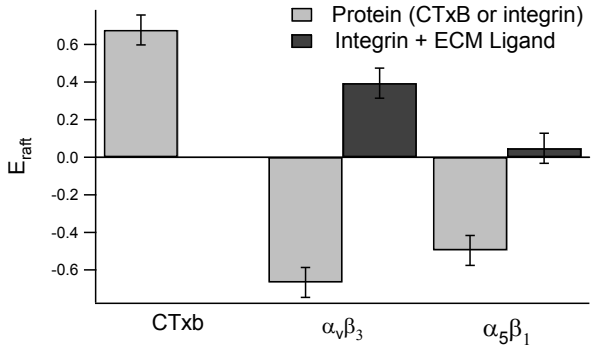

Figure 4.2.4 Normalized difference in intensity between l_o phase and l_d phase (E_{raft}) shown for GM1-CTxB and $\alpha_v\beta_3$ and $\alpha_5\beta_1$ before and after ligand addition. Negative values of E_{raft} correspond to K_p values less than 1

Cell studies have shown that inactive and unbound integrins, similar to the proteins reconstituted into the model bilayers in PBS buffer in the present experiment, are non-raft associated (132, 133). Integrin signaling, integrin involvement in cell adhesion and cell motility, and integrin involvement in angiogenesis, by contrast, are all raft-related activities as demonstrated by studies involving alteration of plasma membrane CHOL levels or association with other raft-associated proteins (31, 134-136). It appears that in the model system presented here, binding to ECM ligands alone suffices to increase a preference in $\alpha_v\beta_3$ and $\alpha_5\beta_1$ for the CHOL rich (l_o) phase, even in the absence of other protein co-factors, activating cations, or known cross-linking agents such as CTxB or crosslinking MAbs. It is notable that $\alpha_v\beta_3$ is more sensitive to raft sequestration than $\alpha_5\beta_1$. This finding is intriguing in light of the observation that $\alpha_v\beta_3$ regulates the adhesive and phagocytic activity of $\alpha_5\beta_1$ (137). Several research groups have investigated the partitioning of raft-associated proteins using giant unilamellar vesicles (GUVs) and giant plasma membrane vesicles (GPMVs). Results show that the relative preference for

ordered phases is higher for these proteins than for non-raft-associated proteins, and this preference increases on addition of crosslinking agents (52, 55, 57, 58). The current system differs from those by being planar and investigating oligomerization state along with sequestration in the absence of artificial crosslinking.

4.2.4 Determining the Degree of Oligomerization

Our previous data show that ligand addition causes substantial changes in E_{raft}, which opens the possibility that these changes are accompanied by similar substantial changes in integrin oligomerization state. Ligands are known to induce clustering in membrane proteins other than integrins (101, 138, 139). Moreover, clustering (through agents such as GM1 or a crosslinking antibody) is known to induce raftophilicity in integrins (39, 84, 140). In order to investigate whether ligand addition by itself induces a change in oligomerization state separate from any change that might be induced by change in lipid phase, a series of TYPE II bilayers, which do not phase separate, were constructed with 0, 5, and 30 mol% CHOL. Oligomerization state of $\alpha_v\beta_3$ and $\alpha_5\beta_1$ was probed by analyzing the PCH data acquired in these six systems before and after ligand binding. The PCH data are included in Fig. 4.2.4. The dotted lines describe the best fits found using the PCH algorithm, which gave information on brightness and dimerization, as described above in 3.2.7. The results of these best fits showing average brightness and degree of dimerization are shown in Fig. 4.2.5. The data show that the integrins were primarily monomers both before and after ligand binding, with the best fits for brightness

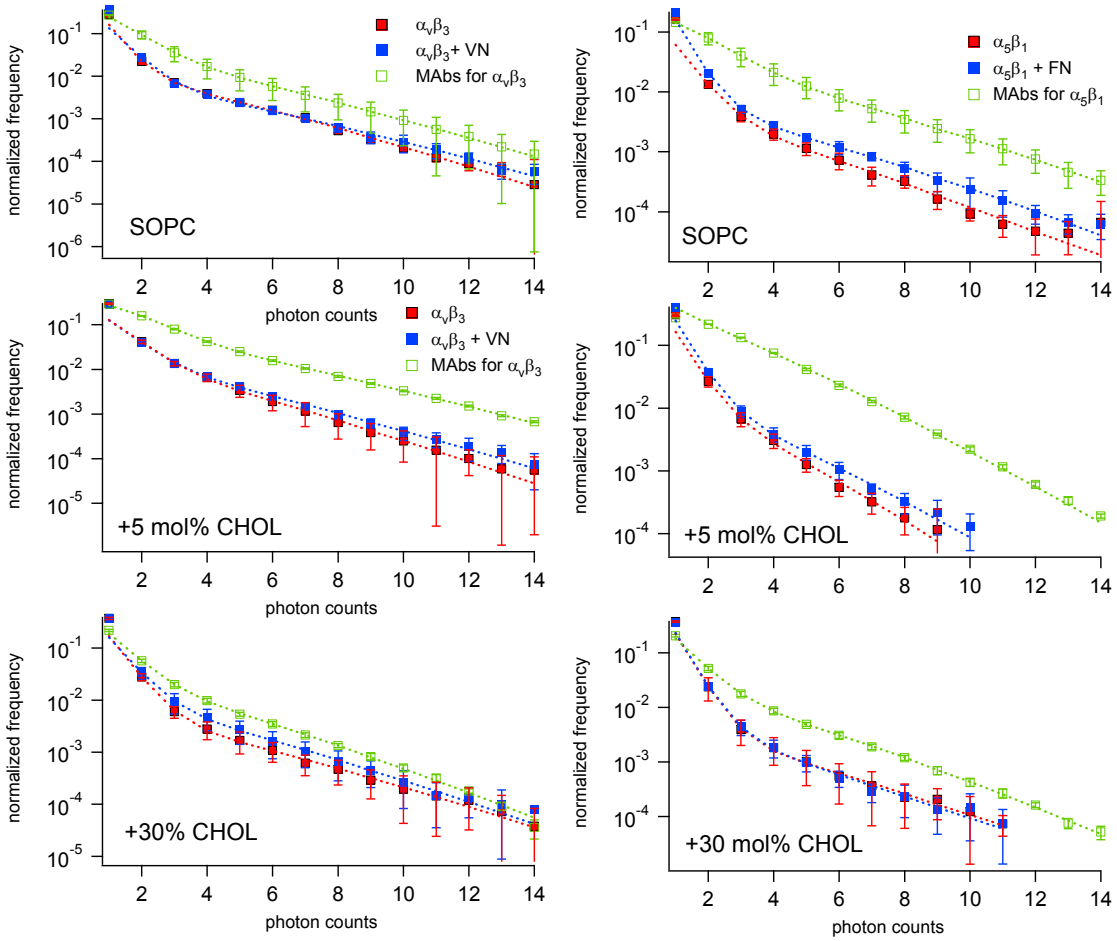

Figure 4.2.5 PCH curves for $\alpha_v\beta_3$ (A,C, E) and $\alpha_5\beta_1$ (B,D, F) before and after ligand binding in SOPC (A,B), SOPC + 5mol% CHOL (C,D), SOPC + 30 mol% CHOL (E,F) along with PCH curves for MAbs for integrins in solution. Dotted lines are best fit curves from PCH algorithm.

for these systems in each case within 15% of the best fit for the brightness of the MAbs in solution. The results for oligomerization state as deduced from solutions to the PCH algorithm are also shown in Fig. 4.2.5 For the $\alpha_v\beta_3$ system, X_{dimer} is below 5% for the CHOL free bilayer, but increases to 5-10 % for 5 mol% CHOL and then about 12% for the 30 mol% CHOL bilayer. The $\alpha_5\beta_1$ system shows the same trend, with possibly higher X_{dimer} (2-7%) found for 0% CHOL. This finding is interesting in light of the observation that reduction of CHOL levels leads to reduction in integrin functioning as observed by

reduction in cellular adhesion capabilities (33). More importantly, there is no statistical difference in oligomerization state before ligand binding (*red bars*) and after ligand binding (*blue bars*), with the possible exception of a moderate increase in oligomerization after ligand binding in the 5 mol% CHOL $\alpha_v\beta_3$ system.

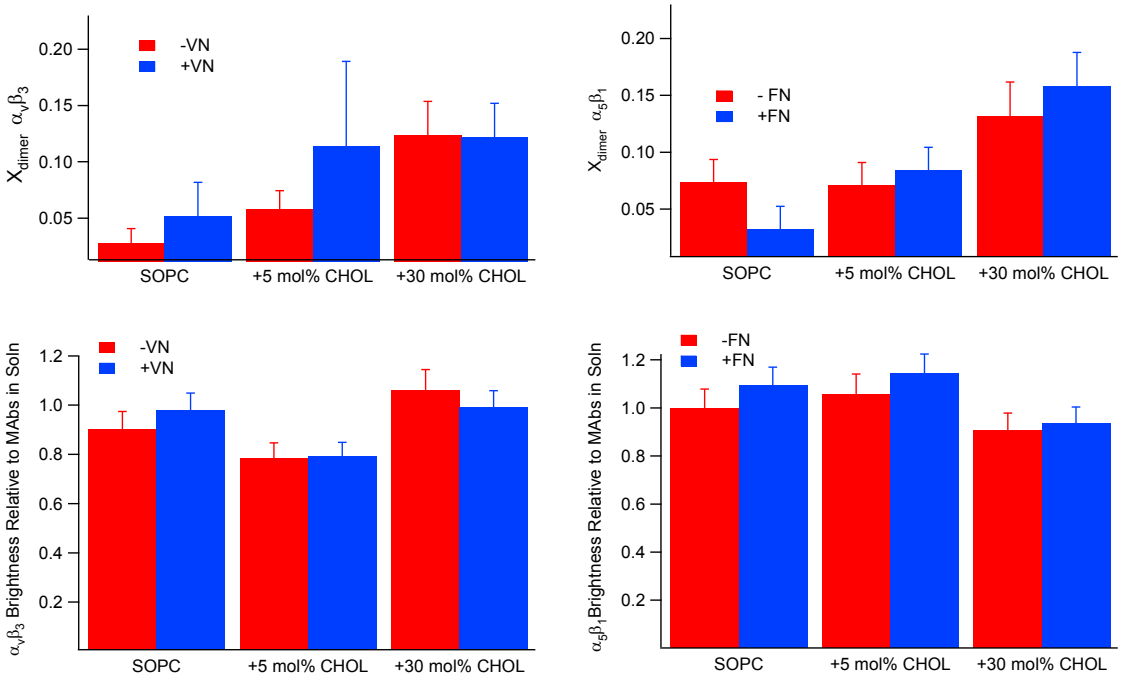

Figure 4.2.6 Fraction of dimers (A,B) and brightness relative to MAbs in solution (C,D) found through PCH analysis for $\alpha_v\beta_3$ (A, C) and $\alpha_5\beta_1$(B, D) before and after ligand binding. These data show that increasing CHOL increases oligomerization for both $\alpha_v\beta_3$ and $\alpha_5\beta_1$ but only to moderate levels

Following the characterization of integrin oligomerization in TYPE II bilayers, we conducted corresponding experiments on raft-mimicking TYPE I bilayers, utilizing the dual EPI/FFS set-up to acquire FFS data in l_o and l_d phases for both $\alpha_v\beta_3$ and $\alpha_5\beta_1$ before and after ligand addition for the purposes of analyzing oligomerization state in this system. The results of these studies are shown in Figure 4.2.6, which include the PCH

data sets as well as the findings for brightness relative to MAbs in solution and X_{dimer}. PCH analysis shows that the primary brightness of the integrins relative to the fluorescent MAbs in solution was found to be 77 ± 9% before ligand binding and 81 ± 9% after ligand binding, and thus essentially the same before and after ligand binding (Fig. 4.2.6(*E*)). The rate of dimerization was moderate, between 5 and 20 mol% for both $\alpha_v\beta_3$ and $\alpha_5\beta_1$ (Fig. 4.2.6(*F*)), thus mirroring the results found in the TYPE II bilayers. The current system has identified oligomerization state sensitively through the use of the PCH algorithm and found that raft sequestration due to monomeric, non-clustered ligands does not induce oligomerization in either $\alpha_v\beta_3$ or $\alpha_5\beta_1$ integrins.

Interestingly, our findings are in good agreement with an early study involving octyl-glucoside that quantified the average molecular weight of the integrin $\alpha_{IIb}\beta_3$ through centrifugation before and after addition of an RGD peptide ligand-mimetic (141). Their study showed only a 10% increase in molecular weight after ligand addition, and thus did not detect significant integrin oligomerization upon ligand addition, either. Our PCH data are also supported by an elegant cell study that found that ligand addition to $\alpha_v\beta_3$ or other forms of $\alpha_v\beta_3$ activation was not capable of inducing clustering in the absence of cytosolic-integrin linkages (39). This research, as well as our data, imply that $\alpha_v\beta_3$ integrin-ligand binding alone is insufficient for integrin clustering or oligomerization. $\alpha_5\beta_1$ clustering has been studied by monitoring the difference in strength of cellular adhesion (a proxy for integrin clustering) of magnetic beads coated with different

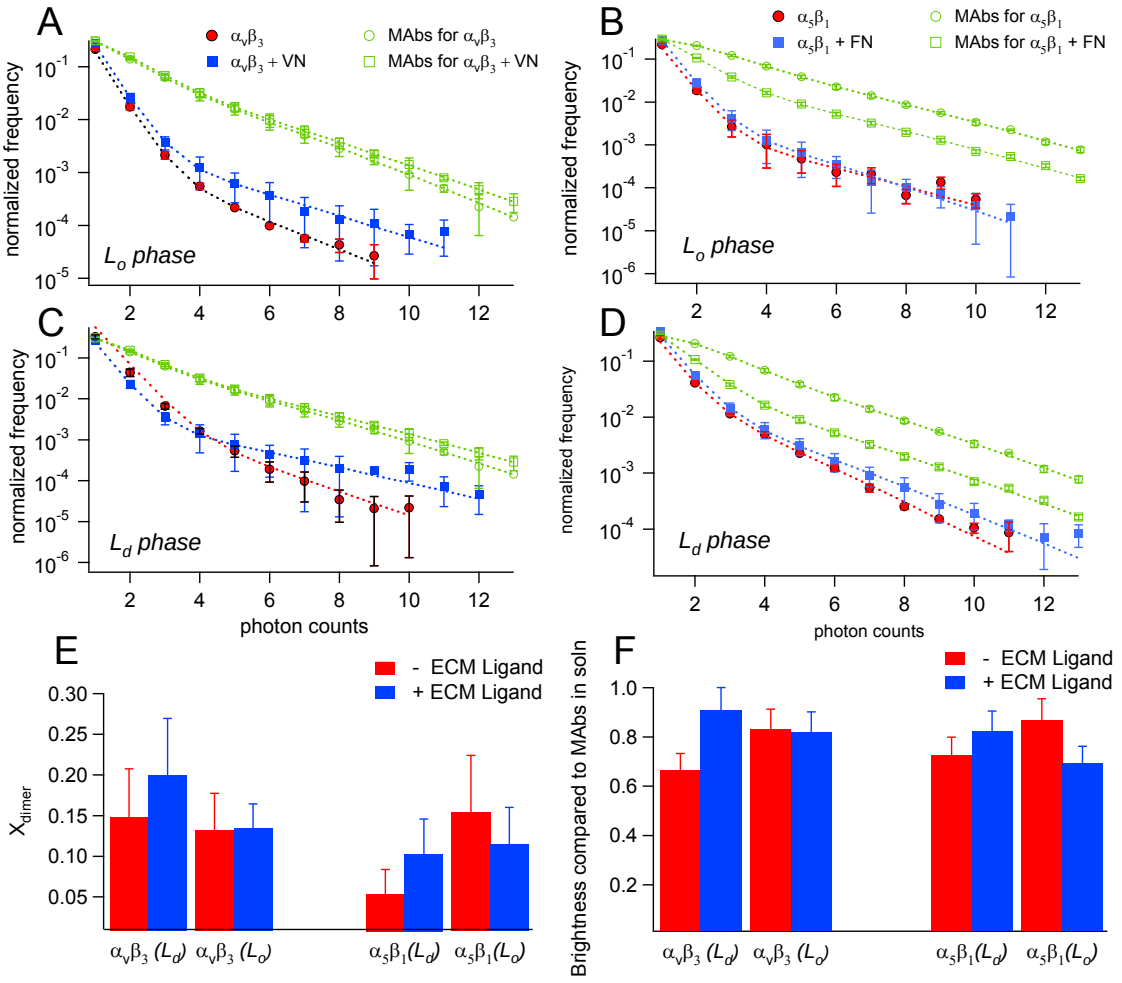

Figure 4.2.7 PCH curves for $\alpha_v\beta_3$ (A,C) and $\alpha_5\beta_1$ (B,D) before (red) and after (blue) ligand binding in both l_o phase (A,B) and l_d phase (C,D) along with PCH curves for MAbs for integrins in solution (green), MAbs data acquired twice, at the time of initial PCH acquisition (before ligand binding) and at the time of subsequent PCH addition (after ligand binding). Dotted lines are best fit curves from PCH algorithm. (E) Fraction of dimers and (F) Brightness compared to MAbs in solution found through PCH analysis of $\alpha_v\beta_3$ (left) and $\alpha_5\beta_1$ (right) integrin proteins before (red) and after (blue) ligand binding in l_d and l_o phases

.

concentrations of FN (142) or polymers linked with either 1.7, 3.6 or 5.4 RGD peptides (84). In both cases, cellular adhesion was significantly stronger (per ligand attached) for clustered ligands than for monovalent ligands, indicating that single ligands were not spontaneously forming clusters.

The combined integrin sequestering and PCH data clearly indicate that ligand binding does not affect X_{dimer} for either $\alpha_v\beta_3$ or $\alpha_5\beta_1$ in phase-separating TYPE I lipid mixtures. In other words, the observed ligand-mediated changes of $\alpha_v\beta_3$ and $\alpha_5\beta_1$ sequestering reported in Figs. 4.2.3-4.2.4 are not caused by changes in receptor oligomerization state. Moreover, the current study demonstrates the change in the fraction of proteins that dimerize before and after ligand binding (5% or less difference in X_{dimer} on ligand addition) is far less than the fraction of proteins that migrated from disordered to ordered lipid phases for both the $\alpha_5\beta_1$ system, where 27% migrated to induce an even distribution, and the $\alpha_v\beta_3$ system, where 54% migrated to the l_o phase to induce a clear preference for the l_o phase. This platform has therefore given us the ability to sensitively distinguish two separate aspects, namely raft-association and oligomerization state, and conclude that ligand binding, while sufficient to induce raft association, is not directly implicated in oligomerization.

Our data suggest that the observed protein sequestering is due to ligand-induced conformational changes of integrins impacting integrin-lipid interactions. It is well known that ligand addition causes substantial structural changes to both the ectodomains and the transmembrane domains of integrins. Electron microscopy studies have analyzed the head group conformation of the EC domains of both $\alpha_v\beta_3$ and $\alpha_5\beta_1$ in solution before and after quantitative exposure to RGD peptides designed to mimic ECM ligands (143, 144). Both $\alpha_v\beta_3$ and $\alpha_5\beta_1$ integrin fragments started in the resting, bent conformations before exposure to the ligands. After ligand exposure, 98% of the $\alpha_v\beta_3$ head groups adopted an open conformation, even in the absence of the known activating factor, Mn^{2+}

(143) and 25% of the $\alpha_5\beta_1$ protein extracellular domains switched to the open conformation (144). The position of the head groups in relation to the membrane also changes: integrins in the bent, resting position have the RGD binding pocket near the plasma membrane but when activated, the RGD binding pocket is thought to straighten out and pull far from the membrane (88). These changes in the ectodomain may influence the observed change in sequestration directly by altering the ectodomain-membrane interface, or indirectly by inducing changes in the integrin transmembrane domains. Furthermore, studies on mutations of integrins indicate that the transmembrane domains of the alpha and beta subunits are associated with substantial conformational changes in response to external stimuli during processes associated with integrin outside in and inside out signaling (145). Such conformational changes likely expose different residues and increase the number of residues in the beta subunit that reside within the lipid membrane thus changing the tilt angle of the beta subunit (146). This process may impact the mismatch between the integrin transmembrane domain and the hydrophobic region of the lipid bilayer (147).

CHAPTER 5 CONCLUSIONS

In this work polymer-tethered lipids were used to investigate aspects of "microscale" membrane organization through a study of the thin-film buckling behavior of lipopolymer-enriched lipid monolayers and "molecular-scale" organization of a lipid membrane through a study of the sequestration and oligomerization state of the membrane proteins $\alpha_v\beta_3$ and $\alpha_5\beta_1$ on cholesterol-enriched model membranes, in the absence and presence of ECM ligands. Both of these investigations hinged on the ability to construct polymer-enriched lipid monolayers and bilayers and use multiple forms of microscopy to extract information about the large scale mechanical response of membranes and the single molecule response of membrane proteins. Both of these studies have important insight into lipid membranes and can be used as the basis for further investigations: on one end, further studies of the mechanical properties of lipid membranes and at the other end, protein-protein interactions in well controlled lipid environments with single molecule sensitivity.

The first objective was construction and characterization of buckling patterns that act as diffusion barriers in lipopolymer-enriched lipid bilayers. These were found to be caused by thin-film buckling, and not heterogeneous unmixing of lipids and lipopolymers or crystallization or dewetting of the substrate. While buckling occurred for methyloxazoline and ethyloxazoline polymer moieties, it was found that methyloxazoline

buckles did not induce the formation of large scale diffusion barriers while ethyloxazoline buckles did. This was attributed to the increased lipophilicity of the ethyloxazoline moiety enabling it to penetrate into the lipid monolayer in the region of the buckles, and thereby cause a lipid bilayer not to form over the buckled regions.

Motivated by the ability to obtain reproducible buckling patterns with ethyloxazoline lipopolymers, the second objective, a systematic investigation of the thin-film buckling response of polyethylene glycol lipopolymers (PEG5000) was undertaken. This was aided in part by an early observation that it was possible to form diffusion barrier-containing fluid lipid bilayers over monolayers constructed with DSPE-PEG5000 concentrations as varied as 3-40 mol% DSPE-PEG5000 mixed with SOPC. These lipopolymer concentrations enable the investigation of thin films with very different plane strain moduli (4x variation) and bending stiffnesses (20x variation) deposited on glass substrates. In a mathematical sense, this is akin to investigating lipid membranes of a constant plane strain modulus and bending stiffness but varying the substrate's plane strain modulus by a factor of 4 and its bending stiffness by a factor of 20. The results showed that as the lipid monolayers were made stiffer, the loading parameter decreased and the percentage of buckled area increased. The decrease in loading parameter meant that less energy was necessary to cause buckling. In addition, the form of buckling altered from more labyrinthine to more network-like as the stiffness of the monolayer more closely approached the stiffness of the substrate. Additional parameters from buckling theory including the loading parameter, the critical stiffness ratio, the relative

delamination size, and the energy penalty for a given loading parameter were also analyzed in light of the buckling data presented.

These results are important because they show the ability to induce compartmentalized bilayers with different bending stiffnesses in a systematic manner. These may prove useful for bilayer-cell studies or other systems where hydrophilic/hydrophobic thin film micropatterning can be utilized, including such fields as biosensor development (148). In addition, the DSPE-PEG5000 study showed that as the plane strain modulus of the film and the substrate became more alike, less energy was necessary to induce buckling, the buckling that was caused was more widespread, and the buckling pattern was better networked (less fractal). In short, the change in critical stiffness ratio induced a change in buckling response by the thin film. A similar mechanical response to changes in substrate thickness would be expected to occur on live cells. Future studies in this area could involve systematically changing the stiffness of the lipid monolayers without varying the thickness of the polymers, for example by the addition of cholesterol which increases film thickness of the lipid layer but only moderately. In addition, it would be interesting to deposit lipopolymer/lipid monolayers on substrates less stiff than glass to further explore the effects of changes in the loading parameter on buckling patterns. Utilizing shorter lipopolymers would probably not be very fruitful as the minimum X_p to observe buckling would increase significantly, as can be calculated from the known parameters.

Investigations at the molecular level involved incorporation of $\alpha_v\beta_3$ and $\alpha_5\beta_1$ into polymer-tethered cholesterol-enriched phospholipid bilayers in order to probe the effect of ligand addition on sequestration behavior and oligomerization state of these proteins. First, proper incorporation and fluidity of the membrane proteins was checked by single molecule fluorescence microscopy, FCS and EPI. For the next objective, the sequestration of these proteins was investigated using ternary (DOPC:DPPC:CHOL) phase separating lipid mixtures through CS- XY scans. These enabled quantification of *Kp* and E_{raft} for the proteins, and showed that both preferred the l_d phase in their resting, native state. After ligand addition, $\alpha_v\beta_3$ switched preferences and sequestered preferentially in the l_o phase, while $\alpha_5\beta_1$ switched to showing no preference for either the l_o or l_d phase. Next, the oligomerization state of the $\alpha_v\beta_3$ and $\alpha_5\beta_1$ proteins in both the l_o and l_d phases was probed using fluorescence fluctuation spectroscopy and PCH analysis. The rate of dimerization was found to be moderate for both $\alpha_v\beta_3$ and $\alpha_5\beta_1$ in both l_o and l_d phases, and significantly, was not found to be substantially affected by ligand addition. In TYPE II bilayers, a trend for increasing oligomerization with increasing cholesterol levels was found. In addition, in these systems as well as in the ternary lipid systems, ligand binding had little effect on the rate of oligomerization.

These results are important because they show, for the first time, the ability to combine studies of sequestration and oligomerization in well-defined model systems. Since integrin functionality related to cellular adhesion or angiogenesis involves microclustering of integrins, this further shows that the ligands and the cholesterol in the rafts alone are insufficient by themselves to induce the conditions involving the formation

of microclusters of $\alpha_v\beta_3$ or $\alpha_5\beta_1$ proteins. These results were found without the use of crosslinking agents prevalent in many systems studying integrins and lipid rafts. The versatility of the platform enables the incorporation of other membrane proteins or extracellular proteins to the system to monitor their effect on the oligomerization state and sequestration of the integrins here studied, or the adoption of a new set of proteins. It would also be very interesting to construct model systems with non-bilayer spanning domains to investigate the role of single-membrane phase separations in protein sequestration. These could be used to analyze whether the cytosolic tail of the integrins or the extracellular head-group is more involved in cholesterol-protein interactions. Based on the ligands' binding in the extracellular domain (top leaflet in the model studies), it would seem likely that these interactions are more important but the ligand binding is also thought to induce a large scale change in the protein conformation (127, 149) which may affect the cytosolic domain (bottom leaflet in model studies) more closely.

LIST OF REFERENCES

LIST OF REFERENCES

1. Wirtz, H., and L. G. Dobbs. 1990. Calcium mobilization and exocytosis after one mechanical stretch of lung epithelial cells. *Science*. 250:1266.

2. Longo, M., A. Bisagno, J. Zasadzinski, R. Bruni, and A. Waring. 1993. A function of lung surfactant protein SP-B. *Science*. 261:453.

3. Takamoto, D., M. Lipp, A. Von Nahmen, K. Y. C. Lee, A. Waring, and J. Zasadzinski. 2001. Interaction of lung surfactant proteins with anionic phospholipids. *Biophys. J.* 81:153-169.

4. de La Serna, J. B., G. Oradd, L. A. Bagatolli, A. C. Simonsen, D. Marsh, G. Lindblom, and J. Perez-Gil. 2009. Segregated phases in pulmonary surfactant membranes do not show coexistence of lipid populations with differentiated dynamic properties. *Biophys. J.* 97:1381-1389.

5. Hallett, M. B., and S. Dewitt. 2007. Ironing out the wrinkles of neutrophil phagocytosis. *Trends Cell Biol.* 17:209-214.

6. Dewitt, S., and M. Hallett. 2007. Leukocyte membrane" expansion": a central mechanism for leukocyte extravasation. *J. Leukocyte Biol.* 81:1160.

7. Brunner, C., A. Niendorf, and J. A. Käs. 2009. Passive and active single-cell biomechanics: a new perspective in cancer diagnosis. *Soft Matter*. 5:2171-2178.

8. Hwang, W. C., and R. E. Waugh. 1997. Energy of dissociation of lipid bilayer from the membrane skeleton of red blood cells. *Biophys. J.* 72:2669-2678.

9. Solon, J., I. Levental, K. Sengupta, P. C. Georges, and P. A. Janmey. 2007. Fibroblast adaptation and stiffness matching to soft elastic substrates. *Biophys J*. 93:4453-4461.

10. Trickey, W. R., T. P. Vail, and F. Guilak. 2004. The role of the cytoskeleton in the viscoelastic properties of human articular chondrocytes. *J. Ortho. Res.* 22:131-139.

11. Takai, E., K. D. Costa, A. Shaheen, C. T. Hung, and X. E. Guo. 2005. Osteoblast elastic modulus measured by atomic force microscopy is substrate dependent. *Ann. Biomed. Eng.* 33:963-971.

12. Simson, R., E. Wallraff, J. Faix, J. Niewöhner, G. Gerisch, and E. Sackmann. 1998. Membrane Bending Modulus and Adhesion Energy of Wild-Type and Mutant Cells of Dictyostelium Lacking Talin or Cortexillins. *Biophys. J.* 74:514-522.

13. Tseng, Y., J. S. H. Lee, T. P. Kole, I. Jiang, and D. Wirtz. 2004. Micro-organization and visco-elasticity of the interphase nucleus revealed by particle nanotracking. *J. Cell Sci.* 117:2159-2167.

14. Kamgoué, A., J. Ohayon, and P. Tracqui. 2007. Estimation of Cell Young's Modulus of Adherent Cells Probed by Optical and Magnetic Tweezers: Influence of Cell Thickness and Bead Immersion. *J. Biomech. Eng.* 129:523-530.

15. Janmey, P., and P. Kinnunen. 2006. Biophysical properties of lipids and dynamic membranes. *Trends Cell Biol*. 16:538-546.

16. Zimmerberg, J., and M. M. Kozlov. 2005. How proteins produce cellular membrane curvature. *Nat. Rev. Mol. Cell Biol.* 7:9-19.

17. Welti, R., and M. Glaser. 1994. Lipid domains in model and biological membranes. *Chem. Phys. Lipids*. 73:121-137.

18. Simons, K., and E. Ikonen. 1997. Functional rafts in cell membranes. *Nature*. 387:569-572.

19. Edidin, M. 2001. Shrinking patches and slippery rafts: scales of domains in the plasma membrane. *Trends Cell Biol.* 11:492-496.

20. Edidin, M. 2003. THE STATE OF LIPID RAFTS: From Model Membranes to Cells. *Ann. Rev. Bioph. Biom.* . 32:257-283.

21. Simons, K., and M. J. Gerl. 2010. Revitalizing membrane rafts: new tools and insights. *Nat. Rev. Mol. Cell Biol.* 11:688-699.

22. Lingwood, D., and K. Simons. 2010. Lipid Rafts As a Membrane-Organizing Principle. *Science*. 327:46-50.

23. Larson, D. R., J. A. Gosse, D. A. Holowka, B. A. Baird, and W. W. Webb. 2005. Temporally resolved interactions between antigen-stimulated IgE receptors and Lyn kinase on living cells. *J. Cell Biol.* 171:527.

24. Pyenta, P. S., D. Holowka, and B. Baird. 2001. Cross-Correlation Analysis of Inner-Leaflet-Anchored Green Fluorescent Protein Co-Redistributed with IgE Receptors and Outer Leaflet Lipid Raft Components. *Biophys. J.* 80:2120-2132.

25. Holowka, D., J. A. Gosse, A. T. Hammond, X. Han, P. Sengupta, N. L. Smith, A. Wagenknecht-Wiesner, M. Wu, R. M. Young, and B. Baird. 2005. Lipid segregation and IgE receptor signaling: a decade of progress. *Biochim. Biophys. Acta, Mol. Cell Res.* 1746:252-259.

26. Gaus, K., E. Chklovskaia, B. Fazekas de St Groth, W. Jessup, and T. Harder. 2005. Condensation of the plasma membrane at the site of T lymphocyte activation. *J. Cell Biol.* 171:121.

27. Pelkmans, L. 2005. Secrets of caveolae-and lipid raft-mediated endocytosis revealed by mammalian viruses. *Biochim. Biophys. Acta, Mol. Cell Res.* 1746:295-304.

28. Plowman, S. J., C. Muncke, R. G. Parton, and J. F. Hancock. 2005. H-ras, K-ras, and inner plasma membrane raft proteins operate in nanoclusters with differential dependence on the actin cytoskeleton. *Proc. Natl. Acad. Sci. U. S. A.* 102:15500.

29. Carman, C. V., and T. A. Springer. 2003. Integrin avidity regulation: are changes in affinity and conformation underemphasized? *Curr. Opin. Cell Biol.* 15:547-556.

30. Depry, C., M. D. Allen, and J. Zhang. 2010. Visualization of PKA activity in plasma membrane microdomains. *Mol. BioSyst.*

31. Gopalakrishna, P., N. Rangaraj, and G. Pande. 2004. Cholesterol alters the interaction of glycosphingolipid GM3 with [alpha]5[beta]1 integrin and increases integrin-mediated cell adhesion to fibronectin. *Exp. Cell Res.* 300:43-53.

32. Ehehalt, R., P. Keller, C. Haass, C. Thiele, and K. Simons. 2003. Amyloidogenic processing of the Alzheimer -amyloid precursor protein depends on lipid rafts. *J. Cell Biol.* 160:113.

33. Dibya, D., N. Arora, and E. A. Smith. 2010. Noninvasive Measurements of Integrin Microclustering under Altered Membrane Cholesterol Levels. *Biophys. J.* 99:853-861.

34. Marwali, M. R., J. Rey-Ladino, L. Dreolini, D. Shaw, and F. Takei. 2003. Membrane cholesterol regulates LFA-1 function and lipid raft heterogeneity. *Blood*. 102:215.

35. Ganguly, S., and A. Chattopadhyay. 2010. Cholesterol Depletion Mimics the Effect of Cytoskeletal Destabilization on Membrane Dynamics of the Serotonin1A Receptor: A zFCS Study. *Biophys. J*. 99:1397-1407.

36. Chichili, G. R., and W. Rodgers. 2009. Cytoskeleton–membrane interactions in membrane raft structure. *Cell Mol. Life Sci.* 66:2319-2328.

37. van Zanten, T. S., A. Cambi, M. Koopman, B. Joosten, C. G. Figdor, and M. F. Garcia-Parajo. 2009. Hotspots of GPI-anchored proteins and integrin nanoclusters function as nucleation sites for cell adhesion. *Proc. Natl. Acad. Sci. U. S. A.* 106:18557-18562.

38. Bunch, T. A. 2010. Integrin αIIbβ3 Activation in Chinese Hamster Ovary Cells and Platelets Increases Clustering Rather than Affinity. *J. Biol. Chem*. 285:1841-1849.

39. Cluzel, C., F. Saltel, J. Lussi, F. Paulhe, B. A. Imhof, and B. Wehrle-Haller. 2005. The mechanisms and dynamics of v 3 integrin clustering in living cells. *J. Cell Biol.* 171:383.

40. Silvius, J. R. 2005. Partitioning of membrane molecules between raft and non-raft domains: Insights from model-membrane studies. *Biochim. Biophys. Acta, Mol. Cell Res.* 1746:193-202.

41. Purrucker, O., S. Gönnenwein, A. Förtig, R. Jordan, M. Rusp, M. Bärmann, L. Moroder, E. Sackmann, and M. Tanaka. 2007. Polymer-tethered membranes as quantitative models for the study of integrin-mediated cell adhesion. *Soft Matter*. 3:333-336.

42. Garg, S., J. Rühe, K. Lüdtke, R. Jordan, and C. A. Naumann. 2007. Domain registration in raft-mimicking lipid mixtures studied using polymer-tethered lipid bilayers. *Biophys. J*. 92:1263-1270.

43. Rawicz, W., K. Olbrich, T. McIntosh, D. Needham, and E. Evans. 2000. Effect of chain length and unsaturation on elasticity of lipid bilayers. *Biophys. J.* 79:328-339.

44. Marsh, D. 2006. Elastic curvature constants of lipid monolayers and bilayers. *Chem. Phys. Lipids*. 144:146-159.

45. Sackmann, E. 1994. Membrane bending energy concept of vesicle-and cell-shapes and shape-transitions. *FEBS Lett.* 346:3-16.

46. Helfer, E., S. Harlepp, L. Bourdieu, J. Robert, F. C. MacKintosh, and D. Chatenay. 2001. Buckling of Actin-Coated Membranes under Application of a Local Force. *Phys. Rev. Lett.* 87:088103.

47. Marsh, D., R. Bartucci, and L. Sportelli. 2003. Lipid membranes with grafted polymers: physicochemical aspects. *Biochim. Biophys. Acta, Biomembr.* 1615:33-59.

48. Rovira-Bru, M., D. Thompson, and I. Szleifer. 2002. Size and Structure of Spontaneously Forming Liposomes in Lipid/PEG-Lipid Mixtures. *Biophys. J.* 83:2419-2439.

49. Purrucker, O., A. Förtig, R. Jordan, and M. Tanaka. 2004. Supported Membranes with Well-Defined Polymer Tethers - Incorporation of Cell Receptors. *ChemPhysChem*. 5:327-335.

50. Kiessling, V., C. Wan, and L. Tamm. 2009. Domain coupling in asymmetric lipid bilayers. *Biochim. Biophys. Acta, Biomembr.* 1788:64-71.

51. Dietrich, C., L. Bagatolli, Z. Volovyk, N. Thompson, M. Levi, K. Jacobson, and E. Gratton. 2001. Lipid rafts reconstituted in model membranes. *Biophys. J*. 80:1417-1428.

52. Kahya, N., D. A. Brown, and P. Schwille. 2005. Raft Partitioning and Dynamic Behavior of Human Placental Alkaline Phosphatase in Giant Unilamellar Vesicles. *Biochemistry*. 44:7479-7489.

53. Saslowsky, D. E., J. Lawrence, X. Ren, D. A. Brown, R. M. Henderson, and J. M. Edwardson. 2002. Placental alkaline phosphatase is efficiently targeted to rafts in supported lipid bilayers. *J. Biol. Chem*. 277:26966.

54. Khan, T. K., B. Yang, N. L. Thompson, S. Maekawa, R. M. Epand, and K. Jacobson. 2003. Binding of NAP-22, a calmodulin-binding neuronal protein, to raft-like domains in model membranes. *Biochemistry*. 42:4780-4786.

55. Sengupta, P., A. Hammond, D. Holowka, and B. Baird. 2008. Structural determinants for partitioning of lipids and proteins between coexisting fluid phases in giant plasma membrane vesicles. *Biochim. Biophys. Acta, Biomembr.* 1778:20-32.

56. Dietrich, C., Z. Volovyk, M. Levi, N. Thompson, and K. Jacobson. 2001. Partitioning of Thy-1, GM1, and cross-linked phospholipid analogs into lipid rafts reconstituted in supported model membrane monolayers. *Proc. Natl. Acad. Sci. U. S. A.* 98:10642-10647.

57. Kalvodova, L., N. Kahya, P. Schwille, R. Ehehalt, P. Verkade, D. Drechsel, and K. Simons. 2005. Lipids as Modulators of Proteolytic Activity of BACE. *J. Biol. Chem*. 280:36815-36823.

58. Baumgart, T., A. T. Hammond, P. Sengupta, S. T. Hess, D. A. Holowka, B. A. Baird, and W. W. Webb. 2007. Large-scale fluid/fluid phase separation of proteins and lipids in giant plasma membrane vesicles. *Proc. Natl. Acad. Sci. U. S. A.* 104:3165-3170.

59. Hammond, A. T., F. A. Heberle, T. Baumgart, D. Holowka, B. Baird, and G. W. Feigenson. 2005. Crosslinking a lipid raft component triggers liquid ordered-liquid disordered phase separation in model plasma membranes. *Proc. Natl. Acad. Sci. U. S. A.* 102:6320-6325.

60. Siegel, A. P., M. J. Murcia, M. Johnson, M. Reif, R. Jordan, J. Rühe, and C. A. Naumann. 2010. Compartmentalizing a lipid bilayer by tuning lateral stress in a physisorbed polymer-tethered membrane. *Soft Matter*. 6:2723-2732.

61. Deverall, M. A., E. Gindl, E. K. Sinner, H. Besir, J. Rühe, M. J. Saxton, and C. A. Naumann. 2005. Membrane lateral mobility obstructed by polymer-tethered lipids studied at the single molecule level. *Biophys. J.* 88:1875-1886.

62. Albertorio, F., A. Diaz, T. Yang, V. Chapa, S. Kataoka, E. Castellana, and P. Cremer. 2005. Fluid and Air-Stable Lipopolymer Membranes for Biosensor Applications. *Langmuir*. 21:7476-7482.

63. Galush, W. J., J. A. Nye, and J. T. Groves. 2008. Quantitative Fluorescence Microscopy Using Supported Lipid Bilayer Standards. *Biophys. J.* 95:2512-2519.

64. Binnig, G., C. F. Quate, and C. Gerber. 1986. Atomic Force Microscope. *Phys. Rev. Lett.* 56:930.

65. Elson, E. L., and D. Magde. 1974. Fluorescence correlation spectroscopy. I. Conceptual basis and theory. *Biopolymers*. 13:1-27.

66. Chen, Y., J. Müller, P. So, and E. Gratton. 1999. The Photon Counting Histogram in Fluorescence Fluctuation Spectroscopy. *Biophys J*. 77:553-567.

67. Huang, B., T. D. Perroud, and R. N. Zare. 2004. Photon Counting Histogram: One-Photon Excitation. *ChemPhysChem*. 5:1523-1531.

68. Magde, D., E. L. Elson, and W. W. Webb. 1974. Fluorescence correlation spectroscopy. II. An experimental realization. *Biopolymers*. 13:29-61.

69. Schwille, P., U. Haupts, S. Maiti, and W. W. Webb. 1999. Molecular Dynamics in Living Cells Observed by Fluorescence Correlation Spectroscopy with One- and Two-Photon Excitation. *Biophys. J*. 77:2251-2265.

70. Hu, X., and D. Cruden. 1993. Buckling deformation in the Highwood Pass, Alberta, Canada. *Can. Geotech. J.* 30:276-276.

71. Malla, R. B., and A. Ghoshal. 1995. Thermally induced vibrations of structures in space. *Aerospace thermal structures and materials for a new era*. 168:68.

72. Pangule, R. C., I. Banerjee, and A. Sharma. 2008. Adhesion induced mesoscale instability patterns in thin PDMS-metal bilayers. *J. Chem. Phys.* 128:-.

73. Jiang, C., S. Singamaneni, E. Merrick, and V. V. Tsukruk. 2006. Complex buckling instability patterns of nanomembranes with encapsulated gold nanoparticle arrays. *Nano letters*. 6:2254-2259.

74. Yoo, P. J., K. Y. Suh, S. Y. Park, and H. H. Lee. 2002. Physical self-assembly of microstructures by anisotropic buckling. *Adv. Mater.* 14:1383-1387.

75. Lee, K. Y. C. 2008. Collapse mechanisms of Langmuir monolayers. *Ann. Rev. Phys. Chem.* 59:771-791.

76. Mei, H., R. Huang, J. Y. Chung, C. M. Stafford, and H. H. Yu. 2007. Buckling modes of elastic thin films on elastic substrates. *Appl. Phys. Lett.* 90:151902.

77. Meier, W. P., and W. Knoll, editors. 2010. Polymer Membranes/Biomembranes (Advances in Polymer Science, vol. 224). Springer, New York.

78. Marsh, D. 2001. Elastic Constants of Polymer-Grafted Lipid Membranes. *Biophys. J.* 81:2154-2162.

79. Singer, S. J., and G. L. Nicolson. 1972. The fluid mosaic model of the structure of cell membranes. *Science*. 175:720-731.

80. Lee, A. G. 2003. Lipid-protein interactions in biological membranes: a structural perspective. *Biochim. Biophys. Acta, Biomembr.* 1612:1-40.

81. Crockett, E. L. 1998. Cholesterol Function in Plasma Membranes from Ectotherms: Membrane-Specific Roles in Adaptation to Temperature. *Amer. Zool.* 38:14.

82. Barenholz, Y. 2004. Sphingomyelin and cholesterol: from membrane biophysics and rafts to potential medical applications. *Subcell. Biochem.* 37:167-215.

83. De Almeida, R. 2003. Sphingomyelin/Phosphatidylcholine/Cholesterol Phase Diagram: Boundaries and Composition of Lipid Rafts. *Biophys. J.* 85:2406-2416.

84. Koo, L. Y., D. J. Irvine, A. M. Mayes, D. A. Lauffenburger, and L. G. Griffith. 2002. Co-regulation of cell adhesion by nanoscale RGD organization and mechanical stimulus. *J. Cell Sci.* 115:1423-1433.

85. Pande, G. 2000. The role of membrane lipids in regulation of integrin functions. *Curr. Opin. Cell Biol.* 12:569-574.

86. Xiong, J.-P., B. Mahalingham, J. L. Alonso, L. A. Borrelli, X. Rui, S. Anand, B. T. Hyman, T. Rysiok, D. Müller-Pompalla, S. L. Goodman, and M. A. Arnaout. 2009. Crystal structure of the complete integrin αVβ3 ectodomain plus an α/β transmembrane fragment. *J. Cell Biol.* 186:589-600.

87. Mitchell, J. S., W. S. Brown, D. G. Woodside, P. Vanderslice, and B. W. McIntyre. 2009. Clustering T-cell GM1 lipid rafts increases cellular resistance to shear on fibronectin through changes in integrin affinity and cytoskeletal dynamics. *Immunol. Cell Biol.* 87:324-336.

88. Luo, B. H., C. V. Carman, and T. A. Springer. 2007. Structural basis of integrin regulation and signaling. *Ann. Rev. Immun.* 25:619.

89. Albelda, S. M., S. A. Mette, D. E. Elder, R. M. Stewart, L. Damjanovich, M. Herlyn, and C. A. Buck. 1990. Integrin distribution in malignant melanoma: association of the 3 subunit with tumor progression. *Cancer Res.* 50:6757.

90. Lehman, J. T. 1999. Synthese von kovalent an Oberfla¨chen fixierten Polyethyloxazolinfilmen zum Aufbau polymergestu¨ tzter Biomembran-Modelle. Gutenberg-Universitat Mainz, Mainz.

91. Lüdtke, K., R. Jordan, P. Hommes, O. Nuyken, and C. A. Naumann. 2005. Lipopolymers from New 2-Substituted-2-Oxazolines for Artificial Cell Membrane Constructs. *Macromol Biosci*. 5:384-393.

92. Jordan, R., K. Martin, H. J. Räder, and K. K. Unger. 2001. Lipopolymers for Surface Functionalizations. 1. Synthesis and Characterization of Terminal Functionalized Poly(N-propionylethylenimine)s. *Macromolecules*. 34:8858-8865.

93. Jordan, R., K. Graf, H. Riegler, and K. K. Unger. 1996. Polymer-supported alkyl monolayers on silica: synthesis and self-assembly of terminal functionalized poly(N-propionylethylenimine)s. *Chem.Commun.*:1025-1026.

94. Murcia, M., D. Minner, G.-M. Mustata, K. Ritchie, and C. Naumann. 2008. Design of Quantum Dot-Conjugated Lipids for Long-Term, High-Speed Tracking Experiments on Cell Surfaces. *J. Am. Chem. Soc.* 130:15054-15062.

95. Rigaud, J.-L., and D. Levy. 2003. Reconstitution of Membrane Proteins into Liposomes. In *Methods Enzymol*. D. Nejat, editor. Academic Press. 65-86.

96. Rigaud, J. L., D. Levy, G. Mosser, and O. Lambert. 1998. Detergent removal by non-polar polystyrene beads. *Euro. Biophys. J.* 27:305-319.

97. Wang, W., and Y. Chau. 2009. Self-assembled peptide nanorods as building blocks of fractal patterns. *Soft Matter*. 5:4893-4898.

98. Audoly, B. 1999. Stability of straight delamination blisters. *Phys. Rev. Lett.* 83:4124-4127.

99. Hutchinson, J., and Z. Suo. 1992. Mixed mode cracking in layered materials. *Adv. in Appl. Mech.* 29:191.

100. Macdonald, P., Y. Chen, X. Wang, Y. Chen, and J. Mueller. 2010. Brightness Analysis by Z-Scan Fluorescence Fluctuation Spectroscopy for the Study of Protein Interactions within Living Cells. *Biophys. J.* 99:979-988.

101. Chen, Y., L. N. Wei, and J. D. Müller. 2003. Probing protein oligomerization in living cells with fluorescence fluctuation spectroscopy. *Proc. Natl. Acad. Sci. U. S. A.* 100:15492.

102. Jacobson, K., O. G. Mouritsen, and R. G. W. Anderson. 2007. Lipid rafts: at a crossroad between cell biology and physics. *Nat. Cell Biol.* 9:7-14.

103. Deverall, M. A., S. Garg, K. Lüdtke, R. Jordan, J. Rühe, and C. A. Naumann. 2008. Transbilayer coupling of obstructed lipid diffusion in polymer-tethered phospholipid bilayers. *Soft Matter*. 4:1899-1908.

104. Frey, S., D. Zhang, M. Carignano, I. Szleifer, and K. Y. Lee. 2007. Effects of block copolymer's architecture on its association with lipid membranes: experiments and simulations. *J. Chem. Phys.* 127.

105. Purrucker, O., A. Förtig, K. Ludtke, R. Jordan, and M. Tanaka. 2005. Confinement of Transmembrane Cell Receptors in Tunable Stripe Micropatterns. *J. Am. Chem. Soc.* 127:1258-1264.

106. Reiter, G., G. Castelein, and J. U. Sommer. 2002. Pattern formation and ordering in thin films of crystallisable block copolymers. Wiley Online Library. 173-178.

107. Braun, H. G., and E. Meyer. 2008. Pattern formation in ultrathin polymer films prepared on microstructured surfaces. *Journal of Physics: Conference Series*. 126:012027.

108. Naumann, C. A., C. F. Brooks, G. G. Fuller, T. Lehmann, J. Rühe, W. Knoll, P. Kuhn, O. Nuyken, and C. W. Frank. 2001. Two-Dimensional Physical Networks of Lipopolymers at the Air/Water Interface: Correlation of Molecular Structure and Surface Rheological Behavior. *Langmuir*. 17:2801-2806.

109. Edmondson, S., K. Frieda, J. E. Comrie, P. R. Onck, and W. T. S. Huck. 2006. Buckling in Quasi 2D Polymers. *Adv. Mater.* 18:724-728.

110. Karapanagiotis, I., W. W. Gerberich, and D. F. Evans. 2001. Early dewetting stages of thin polymer films initiated by nanoindentation. *Langmuir*. 17:2375-2379.

111. Stange, T., D. Evans, and W. Hendrickson. 1997. Nucleation and growth of defects leading to dewetting of thin polymer films. *Langmuir*. 13:4459-4465.

112. Lüdtke, K., R. Jordan, N. Furr, S. Garg, K. Forsythe, and C. A. Naumann. 2008. Two-Dimensional Center-of-Mass Diffusion of Lipid-Tethered Poly (2-methyl-2-oxazoline) at the Air–Water Interface Studied at the Single Molecule Level. *Langmuir*. 24:5580-5584.

113. Parry, G., J. Colin, C. Coupeau, F. Foucher, A. Cimetière, and J. Grilhé. 2005. Snapthrough occurring in the postbuckling of thin films. *Appl. Phys. Lett.* 86:081905.

114. Jagla, E. 2007. Modeling the buckling and delamination of thin films. *Phys. Rev. B*. 75:085405.

115. Volinsky, A. A. 2005. Sub-critical telephone cord delamination propagation and adhesion measurements. UNIVERSITY OF SOUTH FLORIDA TAMPA DEPT OF MECHANICAL ENGINEERING.

116. Szleifer, I., O. V. Gerasimov, and D. H. Thompson. 1998. Spontaneous liposome formation induced by grafted poly (ethylene oxide) layers: Theoretical prediction and experimental verification. *Proc. Natl. Acad. Sci. U. S. A.* 95:1032.

117. Rovira-Bru, M., D. H. Thompson, and I. Szleifer. 2002. Size and structure of spontaneously forming liposomes in lipid/PEG-lipid mixtures. *Biophys. J.* 83:2419-2439.

118. Tsukanova, V., and C. Salesse. 2003. High-Pressure Transition of a Poly(ethylene glycol)-Grafted Phospholipid Monolayer at the Air/Water Interface. *Macromolecules*. 36:7227-7235.

119. Purrucker, O. 2004. Establishment of a New Plasma Membrane Model with Well-Defined Polymer Spacers. Technische Universität München, Universitätsbibliothek.

120. Russell, S. W., J. Li, and J. W. Mayer. 1991. In situ observation of fractal growth during amorphous silicon crystallization in a copper silicide (Cu3Si) matrix. *J. Appl. Phys.* 70:5153-5155.

121. Meakin, P. 1983. Formation of fractal clusters and networks by irreversible diffusion-limited aggregation. *Phys. Rev. Lett.* 51:1119-1122.

122. Miller, A., W. Knoll, and H. Möhwald. 1986. Fractal growth of crystalline phospholipid domains in monomolecular layers. *Phys. Rev. Lett.* 56:2633-2636.

123. Cao, G., X. Chen, C. Li, A. Ji, and Z. Cao. 2008. Self-assembled triangular and labyrinth buckling patterns of thin films on spherical substrates. *Phys. Rev. Lett.* 100:36102.

124. Colin, J., C. Coupeau, J. Durinck, and J. Grilhé. 2009. Buckling patterns of gold thin films on silicon substrates: Formation of superimposed blisters. *EPL (Europhysics Letters)*. 86:54002.

125. Siegel, A., and C. Naumann. 2010. Polymer Stabilized Lipid Membranes: Langmuir Monolayers. In Polymer Membranes/Biomembranes. W. P. Meier, and W. Knoll, editors. Springer Berlin / Heidelberg. 113-165.

126. Verdoucq, L., A. Grondin, and C. Maurel. 2008. Structure-function analysis of plant aquaporin AtPIP2; 1 gating by divalent cations and protons. *Biochem. J.* 415:409-416.

127. Campbell, I., and M. Humphries. 2011. Integrin Structure, Activation, and Interactions. *Cold Spring Harbor Perspectives in Biology*. 3.

128. Deverall, M., S. Garg, K. Lüdtke, R. Jordan, J. Rühe, and C. Naumann. 2008. Transbilayer coupling of obstructed lipid diffusion in polymer-tethered phospholipid bilayers. *Soft Matter*. 4:1899-1908.

129. Erb, E. M., K. Tangemann, B. Bohrmann, B. Müller, and J. Engel. 1997. Integrin IIb 3 reconstituted into lipid bilayers is nonclustered in its activated state but clusters after fibrinogen binding. *Biochemistry*. 36:7395-7402.

130. Gönnenwein, S., M. Tanaka, B. Hu, L. Moroder, and E. Sackmann. 2003. Functional incorporation of integrins into solid supported membranes on ultrathin films of cellulose: impact on adhesion. *Biophys. J.* 85:646-655.

131. Seitz, P. C., M. D. Reif, O. V. Konovalov, R. Jordan, and M. Tanaka. 2009. Modulation of Substrate–Membrane Interactions by Linear Poly(2-methyl-2-oxazoline) Spacers Revealed by X-ray Reflectivity and Ellipsometry. *ChemPhysChem*. 10:2876-2883.

132. Baron, W., L. Decker, and H. Colognato. 2003. Regulation of integrin growth factor interactions in oligodendrocytes by lipid raft microdomains. *Curr. Biol.* 13:151-155.

133. Leitinger, B., and N. Hogg. 2002. The involvement of lipid rafts in the regulation of integrin function. *J. Cell Sci.* 115:963-972.

134. Hogg, N., M. Laschinger, K. Giles, and A. McDowall. 2003. T-cell integrins: more than just sticking points. *J. Cell Sci.* 116:4695.

135. Gopalakrishna, P., S. K. Chaubey, P. S. Manogaran, and G. Pande. 2000. Modulation of α5β1 integrin functions by the phospholipid and cholesterol contents of cell membranes. *J. Cell Biochem.* 77:517-528.

136. Ramprasad, O. G., G. Srinivas, K. S. Rao, P. Joshi, J. P. Thiery, S. Dufour, and G. Pande. 2007. Changes in cholesterol levels in the plasma membrane modulate cell signaling and regulate cell adhesion and migration on fibronectin. *Cell Motil. Cytoskeleton*. 64:199-216.

137. Blystone, S. D., I. L. Graham, F. P. Lindberg, and E. J. Brown. 1994. Integrin alpha v beta 3 differentially regulates adhesive and phagocytic functions of the fibronectin receptor alpha 5 beta 1. *J. Cell Biol.* 127:1129.

138. Cunningham, O., A. Andolfo, M. L. Santovito, L. Iuzzolino, F. Blasi, and N. Sidenius. 2003. Dimerization controls the lipid raft partitioning of uPAR/CD87 and regulates its biological functions. *EMBO J*. 22:5994-6003.

139. Wong, S. W., M. J. Kwon, A. M. K. Choi, H. P. Kim, K. Nakahira, and D. H. Hwang. 2009. Fatty acids modulate Toll-like receptor 4 activation through regulation of receptor dimerization and recruitment into lipid rafts in a reactive oxygen species-dependent manner. *J. Biol. Chem.* 284:27384.

140. Wiseman, P. W., C. M. Brown, D. J. Webb, B. Hebert, N. L. Johnson, J. A. Squier, M. H. Ellisman, and A. F. Horwitz. 2004. Spatial mapping of integrin interactions and dynamics during cell migration by Image Correlation Microscopy. *J. Cell Sci.* 117:5521-5534.

141. Hantgan, R. R., C. Paumi, M. Rocco, and J. W. Weisel. 1999. Effects of Ligand-Mimetic Peptides Arg-Gly-Asp-X (X = Phe, Trp, Ser) on αIIbβ3 Integrin Conformation and Oligomerization†. *Biochemistry*. 38:14461-14474.

142. Roca-Cusachs, P., N. C. Gauthier, A. Del Rio, and M. P. Sheetz. 2009. Clustering of 5 1 integrins determines adhesion strength whereas v 3 and talin enable mechanotransduction. *Proc. Natl. Acad. Sci. U. S. A.* 106:16245.

143. Takagi, J., B. M. Petre, T. Walz, and T. A. Springer. 2002. Global Conformational Rearrangements in Integrin Extracellular Domains in Outside-In and Inside-Out Signaling. *Cell*. 110:599-611.

144. Takagi, J., K. Strokovich, T. A. Springer, and T. Walz. 2003. Structure of integrin [alpha]5[beta]1 in complex with fibronectin. *EMBO J*. 22:4607-4615.

145. Kim, M., C. V. Carman, and T. A. Springer. 2003. Bidirectional transmembrane signaling by cytoplasmic domain separation in integrins. *Science*. 301:1720.

146. Wang, W., and B.-H. Luo. 2010. Structural basis of integrin transmembrane activation. *J. Cell. Biochem.* 109:447-452.

147. Lee, A. G. 2004. How lipids affect the activities of integral membrane proteins. *Biochimica et Biophysica Acta (BBA) - Biomembranes*. 1666:62-87.

148. Lee, C. S., S. H. Lee, S. S. Park, Y. K. Kim, and B. G. Kim. 2003. Protein patterning on silicon-based surface using background hydrophobic thin film. *Biosensors and Bioelectronics*. 18:437-444.

149. Zhu, J., B. Boylan, B.-H. Luo, P. J. Newman, and T. A. Springer. 2007. Tests of the Extension and Deadbolt Models of Integrin Activation. *J. Biol. Chem.* 282:11914-11920.

VITA

VITA

AMANDA P. SIEGEL

EDUCATION

Ph.D. in Chemistry	Purdue University Indianapolis, IN, 2011
J.D., ***with honors***	University of Chicago, Chicago, IL, 1991
B.S. in Physics, ***cum laude***	Yale University, New Haven, CT, 1986

RESEARCH EXPERIENCE

Graduate Student. Thesis advisor: Christoph A. Naumann. **2006-2011**
Area of Research: physical properties of model bilayers including membrane receptor-protein, membrane receptor-lipid, and lipopolymer-lipid interactions within model bilayers. Also investigated diffusion of receptor proteins on the plasma membrane.

HONORS AND AWARDS

Purdue Research Foundation (PRF) Research Grant, *awarded to top senior graduate student at the Indiana University-Purdue University at Indianapolis School of Science.* **2010-11**

ACS National Meeting Student Poster Award, Division of Colloids and Surface Chemistry **2009**

Travel Fellowship, IUPUI Graduate Student Office **2009**

Educational Enhancement Grant, IUPUI Graduate Student Office **2009**

PUBLICATIONS

Siegel, A. P., Murcia, M. J.; Johnson, M.; Reif, M.; Jordan, R., Ruehe, J., Naumann, C. A. (2010) Compartmentalizing a lipid bilayer by tuning lateral stress in a physisorbed polymer-tethered membrane. *Soft Matter* 6, 2723-2732.

Siegel, A. P., Naumann, C. A. (2010) Polymer stabilized lipid membranes: Langmuir monolayers. *Adv. Polymer Sci.* 224, 87-111.

Siegel, A.P., Kimble-Hill, A., Garg, S., Jordan, R., Naumann, C.A. (Submitted) Native ligands change integrin sequestering but not oligomerization in raft-mimicking lipid mixtures. *Submitted to Biophys. J.*

TEACHING/MENTORING

Course Instructor (Department of Chemistry and Chemical Biology, IUPUI)

Recitation Lecturer and Laboratory Instructor for "The Chemistry of Life" (CHEM 115) **2006- 2009**

Laboratory Instructor for "Experimental Chemistry II" (CHEM 126) **2006**

Guest lecturer (2-3 class meetings/term) for "Physical Chemistry of Molecules" (CHEM361) **2007-2011**

High School Student Mentorship

Guilherme Sprowl, subsequent 2010 Gates Millenium Scholar **2008-2009**

David O'Brien, subsequent 2010 Intel Science Talent Search Seminifinalist **2009-2010**

Kevin Song, subsequent 2010 Siemens Competition in Math : Science : Technology Semifinalist **2010 summer**

TECHNICAL EXPERTISE

Techniques utilized extensively include reconstitution of membrane proteins into lipid bilayers, wide field single molecule fluorescence microscopy, confocal fluorescence microscopy, fluorescence correlation spectroscopy, quantitative epifluorescence microscopy, sonochemical fluorescent nanoparticle (quantum dot) synthesis, Langmuir Blodgett film deposition. Responsible for routine maintenance and training. Also familiar with atomic force microscopy.

CONTRIBUTED RESEARCH PRESENTATIONS

(* indicates presenting author)

Oral

Siegel, A.P. ***,** Kimble-Hill, A., Jordan, R., Naumann, C.A. (2011). Effect of native ligands on integrin oligomerization and raft recruitment processes studied in cholesterol containing polymer-tethered lipid bilayer systems. Presented at the 42nd Meeting of the ACS Central Region.

Siegel, A.P., Feuza, N., Jordan, R., Juergen, R., Naumann, C.A.* (2011). Membrane organization and dynamics in physisorbed polymer-tethered phospholipid bilayers. Presented at the 241st ACS National Meeting, Anaheim, CA.

Siegel, A.P.*, Minner, D.E., Murcia, M. Tackett, L., Elmendorf, J. S., Ritchie, K., Naumann, C.A. (2010). Monitoring compartmentalization of the plasma membrane and model membranes using quantum dots monovalently conjugated to tracer molecules. Presented at the 239th ACS National Meeting, San Francisco, CA.

Naumann, C.A.*, **Siegel, A.P.,** Kimble-Hill, A.C. (2010). Raft recruitment processes of membrane proteins studied in planar model membranes. Presented at the 239th ACS National Meeting, San Francisco, CA.

Naumann, C.A.*, Kimble-Hill, A.C., Garg, S., **Siegel, A.P.,** Luedtke, K., Jordan, R. (2009). Protein recruitment to and from raft-mimicking domains studied using polymer-tethered membranes. Presented at the 237th ACS National Meeting, Salt Lake City, UT.

Siegel, A.P.*, Garg, S., Kimble-Hill, A.C., Murcia, M.J., Luedtke, K., Jordan, R., Ruehe, J., Naumann, C.A. (2008). Studying complex processes of membrane dynamics and organization using physisorbed polymer-tethered membranes. Presented at the 236th ACS National Meeting, Philadelphia, PA.

Siegel, A.P.*, Murcia, M.J., Ruehe, J., Naumann, C.A. (2007). Formation of polymeric fences in planar model membranes: An experimental platform for the study of hop diffusion . Presented at the 233rd ACS National Meeting, Chicago, IL.

Poster

Siegel, A.P.*, Kimble-Hill, A., Jordan, R., Naumann, C.A. (2011). Raft Recruitment Processes and Oligomerization State of Integrins Studied in Polymer-Tethered Single and Double Bilayer Systems. Presented at the 56th Annual Meeting of the Biophysical Society. Baltimore, MD.

Minner, D.E., **Siegel, A.P.,** Rauch, P Käs, J., Naumann, C.A.* (2010) Tuning Cellular Mechano-Response Using Biomembrane-Mimicking Substrates of Adjustable Fluidity. Presented at the 4th Mechanobiology Workshop and Biophysical Joint Meeting. Singapore.

Siegel, A.P., Minner, D.E., Murcia, M.J., Elmendorf, J.S., Ritchie, K., Naumann, C.A.* (2010). Monitoring Submicron and Micron-Size Membrane Compartments using Quantum Dots Monovalently Conjugated to Tracer Molecules. Presented at the 55th Annual Meeting of the Biophysical Society. San Francisco, CA.

Siegel, A.P.*, Murcia, M., Minner, D., Elmendorf, J.S., Tackett, L., and Naumann, C.A. Monitoring Membrane Compartmentalization in Adipocytes. Collaborative Research from the Center for Membrane BioSciences (2010). Presented at the 2nd Annual IUPUI Research Day.

Siegel, A.P.*, Murcia, M.J., Ruehe, J., Jordan, R., Naumann, C.A. (2009). Tuneable buckling in polymer-tethered lipid bilayers creates diffusion barriers and a platform for studying hop diffusion. Presented at the 237th ACS National Meeting, Salt Lake City, UT. *Received ACS National Meeting Poster Award from the division of Colloids and Surface Chemistry.*

Minner, D.E.*, Rauch, P., **Siegel, A.P.,** Stelzer, J., Käs, J., Sprowl, G., Harvey, K., Siddiqi, R., Atkinson, S., Naumann, C.A. (2009). Tuning Cellular Mechano-Response Using Biomembrane-Mimicking Substrates of Adjustable Fluidity. Presented at the 54th Annual Meeting of the Biophysical Society, Boston, MA.

Siegel, A.P.*, Murcia, M.J., Ruehe, J., Jordan, R., Naumann, C.A. (2008). Membrane Compartmentalization Through Bilayer Buckling in Polymer-Tethered Phospholipid Bilayers. Presented at the 1st Purdue University Biology and Applications of Membrane Science Symposium.